

ANL-7845

RETURN TO ANL (IDAF-C) LIBRARY.

7845

ANL-7845

Argonne National Laboratory

REACTOR DEVELOPMENT PROGRAM PROGRESS REPORT

July 1971

The facilities of Argonne National Laboratory are owned by the United States Government. Under the terms of a contract (W-31-109-Eng-38) between the U. S. Atomic Energy Commission, Argonne Universities Association and The University of Chicago, the University employs the staff and operates the Laboratory in accordance with policies and programs formulated, approved and reviewed by the Association.

MEMBERS OF ARGONNE UNIVERSITIES ASSOCIATION

The University of Arizona	Kansas State University	The Ohio State University
Carnegie-Mellon University	The University of Kansas	Ohio University
Case Western Reserve University	Loyola University	The Pennsylvania State University
The University of Chicago	Marquette University	Purdue University
University of Cincinnati	Michigan State University	Saint Louis University
Illinois Institute of Technology	The University of Michigan	Southern Illinois University
University of Illinois	University of Minnesota	The University of Texas at Austin
Indiana University	University of Missouri	Washington University
Iowa State University	Northwestern University	Wayne State University
The University of Iowa	University of Notre Dame	The University of Wisconsin

NOTICE

This report was prepared as an account of work sponsored by the United States Government. Neither the United States nor the United States Atomic Energy Commission, nor any of their employees, nor any of their contractors, subcontractors, or their employees, makes any warranty, express or implied, or assumes any legal liability or responsibility for the accuracy, completeness or usefulness of any information, apparatus, product or process disclosed, or represents that its use would not infringe privately-owned rights.

Printed in the United States of America
Available from
National Technical Information Service
U.S. Department of Commerce
5285 Port Royal Road
Springfield, Virginia 22151
Price: Printed Copy \$3.00; Microfiche \$0.95

ARGONNE NATIONAL LABORATORY
9700 South Cass Avenue
Argonne, Illinois 60439

REACTOR DEVELOPMENT PROGRAM
PROGRESS REPORT

July 1971

Robert B. Duffield, Laboratory Director
Robert V. Laney, Associate Laboratory Director

	<u>Program Area</u>	<u>Lead Division</u>	<u>Division Director/ Program Manager</u>
I	EBR-II	EBR-II	M. Levenson
II	LMFBR Design Support	ETD	S. A. Davis
III	Instrumentation and Control	ETD	S. A. Davis
IV	Sodium Technology	CEN	R. C. Vogel/L. Burris
V	Fuels and Materials Development	MSD	P. G. Shewmon
VI	Fuel Cycle	CEN	R. C. Vogel/D. S. Webster
VII	Reactor Physics	AP	R. Avery
VIII	Reactor Safety	RAS	W. R. Simmons
IX	Environmental Studies	CES	E. J. Croke

Report Coordinator: M. Weber

Issued: August 20, 1971

FOREWORD

The Reactor Development Program Progress Report describes current activities, technical progress, and technical problems in the program at Argonne National Laboratory sponsored by the USAEC Division of Reactor Development and Technology. Not all projects are reported every month, but a running account of each project is maintained in the series of reports.

The last six reports
in this series are:

December 1970	ANL-7765
January 1971	ANL-7776
February 1971	ANL-7783
March 1971	ANL-7798
April-May 1971	ANL-7825
June 1971	ANL-7833

REACTOR DEVELOPMENT PROGRAM

Highlights of Project Activities for July 1971

EBR-II

The reactor operated for 1752 MWd in the two-month period ending July 15; the accumulated operational total is now 45,540 MWd. Continued searching for the sources of the recent increases in cover-gas activity identified two experimental-irradiation subassemblies (X073 and X085) as definite sources; these were removed from the reactor (see report for last month). A third experimental-irradiation subassembly, X082A, was identified as a probable source; this subassembly was moved to the storage basket July 15. It is a Mark-E61 type and contains Mark-IA driver-fuel elements that had been irradiated previously to a peak burnup of ~2.8 at. % in controlled-flow subassemblies.

The first Mark-K1 subassembly, which is designed for irradiation of materials specimens at high temperature, has been fabricated and loaded with specimens of Types 304, 304L, 316, and 316L stainless steel. The specimens will be exposed to flowing primary sodium whose temperature has been raised to 1250°F through gamma heating of susceptors. Four types of temperature monitors will be incorporated immediately adjacent to the specimens.

FUELS AND MATERIALS DEVELOPMENT

Low-cycle creep-fatigue tests of Type 304 stainless steel with varying hold times have shown that a thermodynamically unstable microstructure, which changes during the test, has a significant effect on fatigue life. A linear relationship between time to failure and hold time, first suggested by Conway at General Electric, has been confirmed. A good correlation is obtained between uniaxial and biaxial stress-rupture data for 20% cold-worked Type 316 stainless steel, except in the lowest stress range at the highest temperature (1400°F).

Both fast- and thermal-neutron radiography with a ^{252}Cf source have been assessed. The former has only limited potential, but the thermal-neutron results are equal in quality to those obtained with a reactor.

The effective use of the magnetic method of determining the degree of cold work in stainless steel tubes requires that martensite be absent from the tubes before the final drawing operations. This can be ensured by annealing at 1850-1900°F, followed by quenching.

Thermodynamic data have been developed to determine the conditions for control of stoichiometry during creep testing of mixed-oxide fuel. The results were applied to the adjustment of the oxygen-to-metal ratio (O/M)

of a batch of fuel for the ANL Groups O-4 and O-5 experimental fuel pins for irradiation in EBR-II. The O/M value was lowered from 1.98 to 1.938 ± 0.005 . Twenty-five elements in the Groups O-4 and O-5 series have been fabricated to date.

An improved method of computing the temperature distribution across a fuel pin has been developed that accounts for temperature variations of thermal conductivity and for porosity variations. This method has been incorporated into codes.

Thermodynamic experiments suggest that cesium forms cesium uranate rather than cesium oxide in the cooler regions of a fuel pellet, giving a low partial pressure of cesium. Moreover, molybdenum has a significant effect on the oxygen potential of urania and may affect its reaction with cesium.

FUEL CYCLE

At the request of the AEC, a reference conceptual design for melt decladding of fuel subassemblies has been developed, based on experimental investigations of several alternatives. In this concept, two vertically suspended LMFBR subassemblies are melted by being lowered gradually into a crucible which is heated to a temperature between 1550 and 1600°C . After the fuel cladding and structural members have been melted, most of the molten steel is poured into a mold at one side of the crucible by tilting the crucible 10° below horizontal. The oxide fuel pellets are then poured into a receiver at the other side of the crucible by tilting the crucible 45° below horizontal.

REACTOR PHYSICS

The Beginning-of-Life (BOL) Configuration of the FTR

Upon completing the series of control rod and test region worths in subcritical configurations of the FTR Engineering Mockup Critical on ZPR-9, the reactor was reconstituted to simulate the critical FTR system at the time of its initial operation (BOL). For this purpose all fuel depletion was removed, test regions and loops were inserted and the reactor oscillator was removed; the worths of various bankings of the control and safety rods were then studied in a sequence of five modifications of the BOL assembly.

A measurement of isothermal temperature coefficient in the region of 25 to 30°C for the beginning-of-life core shows it to be $-3.3 \pm 0.3 \text{ Ih}/^{\circ}\text{C}$; earlier measurements have evaluated the equivalent end-of-cycle temperature coefficient as $-4.1 \pm 0.4 \text{ Ih}/^{\circ}\text{C}$.

Changes in Central Reactivity Effects in a Sodium-voided Core

The central zone of Assembly 7 in ZPR-6, now fueled with plutonium containing 27 wt % ^{240}Pu , was voided of sodium to appraise the consequent safety-related reactivity effects. With the exception of stainless steel and sodium, all measured reactor fissile, fertile and control materials showed decreased reactivity worths.

Further emphasizing the importance of the study of the interaction of sodium-voiding and reactivity effects in an LMFBR core, the worth of the ^{238}U Doppler effect in the ZPR-6 voided central zone was found to be 40% less than that measured in the unvoided zone.

REACTOR SAFETY

Coolant Dynamics

In analysis of sodium voiding resulting from a loss-of-flow accident, the behavior of the liquid film left behind on the fuel pins is of considerable importance, as the dryout of this film is likely to lead to immediate cladding failure. Available voiding models usually are based on voiding by one or several large bubbles, so the time for film dryout is calculated to depend simply on the rate of radial liquid transport as a result of vaporization from the liquid film, which is assumed to be stationary. For typical LMFBR conditions and an initial liquid fraction of 0.15, dryout has been calculated to occur 200-300 msec after local voiding. However, a study that examined the effect of axial liquid transport (resulting from vapor drag inducing film motion) has shown that axial mass transport can proceed at least an order of magnitude faster than that calculated above. Thus, local dryout spots might occur as early as 20-30 msec after local voiding. Therefore, current voiding models should be extended to include two-phase annular flow between the liquid slugs.

Fuel Dynamics Studies in TREAT

Data and analyses from Tests E1, E2, H2, E3, and E4 have been evaluated to provide preliminary modeling information on internal and external fuel motion arising from severe transient-overpower conditions. Together, these tests provide the first picture of LMFBR oxide-fuel behavior under transient overpower in a flow-channel environment provided by TREAT loops. Even for FTR reactivity-input calculations exceeding \$5/sec, maximum accident cladding temperatures occur at the top of the fuel because of the axial heat transport by flowing coolant. These tests simulate that feature. The results support use of SAS calculations of cladding strain up to the onset of melting. The data also support calculations predicting cladding failure at the top of the fuel, the hottest region of the cladding. The posttest fragments of once-molten fuel are small. From

the appearance of the fines (which were not rounded "shot-like" shapes) from Test E2, it is apparent the original sizes of this material were larger and that an unknown amount of fragmentation occurred before the final distributions. The extensive dispersal throughout the E2 loop indicates that these fines can be carried out of the core. Test E3 indicates that fission-gas-driven oxide mixing with the coolant promotes a more energetic fuel-coolant interaction, but not one approaching overall thermodynamic limits. Conversion of energy to work on the coolant was low in all tests. Failure of preirradiated pins having high internal pressure due to fission-product gases produces an energy-conversion efficiency greater than that resulting from failure of fresh pins.

Progress continues in the use of the hodoscope for observing fuel dynamics during TREAT-loop tests. For example, interesting and strong evidence from the hodoscope shows surprisingly early major fuel-pin distortion in the first test (L1) in the loss-of-coolant series. The distortion, without rupture of cladding, started at 6.5 ± 0.5 sec, consistent with capsule flowmeter indications showing loss of flow beginning at 6 sec, at which time TREAT integrated power (energy input) had reached only 20 ± 5 MW-sec. To expose the small pin distortions (with a resolution of 10 mils or less) required additional extensions in hodoscope data-analysis techniques.

TABLE OF CONTENTS

<u>189a No.</u>		<u>Page</u>
	I. EXPERIMENTAL BREEDER REACTOR NO.II	1.1
	A. Operations	1.1
02-075	1. Reactor Operations	1.1
	a. Operations	1.1
02-076	2. Fuels and Examination Facility Operations	1.3
	a. Fuel Assembly	1.3
	b. Reactor Support	1.4
02-073	3. Fuel and Hardware Procurement	1.4
	a. Reclamation of Vendor Fuel	1.4
02-204	4. Reactor Plant Services for Experimenters	1.4
02-206	5. Operations in Support of Experimental Irradiations	1.8
	a. Operational In-cell Handling and Examination Equipment	1.8
	b. Experimental Support	1.9
	B. Fuels and Materials Studies	1.9
02-609	1. Coolant Chemistry	1.9
	a. Monitoring of Sodium-coolant Quality	1.9
	b. Radioactivity of EBR-II Primary-system Components	1.15
02-610	2. Materials-Coolant Compatibility	1.16
	a. Evaluation and Surveillance of EBR-II Materials	1.16
	b. Surveillance of Materials for High-temperature Experiments	1.19
	c. Assistance to Sodium Technology: CCTL Evaluation	1.20
02-145	3. Metal Driver Fuel Development and Application	1.21
	a. Mark-IA Fuel	1.21
	b. Advanced Fuel (Mark II)	1.25
	c. Surveillance Support	1.26
	C. Engineering	1.27
02-068	1. Systems Engineering	1.27
	a. Surveillance, Evaluation, and Studies of Systems	1.27
02-046	2. New Subassemblies and Experimental Support	1.27
	a. Experimental-irradiation Subassemblies	1.27
	PUBLICATIONS	1.33

TABLE OF CONTENTS

<u>189a No.</u>		<u>Page</u>
	II. LMFBR DESIGN SUPPORT	2.1
02-097	A. Heat Transfer and Fluid Flow	2.1
	1. LMFBR Flow Stability Studies	2.1
	a. Preparation of Apparatus	2.1
	2. Nonboiling Transient Heat Transfer	2.1
	a. Analysis of Heat-flux Transients	2.1
	3. Liquid-metal Heat Transfer in Pin Bundles	2.2
	a. Analytical Investigations	2.2
	4. Electron Bombardment Heater (EBH) Development	2.2
	a. MHD Characteristics of EB-versus- Resistance-type Heaters	2.2
	5. Heat Transfer in Liquid-metal-heated Steam Generators	2.2
02-099	B. Engineering Mechanics	2.3
	1. Structure-fluid Dynamics	2.3
	a. Parallel Flow-induced Vibration	2.3
	b. Crossflow-induced Vibrations of Cylinders	2.5
	III. INSTRUMENTATION AND CONTROL	3.1
02-024	A. Instrumentation Development for Instrumented Subassembly	3.1
	1. Instrumented Subassembly (ISA) Flowmeters	3.1
	2. Fuel-pin and Coolant Thermocouples	3.1
02-025	B. FFTF Instrumentation Development	3.2
	1. Magnetometer Probe-type Flowsensors	3.2
02-138	C. Neutron-detector Channel Development	3.3
	1. Intermediate- and Wide-range Systems	3.3
	2. High-temperature Neutron-detector Technology	3.4
	3. High-temperature Neutron-detector Cable Technology	3.4
	4. NITF Test Program	3.5

TABLE OF CONTENTS

<u>189a No.</u>		<u>Page</u>
02-096	D. Advanced Technology Instrument Development	3.5
	1. Acoustic Surveillance	3.5
	a. Development of High-temperature Detector	3.5
	b. Development of Acoustic Waveguides	3.6
	2. Vibration Sensor	3.7
	a. Out-of-pile Tests of Sodium-immersible Commercial Transducers	3.7
02-528	E. Plant Dynamics and Control Analysis	3.8
	1. Analysis of Overall Control-system Performance during Mild Transients to Identify and Resolve Control Problems	3.8
	PUBLICATION	3.8
	IV. SODIUM TECHNOLOGY	4.1
02-593	A. Sodium Impurity Analysis and Control	4.1
	1. Studies of the Sodium-Oxygen-Hydrogen System	4.1
	2. Vacuum Distillation as an Analytical Method for Impurities in Sodium	4.2
02-137	B. Nonmetallic Impurity Interactions in Sodium-Metal Systems	4.3
	1. Development of Equilibration Methods for Determining the Activity of Nonmetallic Impurities in Sodium	4.3
	a. Development of the Vanadium-wire Equilibration Method for Determining Oxygen Activity in Sodium	4.3
	b. Application of the Equilibration Method to the Measurement of Carbon Activity in Sodium	4.5
02-213	C. Sodium Effects on Mechanical Behavior of Stainless Steel	4.6
	1. Studies of Carbon Transport in Sodium-Steel Systems	4.6
	a. Distribution of Carbon between Iron-base Alloys and Liquid Sodium	4.6

TABLE OF CONTENTS

<u>189a No.</u>		<u>Page</u>
	b. Measurements of Carbon Activities in Fe-Ni and Fe-Cr-Ni Alloys	4.8
	PUBLICATION	4.9
	V. FUELS AND MATERIALS DEVELOPMENT	5.1
	A. LMFBR Cladding and Structural Materials	5.1
02-605	1. Swelling and Mechanical Behavior of Cladding Alloys	5.1
	a. Swelling of Type 304 Stainless Steel	5.1
02-091	2. Creep, Fracture, and Fatigue Studies on Stainless Steel	5.2
	a. Low-cycle Fatigue	5.2
	b. Stress Rupture of 20% Cold-worked AISI Type 316 Stainless Steel at Elevated Temperatures	5.6
02-092	3. Nondestructive Testing Research and Development	5.9
	a. Fast-neutron Radiography with ^{252}Cf	5.9
	b. Thermal-neutron Radiography	5.12
	c. Development of Pulsed Eddy-current Equipment for Testing Fuel-element Jackets in FEF	5.12
02-133	4. NDT Characterization of Cladding Alloys	5.13
	a. NDT Measurement of Effective Cold Work in Cladding Tubes	5.13
	B. Fuel Properties	5.13
02-094	1. High-temperature Properties of Ceramic Fuels	5.13
	a. Plastic Yielding and Fracture of Mixed Oxides	5.13
	b. Thermodynamic Behavior of Mixed-oxide Fuels	5.16
	c. Compressive Creep of Mixed-oxide Fuels	5.18
	d. Irradiation Effects in Creep of Oxide Fuels	5.20
02-162	2. Thermochemical Properties of Reactor Fuels	5.20
	a. Fission-product Oxide Distribution and Cladding Interaction	5.20
	b. U-Pu-O Fuel-Fission-product Interactions	5.22

TABLE OF CONTENTS

<u>189a No.</u>		<u>Page</u>
	C. Fuel Elements	5.23
02-086	1. Behavior of Reactor Materials	5.23
	a. Migration of Major Fuel Constituents	5.23
02-005	2. Oxide Fuel Studies	5.26
	a. Fuel-swelling Studies	5.26
	b. Fuel-element Performance	5.27
	PUBLICATIONS	5.29
	VI. FUEL CYCLE	6.1
02-173	A. Molten-metal Decladding of LMFBR Fuels	6.1
	1. Engineering Concepts, Analysis, and Evaluation	6.1
	2. Engineering Development	6.2
	a. Melt Decladding	6.2
	b. Vacuum Evaporation of Zinc	6.4
	3. Process Demonstration Experiments	6.4
	a. Irradiated-fuel Experiments	6.4
02-157	B. LMFBR Fuel Materials Preparation--U/Pu Nitrates to Oxides	6.5
	1. Pilot-plant Program	6.5
02-158	C. LMFBR Fuel Fabrication--Analyses and Continuous Processing	6.6
	1. Plutonium/Uranium Ratio in Fuel	6.7
	a. Analysis of ThO ₂ -UO ₂ Pellets	6.8
	b. Analysis of ThO ₂ -UO ₂ Mixed Powder	6.9
	c. Conclusions	6.10
	2. Oxygen Content of Fuel	6.10
	VII. REACTOR PHYSICS	7.1
	A. ZPR Fast Critical Experiments	7.1
02-179	1. Fast Critical Facilities; Experiments and Evaluation--Illinois	7.1
	a. Clean Critical Experiments	7.1
	b. Mockup Critical Experiments	7.4
02-181	2. Fast Critical Facilities; Experiments and Evaluation--Idaho	7.9
	a. Clean Critical Experiments	7.9
	b. Doppler Experiments	7.10

TABLE OF CONTENTS

<u>189a No.</u>		<u>Page</u>
	B. Support of ZPR Fast Critical Experiments	7.10
02-134	1. Fast Critical Experiments; Theoretical Support--Illinois	7.10
	a. ZPR Heterogeneity Method Development	7.10
02-013	2. Fast Critical Experiments; Experimental Support--Illinois	7.13
	a. Maintenance of Support Techniques and Facilities	7.13
	C. Fast Reactor Analysis and Computational Methods	7.14
02-081	1. Reactor Physics--Applied Computational Methods	7.14
	a. Cross-section Data Evaluation	7.14
	b. Reactor Computations and Code Development	7.15
02-085	2. Reactor Code Center	7.21
	D. Acquisition of Nuclear Data	7.22
02-083	1. Burnup Analysis and Fission Yields for Fast Reactors	7.22
	a. Development of Analytical Procedures for Fission-product-burnup Monitors	7.22
	PUBLICATIONS	7.24
	VIII. REACTOR SAFETY	8.1
02-112	A. Accident Analysis and Safety Evaluation	8.1
	1. Analysis of Fuel Behavior	8.1
	a. Analysis of Fuel Behavior up to Gross Cladding Failure	8.1
	b. Analysis of Fuel Motion after Loss of Integrity of Pins ("Slumping")	8.2
02-114 & 02-614	B. Coolant Dynamics	8.3
	1. Liquid-Vapor Dynamics	8.3
	a. Liquid-film Thickness Criteria	8.3
	2. Mathematical Models of Voiding and Reentry	8.4
	a. Models of Expulsion and Reentry	8.4

TABLE OF CONTENTS

<u>189a No.</u>		<u>Page</u>
02-117	C. Fuel Dynamics Studies in TREAT	8.5
	1. Transient In-pile Tests of Ceramic Fuel	8.5
	a. Effects of Release of Small Amount of Molten Fuel from Seven-pin Cluster of Fresh Fuel with Local Melting (Test D1)	8.5
	2. Experiment Support	8.6
	a. Procurement of Mark-IIA Loops for In-pile Tests	8.6
	b. Procurement of Stretched Mark-IIC Loops for In-pile Tests	8.6
	3. Analytical Support	8.7
	a. Modeling of Multiple-pin Behavior	8.9
	b. TREAT Test Analyses	8.10
	c. Hodoscope Development	8.15
02-164	D. Fuel-Coolant Interactions	8.21
	1. In-pile Simulation Tests: Expulsion and Reentry	8.21
	a. Detailed Design of the R-series Test Vehicle	8.21
02-122	E. TREAT Operations	8.22
	1. Operations	8.22
	a. Neutron Radiographs of Capsules for TREAT and EBR-II Experiments	8.22
	PUBLICATION	8.22
	IX. ENVIRONMENTAL STUDIES	9.1
02-166	A. Thermal-plume Dispersion Studies	9.1
	1. Sinking-plume Experiment	9.1

Listing of Reportable
ANL Reactor Development Program Projects
in 189a Order

189a No.	Reported This Month in Section	189a Title	RDT Branch
02-005	V	Oxide Fuel Studies	RT-FM
02-010		Fast Critical Experiments; Theoretical Support--Idaho	RT-PH
02-011		Fast Critical Experiments; Experimental Support--Idaho	RT-PH
02-012		Fast Critical Experiments--Industrial Appointments	RT-PH
02-013	VII	Fast Critical Experiments; Experimental Support--Illinois	RT-PH
02-015		Planning and Evaluation of Critical Assembly Experiments	RT-PH
02-019		Production of Materials for ZPR Experiments	RE-FE
02-020		ZPR Materials Procurement	RE-FE
02-024	III	Instrumentation Development for Instrumented Subassembly	PE-IC
02-025	III	FFTF Instrumentation Development	PE-IC
02-026		Core Component Test Loop (CCTL)	RE-CD
02-045		Equipment--Fuel Related	RE-FH
02-046	I	New Subassemblies and Experimental Support	RE-CD
02-048		Instrumented Subassemblies	RE-CD
02-061		Nuclear Instrument Test Facility	PE-IC
02-068	I	Systems Engineering	PE-LS
02-073	I	Fuel and Hardware Procurement	RE-FE
02-075	I	Reactor Operations	PE-LS
02-076	I	Fuels and Examination Facility Operations	RE-FE
02-081	VII	Reactor Physics--Applied Computational Methods	RT-PH
02-082		Cross-section Measurements	RT-PH
02-083	VII	Burnup Analysis and Fission Yields for Fast Reactors	RT-PH
02-084		Determination of Nuclear Constants	RT-PH
02-085	VII	Reactor Code Center	RT-PH
02-086	V	Behavior of Reactor Materials	RT-FM
02-087		Chemistry of Irradiated Fuel Materials	RT-FM
02-091	V	Creep, Fracture, and Fatigue Studies on Stainless Steel	RT-FM
02-092	V	Nondestructive Testing Research and Development	RT-FM
02-094	V	High-temperature Properties of Ceramic Fuels	RT-FM
02-096	III	Advanced Technology Instrument Development	RT-ST
02-097	II	Heat Transfer and Fluid Flow	RT-ST

189a No.	Reported This Month in Section	189a Title	RDT Branch
02-099	II	Engineering Mechanics	RT-ST
02-112	VIII	Accident Analysis and Safety Evaluation	NS-FS
02-114	VIII	Coolant Dynamics	NS-FS
02-116		Fuel-element Failure Propagation	NS-FS
02-117	VIII	Fuel Dynamics Studies in TREAT	NS-FS
02-119		High-temperature Physical Properties and Equation-of-state of Reactor Materials	NS-FS
02-122	VIII	TREAT Operations	NS-FS
02-126		Structural Dynamics and Containment	NS-FS
02-131		EBR-II In-core Instrument Test Facility (INCOT)	PE-IC
02-133	V	NDT Characterization of Cladding Alloys	RT-FM
02-134	VII	Fast Critical Experiments; Theoretical Support--Illinois	RT-PH
02-137	IV	Nonmetallic Impurity Interactions in Sodium-Metal Systems	RT-CC
02-138	III	Neutron-detector Channel Development	PE-IC
02-144		Reactor Analysis, Testing, and Methods Development	RE-CD
02-145	I	Metal Driver Fuel Development and Application	RE-FE
02-148		Operation with Failed Fuel	RE-CD
02-150		Hot Fuel Examination Facilities	PE-FH
02-151		Characterization of Irradiation Environment	RE-CD
02-157	VI	LMFBR Fuel Materials Preparation--U/Pu Nitrates to Oxides	RT-FR
02-158	VI	LMFBR Fuel Refabrication--Analyses and Continuous Processing	RT-FR
02-159		LMFBR Reprocessing--Plutonium Isolation	RT-FR
02-162	V	Thermochemical Properties of Reactor Fuels	RT-FR
02-164	VIII	Fuel-Coolant Interactions	NS-FS
02-165		Postaccident Heat Removal	NS-FS
02-166	IX	Thermal-plume Dispersion Studies	PA
02-173	VI	Molten-metal Decladding of LMFBR Fuels	RT-FR
02-175		Physical and Chemical Studies--Molten Fuel, Cladding, and Coolant	RT-FR
02-177		Activation Studies of Fast-neutron Spectra	RT-FM
02-178		ZPR-6 and -9 Operations and Maintenance	RT-PH
02-179	VII	Fast Critical Facilities; Experiments and Evaluation--Illinois	RT-PH
02-180		ZPPR Operations and Maintenance	RT-PH
02-181	VII	Fast Critical Facilities; Experiments and Evaluation--Idaho	RT-PH
02-185		Lake Circulation Model Development	PA

189a No.	Reported This Month in Section	189a Title	RDT Branch
02-194		Surveillance and Failure Evaluation of Experimental Fuel Irradiations	RT-FM
02-195		Instrumentation System Engineering	PE-IC
02-197		TREAT Improvements	PM-EB
02-204	I	Reactor Plant Services for Experimenters	RT-FM
02-205		Nondestructive Testing and Services to Experimenters	RT-FM
02-206	I	Operations in Support of Experimental Irradiations	RT-FM
02-210		Great Lakes Power Plant Siting Study	PA
02-213	IV	Sodium Effects on Mechanical Behavior of Stainless Steel	RT-CC
02-528	III	Plant Dynamics and Control Analysis	PE-IC
02-530		Operation of Digital Data Acquisition System (DAS)	PE-IC
02-593	IV	Sodium Impurity Analysis and Control	RT-CC
02-595		Radioactivity Monitoring in LMFBR Systems	RT-CC
02-605	V	Swelling and Mechanical Behavior of Cladding Alloys	RT-FM
02-606		Theoretical Fast-reactor Physics	RT-PH
02-607		On-line Monitoring and Sampling for Sodium Systems	RT-CC
02-609	I	Coolant Chemistry	RT-CC
02-610	I	Materials-Coolant Compatibility	RT-CC
02-611		GCFR Fuel-element Development	RT-FM
02-613		GCFR Safety-related Performance Aspects of Fuel and the Core	NS-AE
02-614	VIII	Coolant Dynamics	NS-FS

I. EXPERIMENTAL BREEDER REACTOR NO. II

A. Operations

1. Reactor Operations. G. E. Deegan (02-075)

a. Operations (Last reported: ANL-7825, p. 1.1)

The reactor operated for 1752 MWd in the two-month period ending July 15. The accumulated operational total is now 45,540 MWd.

While the primary tank was cooled to 580°F for installation of instrumented subassembly XX03, a new motor-generator set was installed in the power supply for the secondary pump. Testing of the pump under isothermal conditions included running it for 24 hr at the flow rate used for 62.5-MWt reactor operation. The primary tank was then heated to 700°F, and fuel handling for Run 49A was completed. After checking of the instrumentation for Subassembly XX03 and of reactor interlocks, the reactor was started up and brought to full power for Run 49A on May 18. On the following day, the reactor was shut down to make adjustments to move the nuclear center of the core closer to the geometric center. When fuel handling was completed, power was returned to 62.5 MWt for Run 49B. The run was terminated prematurely on May 31 when a large increase in cover-gas activity necessitated shutdown of the reactor. Experimental-irradiation subassembly X085, which contained an oxide-fuel element with a deliberately made cladding defect, was identified by a xenon-tag sample as the source of the leak. This subassembly had been originally loaded into the reactor in late October 1970 for Run 47A. It was moved to the storage basket during the fuel handling for Run 49C.

The reactor was started up for Run 49C on June 3, and operation continued at 62.5 MWt until June 7, when power was reduced to 58 MWt for oscillator experiments. During the experiments, an increase in cover-gas activity was observed. The experiments were stopped, and power was returned to 62.5 MWt. When the cover-gas activity approached five times the normal background, power was reduced to 30 MWt. At this power level, the leak apparently stopped. RDT concurrence was then received to operate at cover-gas activities up to 250 times normal background, and reactor power was returned to 62.5 MWt. Several further increases in activity occurred during the next day, and on June 8, Run 49C was terminated when the activity exceeded the new limit. A xenon-tag sample was negative. Six experimental-irradiation subassemblies were removed from the core as leak suspects. During the startup for Run 49D, it was confirmed that the fission-product source was still in the core, so the reactor was shut down from 40 MWt. Seven additional leak suspects were removed for Run 49E, and other possible suspects were lifted from the core. After each lift, the cover gas was checked for increased activity, but all checks

were negative. During the lifts, one experimental-irradiation subassembly, X119, could not be removed from the core. A scalloped dummy subassembly was installed adjacent to it to provide additional clearance, and the subassembly then was removed.

High cover-gas activity was again observed during the power increase for Run 49E, so the reactor was shut down from 40 MWt. Eight additional experiments and three Mark-II subassemblies were removed as leak suspects for Run 49F. The No. 4 control-rod thimble was replaced after an unsuccessful attempt to insert a subassembly in the position between the No. 4 and 5 control-rod thimbles (see Sect. I.C.1.a). After the replacement, loading continued without difficulty. Run 49F, which began on June 20, continued until June 30 with no abnormal cover-gas activity. A complete set of oscillator and rod-drop data was taken during the run.

Fuel handling for Run 50A included installation of three of the 11 subassemblies previously removed as leak suspects. The entire Run 50 was planned for the sole purpose of locating the subassembly with the cladding penetration; Run 50A was scheduled for 24 hr at 62.5 MWt. No abnormal cover-gas activity was seen. During fuel handling for Run 50B, the three suspects installed for Run 50A were removed and four other experimental-irradiation subassemblies that were leak suspects were installed. Cover-gas activity increased during startup, so the reactor was shut down from 30 MWt. Two of the four suspects, X058 and X082A, were removed, and the other two, X094 and X081, were left in the core. Run 50C, another 24-hr run at 62.5 MWt, was completed without evidence of a fission-product source in the reactor. Subassembly X058 was then inserted into the core, and X094 and X081 were removed. Operation with this loading produced no unusual cover-gas activity, so X058 was removed from the core. Subassembly X082A, the last of the four suspects that had been in the reactor during Run 50B, was then loaded into the reactor. Power was increased to 62.5 MWt, and after a short period of operation at that level, cover-gas activity began to rise. Run 50E was terminated, X082A was transferred to the storage basket, and the reactor was loaded for Run 50F, a scheduled 777-MWd run. Five experimental-irradiation and three Mark-II subassemblies, previously removed as leak suspects, were returned to the core for this run.

Additional details of the fuel handling for this period are as follows:

For Run 49A: Two Mark-II driver subassemblies were installed, and one was removed. One subassembly of impact-bonded vendor fuel and one of heat-treated vendor fuel were also removed. For Run 49C: Six surveillance subassemblies of vendor fuel were removed. For Run 50A: One surveillance subassembly of heat-treated vendor fuel was reinstalled for additional irradiation. Several outer-blanket subassemblies in Row 8,

which were approaching their burnup limit, were exchanged with blanket subassemblies in Row 14. For Run 50E: The high-worth control rod was replaced.

Changes in experimental-irradiation subassemblies are covered under Sect. I.A.4.

2. Fuels and Examination Facility Operations. M. J. Feldman (02-076)

a. Fuel Assembly. D. L. Mitchell (Last reported: ANL-7825, p. 1.2)

Seventeen Mark-IA subassemblies were assembled in the cold line during this reporting period. All were made up of centrifugally bonded vendor elements that had been heat-treated by ANL (see Sect. I.A.3.a).

Table I.1 summarizes the production activities for May 16 through July 15, 1971, and for fiscal years 1971 and 1972.

TABLE I.1. Production Summary for FEF Cold Line

	FY 1971		FY 1972	
	5/16/71 through 6/30/71	Total for FY 1971	7/1/71 through 7/15/71	Total for FY 1972
Subassemblies Fabricated with Mark-IA Fuel				
With cold-line elements	0	2	0	0
With vendor elements	13	106	9	9
Preirradiation Treatment of Vendor Mark-IA Fuel				
Heat-treating of as-fabricated elements ^a				
Heat-treated, inspected, and accepted ^b	2,623	20,103	562	562
Heat-treated, inspected, and rejected ^c	277	1,655	205	205
Total Elements Available for Subassembly Fabrication as of 7/15/71				
Cold-line fuel				
Mark IA			199	
Mark II			189	
Vendor fuel (Mark IA)				
Impact-bonded ^d			205	
Heat-treated ^b			16,138	

^a These elements, cast and centrifugally bonded by the vendor, have been accepted by ANL verification inspection, but not yet approved for general use in the reactor. They are being heat-treated to reclaim them. (See Sec. I.A.3.a.)

^b Includes elements previously rejected for void size, but found acceptable on retesting of the sodium bond. (See footnote c.)

^c Void size in the sodium bond is the principal cause for rejection. The bonds in elements rejected for this reason are being retested (see Sec. I.A.3.a); those rejected after this reevaluation may be reclaimed by impact-bonding.

^d Impact-bonding by ANL of 11,853 unbonded vendor fuel elements was completed in fiscal year 1970.

- b. Reactor Support. J. P. Bacca and N. R. Grant (Last reported: ANL-7825, p. 1.5)

(1) Fabrication of Tantalum-drop-rod Subassembly (N. R. Grant). A drop-rod subassembly containing three tantalum slugs and one stainless steel slug (see ANL-7758, p. 57) has been fabricated. It will be used for reactivity tests in the reactor in place of the drop rod now being used, which contains stainless steel slugs only. The drop rod was satisfactorily flow-tested by the EBR-II Experimental Irradiation and Testing Group and then was sent to the special-materials vault for interim storage.

3. Fuel and Hardware Procurement. M. J. Feldman (02-073)

- a. Reclamation of Vendor Fuel. D. L. Mitchell (Last reported: ANL-7825, p. 1.50)

During this reporting period, heat-treating of the centrifugally bonded vendor elements to reclaim them was completed. (See Table I.1 for number of elements heat-treated, inspected, and shown to be "accepts" or "rejects" in this reporting period.) Of the 22,650 elements initially available at the beginning of this reclamation program, 22,525 were heat-treated and examined. (The other 125 elements were used for other purposes, except for 18 that were damaged in shipping and handling.) Their examination to date shows 20,665 elements to be "accepts." Of these, 4527 were used in subassemblies for in-reactor tests.

Elements were rejected principally for the size of the voids in the sodium bond; the acceptable void size was based on Revision 6 of Specification FCF-1 (Product Specification for EBR-II Driver Fuel Elements). A new type of bond tester, now in operation, can measure the larger void sizes that are acceptable under Revision 7 of FCF-1. The elements that were rejected under Revision 6 will be reevaluated for void size in the new tester. Rejected elements from the new tester and those elements rejected for traps and bubbles will be impact-bonded (1000-2000 impacts at ~500°C) in an effort to reclaim them, after which their bonds will be retested. Elements rejected after the impact-bonding operation will not be subjected to any additional reclamation processing to salvage them.

4. Reactor Plant Services for Experimenters. R. Neidner (02-204; last reported: ANL-7825, p. 1.6, under Experimental Irradiation and Testing)

Table I.2 shows the status of experimental irradiations in EBR-II on July 15, after Run 50E. The footnotes for the table summarize the removals and reinsertions of experimental-irradiation subassemblies during the search for a fission-product leaker. Subassembly X082A was identified as the most probable leaker, and its irradiation was terminated at the end of Run 50E. (See also Sect. I.A.1.a)

TABLE I.2. Status of Experimental Irradiations in EBR-II as of July 15, 1971
(Run 50E Completed)

Subassembly No. and (Position)	Date Loaded	Content and (Number of Capsules)	Experi- menter	Accumulated Exposure, MWd	Estimated Goal Exposure, MWd	Burnup ^a
XX03 (5F3)	5/14/71	Structural (5)	HEDL	1,752	6,200	0.6
XG03A (8D2)	9/14/70	UO ₂ -20 wt % PuO ₂ (2)	GE	4,861	13,000	0.8+7.5 ^b = 8.3
XG04A (8A7)	9/15/70	UO ₂ -20 wt % PuO ₂ (2)	GE	4,861	21,000	0.8+8.5 ^b = 9.3
X055A (7E5)	3/16/71	(U _{0.85} -Pu _{0.15}) ^C (19)	UNC	3,206	15,000	0.8+4.8 ^b = 5.6
X058 ^{c,d} (7B6)	4/24/69	UO ₂ -25 wt % PuO ₂ (37)	GE	18,789	21,800	6.5
X068A (6B4)	2/23/71	Mark IA (61)	ANL	3,632	9,300	0.8+2.4 ^b = 3.2
X069A (6F4)	4/22/71	UO ₂ -25 wt % PuO ₂ (37)	HEDL	2,414	16,000	0.6+2.9 ^b = 3.5
X071A (6C4)	3/29/71	Mark II (37)	ANL	3,206	5,800	1.1+6.6 ^b = 7.7
X074A (6A5)	5/16/71	UO ₂ -25 wt % PuO ₂ (37)	HEDL	1,752	10,000	0.7+3.4 ^b = 4.1
X076 (7A2)	3/27/70	UO ₂ -25 wt % PuO ₂ (19)	WARD	10,413	15,000	3.4
X079 ^e (4B2)	4/17/70	(U _{0.85} -Pu _{0.15}) ^C (19)	UNC	10,821	11,000	5.6
X081 ^{d,f} (7F6)	5/24/70	UO ₂ -25 wt % PuO ₂ (9)	GE	8,189	19,000	2.6+6.7 ^b = 9.3
X082A ^g (5A4)	2/23/71	Mark IA (61)	ANL	2,955	4,500	0.5+2.8 ^b = 3.3
X083 ^d (5E2)	9/15/70	Mark IA (61)	ANL	5,443	13,900	1.5
X086 ^e (5D4)	8/7/70	(U _{0.8} -Pu _{0.2}) ^N (10)	BMI	6,776	7,000	3.2
		(U _{0.8} -Pu _{0.2}) ^C (5)	LASL			3.2
		(U _{0.8} -Pu _{0.2}) ^C (4)	WARD			2.9

TABLE I.2 (contd)

Subassembly No. and (Position)	Date Loaded	Content and (Number of Capsules)	Experi- menter	Accumulated Exposure, MWd	Estimated Goal Exposure, MWd	Burnup ^a		
X087A	(6C2)	10/27/70	UO ₂ -25 wt % PuO ₂	(61)	HEDL	4,699	19,000	1.0+1.1 ^b = 2.1
X088	(7C4)	5/24/70	UO ₂ -25 wt % PuO ₂	(19)	WARD	8,912	14,500	2.1
X089	(2F1)	9/15/70	Structural	(7)	HEDL	6,249	7,800	2.6
X090	(7D5)	9/15/70	Structural	(4)	BMI	6,249	6,700	1.3
			Structural	(1)	INC			1.3
			Structural	(1)	ORNL			1.3
			Structural	(1)	HEDL			1.3
X091	(4B3)	9/11/70	Structural	(7)	HEDL	6,249	16,000	2.3
X093	(6E4)	10/27/70	UO ₂ -25 wt % PuO ₂	(61)	HEDL	4,699	16,000	1.6
X094 ^{d, f}	(7B4)	11/16/70	UO ₂ -15 wt % PuO ₂	(7)	GGA	1,613	8,600	0.5
X095	(7A5)	9/18/70	Structural	(1)	NRL	6,230	11,000	1.3
X097	(5A2)	3/18/71	UO ₂ -25 wt % PuO ₂	(61)	HEDL	3,219	14,000	1.3
X098	(4C2)	11/16/70	Structural	(19)	GE	3,724	8,000	1.4
X099	(7F5)	11/16/70	Boron Carbide	(6)	ORNL	3,724	20,000	0.8
X100	(2D1)	10/7/70	Structural	(7)	ORNL	5,479	10,000	2.3
X102	(7F1)	2/22/71	Chromium Corrosion	(1)	ANL	3,724	10,000	0.5
X110	(7C5)	2/22/71	Structural	(7)	INC	3,724	7,500	0.8
X112	(6B2)	5/12/71	UO ₂ -20 wt % PuO ₂	(19)	ORNL	1,752	10,000	0.6
			UO ₂ -20 wt % PuO ₂	(18)	B&W			0.6

TABLE I. 2 (contd)

Subassembly No. and (Position)	Date Loaded	Content and (Number of Capsules)	Experi- menter	Accumulated Exposure, MWd	Estimated Goal Exposure, MWd	Burnup ^a	
X113 ^h	(6F1)	4/22/71	UO ₂ -20 wt % PuO ₂ (13) UO ₂ -20 wt % PuO ₂ (5) Structural (1)	ANL ANL/NUMEC ANL	1,670	10,000	0.7+3.7 ^b = 4.4 0.5+9.8 ^b = 10.3 0.4+2.4 ^b = 2.8
X115	(6D1)	4/21/71	UO ₂ -25 wt % PuO ₂ (37)	WARD	2,414	14,000	0.8
X117 ⁱ	(8B2)	2/24/71	UO ₂ -25 wt % PuO ₂ (9)	GE	2,826	30,000	0.5+4.9 ^b = 5.4
X120	(7E3)	5/6/71	Boron Carbide (6) Tantalum (1)	HEDL HEDL	1,764	4,000	0.4 0.4
X123	(2B1)	7/2/71	Structural (1)	HEDL	241	3,100	0.1
X133	(7B3)	7/1/71	Structural (37)	ANL	241	1,500	~0

^aEstimated accumulated center burnup on peak rod, based on unperturbed flux, but considering depletion effects (fuels, at. %; nonfuels, nvt x 10⁻²²).

^bPrevious exposure from another subassembly.

^cIn storage basket during runs 50A, 50C, and 50E.

^dInstalled for run-50F startup.

^eTerminated after run 50A.

^fIn storage basket during runs 50A, 50D, and 50E.

^gTerminated after run 50E.

^hIn storage basket during runs 50B, 50C, 50D, and 50E.

ⁱTemporarily stored in position 14C7 since run 50A.

5. Operations in Support of Experimental Irradiations (02-206)

a. Operational In-cell Handling and Examination Equipment.

M. J. Feldman (Last reported: ANL-7798, p. 42, under 4. Hot Fuel Examination Facilities; a. Improvement of the FEF)

(1) Handling Subassemblies Containing Failed Fuel

(D. M. Paige). As reported in ANL-7798, provision is being made for the capability to handle an EBR-II subassembly containing a fuel failure too severe for safe handling with standard procedures and to transfer the subassembly to the FEF for in-cell disassembly and examination.

During this reporting period, the in-cell equipment for handling and storing the sodium-filled dipper (which will contain the subassembly) and the milling machine for dismantling the subassembly was received and satisfactorily tested out-of-cell. (The failed-fuel radiation shield and the gas-tight container for holding the sodium-filled dipper were received earlier and satisfactorily tested out-of-cell.) The dipper was tested with a dummy subassembly, but no sodium. In operation, the loaded dipper will be stored in a dipper-holding container placed into one of the existing floor pits in the argon cell until the subassembly is removed from the dipper for examination and disassembly. The holding container is equipped with heaters (controlled to provide a temperature of 500°F) for use if decay heat is insufficient to keep the sodium molten. Tests of the heaters showed that a temperature of 500°F could be achieved in about 5 hr. If desired, the sodium can be melted from the top down to prevent eruption of liquid sodium through the top sodium crust during heating. Forced-argon cooling of the dipper while it is in the holding container is also provided. The handling equipment and the holding container will be transferred into the argon cell soon for remote testing.

Detailed designs are complete for modifying the milling machine (which has numerical control) for remote operation and for a fixture to hold the subassembly during milling. After the mill is modified and the holding fixture is fabricated, extensive machining mockup tests, initially out-of-cell, will be performed.

As reported in ANL-7798, neutron radiography is one of the procedures being considered for nondestructive examination of the subassembly. The existing argon-cell isotopic neutron source was to have been used. Tests using a subassembly mockup and a neutron source equivalent in strength to that expected from the argon-cell source showed that the definition would be insufficient for obtaining data for the fuel failure. Therefore, the use of the argon-cell source for nondestructive examination is being reconsidered. Detailed designs are complete for the other examination equipment.

- b. Experimental Support. M. J. Feldman, J. P. Bacca, and N. R. Grant (Last reported: ANL-7825, p. 1.10)

Table I.3 lists the new subassemblies that were made up with new capsules or elements and sent to the reactor or to the special-materials vaults for interim storage until needed for the reactor.

TABLE I.3. New Subassemblies Fabricated in the FEF

Subassembly No. (and Type)	Content and (Number) of Capsules or Elements
X107 (B61A) ^a	HEDL mixed-oxide fuel elements (58); dosimetry elements (3)
X123 (M1A) ^a	HEDL structural-materials capsule (1)
X125, X128, X129, X130, X131, X132 (B19) ^b	In each: ANL-EBR-II dosimetry capsules (3); dummy elements (16)
X126 (driver) ^b	ANL-EBR-II dosimetry capsules (5), including one each in the upper and lower reflector shields; Mark-IA fuel elements (88)
X127 (driver) ^b	ANL-EBR-II dosimetry capsules (3); Mark-IA fuel elements (88)
X133 (L37) ^a	ANL pressurized Creep-IIB capsules (34); dummy elements (3)

^aSubassembly sent to reactor.

^bSubassembly sent to the special-materials vaults for interim storage until needed for the reactor.

B. Fuels and Materials Studies

1. Coolant Chemistry. D. W. Cissel (02-609)

- a. Monitoring of Sodium-coolant Quality. W. H. Olson, C. C. Miles, and T. P. Ramachandran (Last reported: ANL-7825, p. 1.13)

Tables I.4 and I.5 give information pertaining to the taking of the primary- and secondary-sodium samples whose analyses are reported below.

(1) Radionuclides in Sodium. Table I.6 lists results of analyses for ¹³⁷Cs and ¹³¹I in the primary sodium. An increase in ¹³⁷Cs activity is evident, beginning with the June 7 sample. The increase was coincident with increased xenon activity in the cover gas. (See Sect. I.A.1.a.)

Table I.7 lists total activities of activation products in the 86,000 gal of primary sodium. Determinations were made on vacuum-distillation residues from the samples.

TABLE I.4. Sampling of Primary Sodium

Sample Date	Analysis for	Sampling Method ^a	Sample Vessel	Sample Flow, gpm	Flush Time, min	Sample Temp, °F	Bulk Sodium Temp, °F
4/29/71	Tritium	of	Quartz beaker	0.4	15	580	680
5/5/71	¹³⁷ Cs and ¹³¹ I	of	Pyrex beaker	0.4	15	515	565
5/13/71	Trace metals and activation products	of	Ti cup	0.6	15	505	575
5/14/71	¹³⁷ Cs and ¹³¹ I	of	Pyrex beaker	0.8	15	460	565
	Carbon and oxygen	ft	SS extrusion vessel	0.8	15	465	565
5/19/71	¹³⁷ Cs and ¹³¹ I α activity	of	Pyrex beaker	0.6	15	580	700
	Cadmium and zinc	of	Pyrex beaker				
		of	Quartz beaker				
5/24/71	¹³⁷ Cs and ¹³¹ I Tritium	of	Pyrex beaker	0.7	15	600	695
	Boron	of	Quartz beaker				
		of	Ta cup				
5/28/71	¹³⁷ Cs and ¹³¹ I	of	Pyrex beaker	0.7	15	590	700
6/1/71	¹³⁷ Cs and ¹³¹ I	of	Pyrex beaker	0.7	15	590	695
6/2/71	Plutonium	of	Ti cup	0.7	15	590	695
6/4/71	¹³⁷ Cs and ¹³¹ I	of	Pyrex beaker	0.7	15	590	700
6/7/71	¹³⁷ Cs and ¹³¹ I	of	Pyrex beaker	0.7	15	580	695
6/8/71	¹³⁷ Cs and ¹³¹ I	of	Pyrex beaker	0.7	15	590	695
6/11/71	¹³⁷ Cs and ¹³¹ I	of	Pyrex beaker	0.7	15	580	695
	Carbon and oxygen	ft	SS extrusion vessel	0.7	240	540	695
6/14/71	¹³⁷ Cs and ¹³¹ I	of	Pyrex beaker	0.5	15	580	695
6/18/71	¹³⁷ Cs and ¹³¹ I Potassium	of	Pyrex beaker	0.7	15	580	695
		of	Pyrex beaker				
	Activation products	of	Ti cup	0.6	15	580	690
6/23/71	¹³⁷ Cs and ¹³¹ I Plutonium	of	Pyrex beaker	0.6	15	600	695
	Tritium	of	Ta cup				
		of	Quartz beaker				
6/28/71	¹³⁷ Cs and ¹³¹ I Nitrogen	of	Pyrex beaker	0.5	15	580	695
		of	Quartz beaker				
7/2/71	Trace metals and activation products	of	Ti cup	0.5	30	580	695

^a of = overflow; ft = flow-through.

TABLE I.5. Sampling of Secondary Sodium

Sample Date	Analysis for	Sampling Method ^a	Sample Vessel	Sample Flow, gpm	Flush Time, min	Sample Temp, °F	Bulk Sodium Temp, °F
4/29/71	Tritium	of	Quartz beaker	0.7	18	420	490
5/11/71	Carbon and oxygen	ft	SS extrusion vessel	0.8	15	440	470
5/13/71	Trace metals	of	Ta cup	0.6	15	435	465
5/19/71	Silicon	of	Ta cup	0.7	15	425	490
5/20/71	Boron	of	Ta cup	0.7	15	420	460
5/24/71	Tritium	of	Quartz beaker	0.7	15	430	490
6/7/71	Carbon and oxygen	ft	SS extrusion vessel	0.8	15	440	485
6/16/71	Trace metals	of	Ta cup	0.6	15	420	450
6/17/71	Nitrogen	of	Quartz beaker	0.7	15	430	440
6/18/71	Boron	of	Ta cup	0.7	15	420	440
6/23/71	Tritium	of	Quartz beaker	0.4	17	485	485
6/24/71	Silicon	of	Ta cup	0.7	15	460	485
7/13/71	Trace metals	of	Ta cup	0.6	30	440	460

^aof = overflow; ft = flow-through.

TABLE I.6. ¹³⁷Cs and ¹³¹I in Primary Sodium

Sample Date	Sample Size, g	¹³⁷ Cs, nCi/g	¹³¹ I, pCi/g
5/5/71 ^a	12.6	17	110
5/14/71	12.1	17	58
5/19/71	13.6	16	25
5/24/71	11.6	17	66
5/28/71	13.5	17	72
6/1/71	13.0	18	147
6/4/71	13.0	17	97
6/7/71	11.3	20	31
6/8/71	12.5	22	463
6/11/71	12.8	23	294
6/14/71	13.0	21	196
6/18/71	10.5	22	113
6/23/71	13.1	21	82
6/28/71	11.5	23	68

^aTaken from FERD loop; all other samples taken from purification loop.

TABLE I.7. Activation Products in 86,000 gal of Primary Sodium

Sample Date	Sample Size, g	Total Activity, Ci				
		^{110m}Ag	^{54}Mn	^{125}Sb	^{117}Sn	^{113}Sn - ^{113m}In
5/13/71	56.5	0.18	0.008	0.15	1.2	1.65
6/18/71	24.2	0.16	0.020	0.03	1.0	1.60
7/2/71	55.4	0.19	0.017	0.24	1.4	1.79

A sample of primary sodium taken May 19 was analyzed for α reactivity. The activity of ^{210}Po was 67 dis/min-g. Plutonium activity for this sample and two others (taken June 2 and 23) was <1 dis/min-g.

Table I.8 lists results of analyses for tritium in the primary and secondary sodium. In addition, samples of steam and condensate from the power cycle have been analyzed for tritium present during periods of operation and outage of the secondary-sodium cold trap. Table I.9 lists the results of these analyses. These data show that concentration of tritium in the steam system is a function of trap operation.

(2) Trace Metals in Sodium. Table I.10 lists results of analyses for trace metals in the primary and secondary sodium. Concentrations are measured by atomic-absorption spectrophotometry on vacuum-distillation residues. Both values for lead in the primary sodium are lower than normal. (See footnotes for the table.)

Cadmium, zinc, and potassium cannot be determined from distillation residues. Cadmium and zinc are separated from sodium by solvent extraction and measured by atomic-absorption spectrophotometry.

TABLE I.8. Tritium in Sodium

Sample Date	Primary Sodium		Secondary Sodium	
	Sample Size, g	Tritium, $\mu\text{Ci/g}$	Sample Size, g	Tritium, $\mu\text{Ci/g}$
4/29/71	5.5	4.2×10^{-2}	3.6	6.7×10^{-3}
5/24/71	3.5	6.3×10^{-2}	3.3	9.2×10^{-3}
6/23/71	Sample no good		3.4	2.9×10^{-3}

TABLE I.9. Tritium Content of Steam System,
with and without Operation of the
Secondary-sodium Cold Trap

Sample Date	Tritium in Steam, pCi/ml	Tritium in Turbine Condensate, pCi/ml	Secondary Cold Trap Operating?
4/20/71	12	13	Yes
4/23/71	9	8	Yes
4/26/71	14	14	Yes
4/27/71	18	17	Yes
4/28/71	18	17	No
4/29/71	20	18	No
5/3/71	31	29	No
5/4/71	33	34	No
5/19/71	73	74	No
5/21/71	64	62	No
5/24/71	74	75	No
5/24/71	75	72	No
5/26/71	83	72	Yes
6/7/71	17	13	Yes
6/21/71	9	13	Yes
6/22/71	12	11	Yes
6/23/71	11	13	Yes
6/24/71	13	13	Yes

TABLE I.10. Trace Metals in Sodium

Sample Date	Sample Size, g	Concentration, ppm														
		Ag	Al	Bi	Ca	Co	Cr	Cu	Fe	In	Mg	Mn	Mo	Ni	Pb	Sn
<u>Primary Sodium</u>																
5/13/71	56.5	0.07	<0.6	3.2	<0.02	<0.02	0.02	0.04	0.97	<0.06	0.013	0.009	<0.07	<0.04	5.0 ^a	26.9
7/2/71	55.4	0.13	<0.6	1.1	<0.01	<0.02	<0.02	0.03	0.45	<0.06	0.018	0.005	<0.07	<0.04	1.8 ^b	25.5
<u>Secondary Sodium</u>																
5/13/71	53.6	0.16	<0.6	<0.1	0.04	<0.02	0.06	0.05	1.27	<0.06	0.038	0.021	<0.07	0.06	0.20	<0.5
6/16/71	57.0	0.05	<0.6	<0.1	0.11	<0.02	0.05	<0.02	0.23	<0.06	0.028	<0.006	<0.07	<0.04	0.18	<0.5
7/13/71	57.6	0.08	<0.6	<0.1	0.02	<0.02	0.03	0.02	0.21	<0.06	0.032	0.014	<0.07	<0.04	0.23	<0.5

^aThe primary-sodium bulk temperature was ~575°F; this may account for the low lead value.

^bThis sample may have been overheated during distillation. A 10-g sample taken 7/16/71 yielded 11 ppm lead.

Potassium is determined by flame spectrophotometry without separation from sodium. Results of analyses for the three trace metals in primary sodium were:

5/19/71 sample	Cd 0.02 ppm; Zn < 0.06 ppm
6/18/71 sample	K 165 ppm

(3) Carbon and Oxygen in Sodium. Table I.11 lists results of analyses for carbon and oxygen in the primary and secondary sodium. Samples of ~15 g are extrusion-aliquoted for analysis. Carbon is determined by the oxyacidic-flux method, and oxygen by the mercury-amalgamation method.

TABLE I.11. Carbon and Oxygen in Sodium

Sample Date	Carbon		Oxygen	
	Number of Aliquots ^a	Average Concentration, ppm	Number of Aliquots ^a	Average Concentration, ppm
<u>Primary Sodium</u>				
5/14/71	3	1.0 ± 0.5	3	1.6 ± 0.6
6/11/71	3	1.1 ± 0.2	3	1.2 ± 0.3
<u>Secondary Sodium</u>				
5/11/71	3	1.6 ± 0.2	3	1.3 ± 0.9
6/7/71	3	1.3 ± 0.4	4	1.0 ± 0.5

^aAliquot size ~1 g.

(4) Nitrogen in Sodium. Table I.12 lists results of analysis for nitrogen in the primary and secondary sodium. Nitrogen is determined by the Kjeldahl method.

TABLE I.12. Nitrogen in Sodium

Primary Sodium			Secondary Sodium		
Sample Date	Sample Size, g	Nitrogen, ppm	Sample Date	Sample Size, g	Nitrogen, ppm
6/28/71	12.1	<0.1	6/17/71	11.8	<0.1

(5) Silicon in Sodium. Because of sampling problems, the primary sodium was not analyzed for silicon. Two samples of secondary sodium were analyzed for silicon with the following results:

5/19/71 sample	Si 0.4 ppm
6/24/71 sample	Si 4.4 ppm

(6) Boron in Sodium. Because of sampling problems, the primary sodium was not analyzed for boron. Two samples of secondary sodium were analyzed for boron with the following results:

5/20/71 sample	B < 0.05 ppm
6/18/71 sample	B < 0.05 ppm

- b. Radioactivity of EBR-II Primary-system Components.
C. R. F. Smith, E. R. Ebersole, and H. Hurst (Last reported:
ANL-7798, p. 12)*

Radioactivity measurements made of components during fiscal year 1971 and not previously reported are summarized below.

(1) Primary Pump No. 1. This 5000-gpm (nominal) centrifugal-pump assembly was removed from the primary tank on December 27, 1970, for repair and maintenance. The results of a radiation survey of the uncleaned assembly were reported in ANL-7798. The assembly was cleaned using a procedure consisting of: (a) conversion of residual sodium to sodium oxide in a dry air-argon atmosphere; (b) disassembly into component parts (impeller shaft, baffle assembly, and pump case), followed by a series of alcohol-water rinses of each component; (c) scrubbing of exposed surfaces of each component in hot ammonium citrate-oxalate cleaning solution; and (d) rinsing in hot water and ethyl alcohol, followed by drying in air.

Each component, before and after cleaning, was axially scanned for radioactivity by moving the component past a GeLi gamma-ray detector. Other than ^{22}Na , which was totally removed in the cleaning process, the principal activities found on the uncleaned pump were (in decreasing order of importance) ^{54}Mn , ^{60}Co , ^{137}Cs , and ^{182}Ta . On the uncleaned surfaces, ^{182}Ta was less than a tenth that of ^{54}Mn . The cleaning process removed 44-67% of the ^{54}Mn , 42-92% of the ^{60}Co , and ~65% of the ^{137}Cs , but no significant amount of ^{182}Ta . Tantalum-182 is formed by the reaction $^{181}\text{Ta}(n,\gamma)^{182}\text{Ta}$. The source of tantalum is believed to be the cladding of the antimony neutron source used in EBR-II.

Radioactive deposits of ^{137}Cs , ^{54}Mn , and ^{60}Co were found on uncleaned surfaces in the cover-gas region in the primary tank. The major

*The results of gamma-scanning the irradiated-fuel-monitor thimble are given in ANL-7776 (p. 26).

activity was ^{137}Cs , which, because of its volatility, is assumed to have been transported from the sodium pool by vaporization-deposition. The mechanism by which ^{54}Mn and ^{60}Co appear on surfaces in the primary tank exposed only to the cover gas is not understood and needs to be explored.

(2) Pump Duct of FERD Loop. The pump duct of the FERD (fuel-element rupture detector) loop is a component of the delayed-neutron detection system that continuously samples primary sodium from the effluent of the EBR-II intermediate heat exchanger. The duct (fabricated from Type 304 stainless steel) was replaced in April 1970 after an estimated 210 million gallons of 700°F primary sodium had passed through it.

After the duct was removed from the FERD system, the small amount of sodium remaining in it was removed by heating and draining. The duct was scanned for radiation with a GeLi detector before and after washing it with ethyl alcohol and water. These washes removed 28% of the initial ^{54}Mn and 52% of the initial ^{60}Co . No ^{137}Cs was detected in either scan.

(3) Primary-purification-system Cold Trap. In March, after EBR-II had been shut down more than three months, the perimeter of the primary-purification-system cold trap was monitored with a radiation survey meter (Juno Model 7). Measurements were taken on 6-in. centers 2 in. from the surface of the insulation. From these measurements, an isodotic map was prepared. This map showed two centers where radioactivity was two to three times as great as the general level of about 100 mR/hr. One of these centers was near the bottom of the tank, where radioactivity was expected to be greatest owing to coprecipitation and adsorption of radionuclides on sodium oxide precipitates. The other center of activity was on the opposite side of the tank and near its upper edge. The reason for high radiation in this zone is not known at present.

Figure I.1 is a cutaway view of the trap. Figure I.2 shows the isodotic map.

2. Materials-Coolant Compatibility. D. W. Cissel (02-610)

- a. Evaluation and Surveillance of EBR-II Materials. D. W. Cissel and W. E. Ruther (Last reported: ANL-7825, p. 1.20)

(1) Examination of IHX Drain Tube (Not previously reported). This long tube, which had extended down into the IHX (intermediate heat exchanger), was removed from EBR-II last winter. Markings still visible after nearly eight years in sodium service identified the tubing as SPEC-ASTM-A213 TMI HEAT W93899 1 OD x 0.065. This specification is for Type 304 stainless steel seamless tubing made from an electric-furnace melt. Secondary sodium at temperatures from 610 to 650°F had flowed past

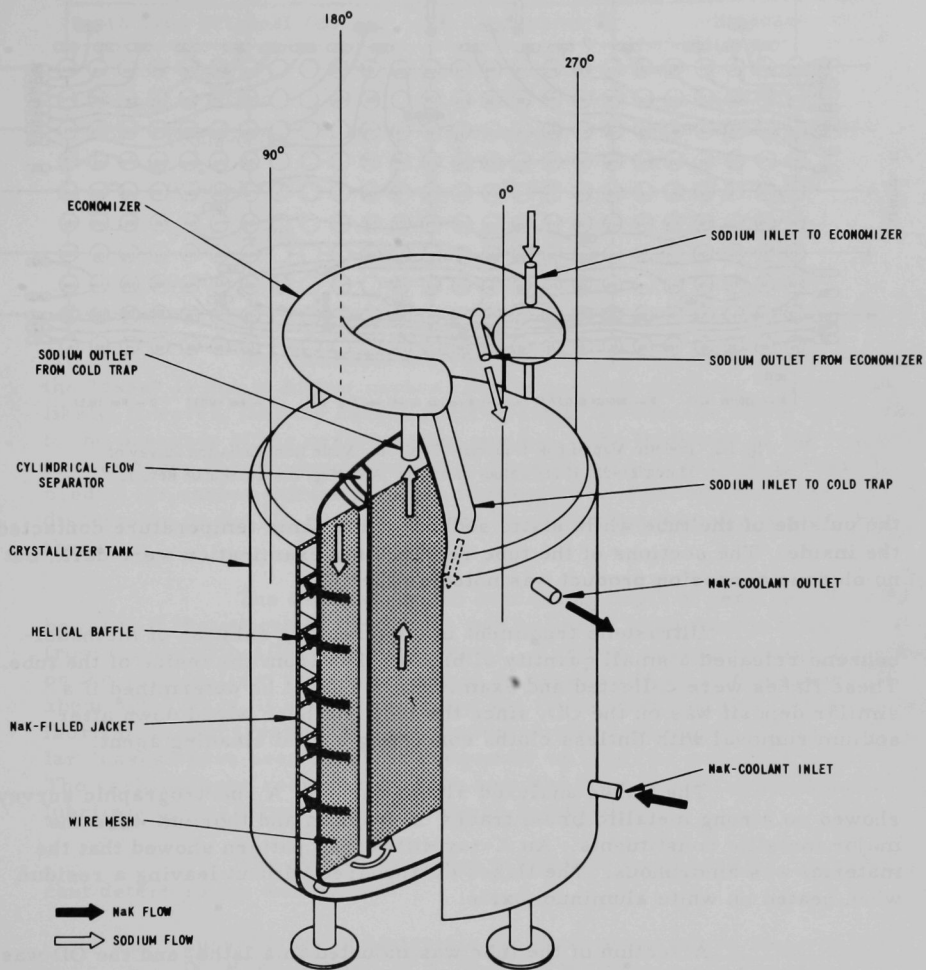


Fig. I.1. EBR-II Primary Cold Trap. ANL Neg. No. 103-P5007.

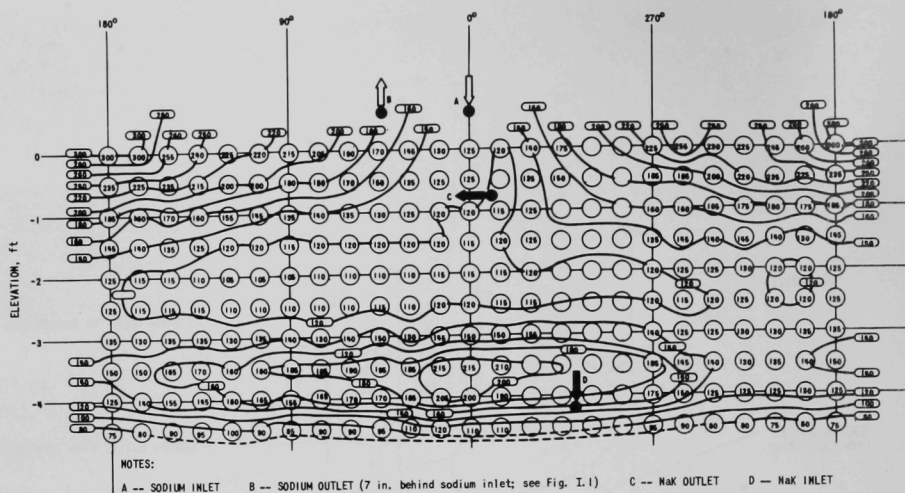


Fig. I.2. Isodose Map of EBR-II Primary Cold Trap Made from Radiation Survey of March 25-29, 1971; Values in mR/hr. ANL Neg. No. 103-P5008 Rev. 1.

the outside of the tube while static sodium at the same temperature contacted the inside. The sections of the tube received for examination were dark, but no obvious corrosion product was noted on the OD.

Ultrasonic treatment in a degreasing solution of methanol-benzene released a small quantity of black flakes from the inside of the tube. These flakes were collected and examined. It cannot be determined if a similar deposit was on the OD, since the tube had been wiped down after sodium removal with lintless cloths containing a mild cleaning agent.

The flakes analyzed 51% of carbon. A spectrographic survey showed no strong metallic lines; traces of uranium and thorium were the major metallic constituents. An X-ray diffraction pattern showed that the material was amorphous. The flakes disappeared without leaving a residue when heated on white aluminum oxide.

A section of the tube was mounted in a lathe, and the OD was machined off in 0.002-in.-thick cuts. The turnings were collected and analyzed for carbon and nitrogen. The surface cutting resulted in occasional release of a fine, black powder into the air, which resembled the sooty, airborne particles from an improperly adjusted acetylene flame. Table I.13 gives the chemical analyses of the lathe turnings.

Metallographic specimens of the tube wall showed a non-sensitized structure, as expected from the service temperature. The OD of the tubing had a "case" of about 0.0004 in., which polished differently from the rest of the tube. No such "case" was found on the ID.

TABLE I.13. Chemical Analyses of Turnings from the IHX Drain Tube

Depth from Original OD, in.	Carbon, wt %	Nitrogen, wt %
0-0.002	0.148	0.034
0.002-0.004	0.039	0.036
0.004-0.006	0.029	0.035
0.006-0.008	0.028	0.034
0.008-0.010	0.028	0.034

The chemical analyses (Table I.13) strongly suggest that the "case" is due to higher carbon content near the surface. It seems unlikely, however, that the carbon enrichment at the surface of the OD is due to the presence of the carbonaceous residue. The thickness of the "case" is over twice the maximum depth that the data of Agarwala et al.* would predict for carbon diffusion at this temperature. Further, no "case" is discernible on the ID, even though the black residue was at a maximum there.

The same argument concerning depth of penetration could be made if the source of the "case" was assumed to be carbon transported from the ferritic-alloy steam generator. Further, carbon residue deposited on the surface from the sodium would be expected to be 100% carbon, not about 50%. Thus, it seems likely that the tubing acquired this "case" during fabrication heat treatment, when the temperature was much higher. Similar "cases" have been observed frequently on other as-received tubing. The carbonaceous residue may have resulted from the decomposition of a lubricant or preservative on the tube as installed.

The overall condition of the tube was excellent; no significant deterioration was evident.

- b. Surveillance of Materials for High-temperature Experiments.
D. W. Cissel and W. E. Ruther (Not previously reported)

Fabrication of the first Mark-K1 materials-irradiation sub-assembly was completed, and the subassembly was loaded with Types 304, 304L, 316, and 316L stainless steel specimens. The subassembly exposes these specimens to flowing primary sodium at 1250°F. It achieves this high temperature by using gamma heating of thermally insulated stainless steel susceptors.

*R. P. Agarwala, M. C. Naik, M. S. Anand, and A. R. Paul, Diffusion of Carbon in Stainless Steels, J. Nucl. Mater. 36, pp. 41-47 (1970).

Because of uncertainties in calculating gamma heating, temperature monitors were incorporated immediately adjacent to the specimens. Four types of monitors are used in this first experiment. Two of the types are based on the difference in the expansions of stainless steel and sodium, one on the irradiation damage of silicon carbide powder, and the fourth type on the melting of selected alloy wires.

The completed subassembly is undergoing nondestructive acceptance tests at the EBR-II site.

- c. Assistance to Sodium Technology: CCTL Evaluation.
D. W. Cissel and S. Greenberg (Not previously reported)

The Core Component Test Loop (CCTL) is a large, high-temperature sodium facility operated by the Engineering and Technology Division. A 6300-hr, 1100°F test of an FFTF Mark-II subassembly has recently been completed, and it is important to know if this test degraded the mechanical properties of the Type 304 stainless steel material of construction.

Accordingly, tensile specimens machined from 5 in., Schedule 10, Type 304 stainless steel pipe exposed in the loop sodium during testing of the Mark-II subassembly were tested at room temperature (in air) and at 1060°F (in vacuum). The purpose was to compare these results with results of similar tests on identical material obtained after a previous 3500-hr exposure at 1050°F.

Table I.14 summarizes the results of both series of tests. It is apparent that there has been no serious degradation of properties.

TABLE I.14. Results of Tensile Tests of CCTL Samples

Exposure ^a	Tested at Room Temperature			Tested at 1060°F		
	Ultimate Strength, psi	Yield Strength, psi	Elongation, %	Ultimate Strength, psi	Yield Strength, psi	Elongation, %
3500 hr at 1050°F	96,000	31,000	42	54,000	31,000	26
3500 hr at 1050°F + 6300 hr at 1100°F	93,000	47,000	41	53,000	27,000	29

^aAdditional exposure of about 1200 hr at a temperature somewhat above 700°F should be added to each exposure listed.

The work described here is part of an overall program being carried out in cooperation with the Engineering and Technology Division, the Materials Science Division, and the Chemical Engineering Division.

3. Metal Driver Fuel Development and Application. C. M. Walter (02-145)

a. Mark-IA Fuel. N. J. Olson (Last reported: ANL-7798, p. 24)

(1) Diameter Behavior of Impact-bonded Vendor Fuel at 1.8 at. % Burnup, for 50- and 62.5-MWt Operation. Table I.15 lists ranges of measured values of $\Delta D_{\max}/D_0$ for Mark-I impact-bonded AGC driver-fuel elements at a maximum burnup of ~1.8 at. %. The table also gives statistical parameters developed from the values. The data have been used to compare the performance of the elements at 50 and 62.5 MWt.

The preirradiation diameters of the elements in Subassemblies C-2266 (50 MWt) and C-2267 (62.5 MWt) were not measured. Instead, they were calculated by a computer fitting routine that assumes the diameter in the plenum region to be unchanged with irradiation.

The preirradiation diameters of the nine elements listed in Table I.15 for Subassemblies C-2255, C-2256, and C-2257 were measured. From these and computer-fitted D_0 's for six elements in each of the three subassemblies whose D_0 's had not been measured, the average biasing effect was found to be

$$\Delta D_{\max}^{\text{Actual}}/D_0 = 1.12 \Delta D_{\max}^{\text{Fit}}/D_0 \quad (1)$$

when $\Delta D_{\max}^{\text{Fit}}/D_0 > 0.3\%$. The $\Delta D_{\max}/D_0$ values listed for Subassemblies C-2266 and C-2267 in Table I.15 were adjusted in accordance with Eq. 1. Note that the biasing effect shown by Eq. 1 pertains only to this set of data; the effect could be different for other elements. Therefore, measurements of actual ΔD_0 's before irradiation are necessary for accurate interpretation of diameter data.

No trend in $\Delta D_{\max}/D_0$ as a function of percentage exposure at 62.5 MWt was observed for Subassemblies C-2255, C-2256, and C-2257. Although not noted in Table I.15, the range for the six elements in these subassemblies whose D_0 's had not been measured fell within the tabulated statistical ranges when the fitted $\Delta D_{\max}/D_0$ values were adjusted according to Eq. 1. Although the data for C-2255 fall within the $\Delta D_{\max}/D_0$ distribution for C-2266, data from other subassemblies irradiated at 62.5 MWt indicate that no general conclusion could be made from this observation. The data for C-2255, C-2256, and C-2257 were grouped to better compare them with data for C-2267 and C-2266. The grouped averages and standard deviations are tabulated in Table I.15.

The statistical form for the representative frequency of occurrence of a given $\Delta D_{\max}/D_0$ was assumed to be described by a Weibull distribution* that has the general form

*W. Weibull, A Statistical Distribution Function of Wide Applicability, J. Appl. Mech. 18, 293 (1951).

TABLE I.15. $\Delta D_{\max}/D_o$ and Statistical Parameters for AGC Mark-IA Driver-fuel Elements

Subassembly No.	% Exposure at 62.5 MWt	Number of Elements Measured	Measured $\Delta D_{\max}/D_o$, %	$\overline{\Delta D_{\max}/D_o} = \bar{x}$, % ^a	Std. Dev. (σ), % ^a	Rank			$\overline{\Delta D_{\max}/D_o} = \bar{x}$, % ^b	Std. Dev. (σ), % ^b
						95%	Median	5%		
C-2266	0	10	0.430-0.630 ^c	0.503	0.119	$\left\{ \begin{array}{l} \eta = 0.470 \\ \beta = 5.34 \\ R = 1.03 \end{array} \right.$	0.535	0.585	0.499	0.090
							6.78	9.91		
							1.07	1.24		
C-2267 ^d	100	12	0.470-0.850 ^c	0.628	0.148	$\left\{ \begin{array}{l} \eta = 0.591 \\ \beta = 4.64 \\ R = 1.02 \end{array} \right.$	0.678	0.744	0.629	0.121
							5.78	8.24		
							1.02	1.15		
C-2255	73	3	0.419-0.720	0.566	0.151	$\left\{ \begin{array}{l} \eta = 0.638 \\ \beta = 2.98 \\ R = 0.992 \end{array} \right.$	0.807	0.935	0.730 (0.730) ^a	0.212 (0.198) ^a
C-2256	53	3	0.582-0.759	0.681	0.134		3.85	5.90		
C-2257	73	3	0.805-1.027	0.943	0.120		0.998	1.23		

^aFor assumed normal distribution.^bFor actual distribution using median rank: $\bar{x} = \eta \Gamma(1 + 1/\beta) = \text{average}$
 $\sigma^2 = \eta^2 [\Gamma(1 + 2/\beta) - (\Gamma(1 + 1/\beta))^2] = \text{variance}$ ^cBased on $\Delta D_{\max}^{\text{Actual}}/D_o = 1.12 \Delta D_{\max}^{\text{Fit}}/D_o$.^dControlled-flow subassembly to simulate 62.5-MWt conditions at 50 MWt.

$$F(x) = 1 - \exp \left[- \left(\frac{x - x_0}{\eta} \right)^\beta \right],$$

where

$$x = \Delta D_{\max} / D_0,$$

$F(x)$ = fraction of population $< x$,

x_0 = origin of the distribution,

and

$$\eta, \beta = \text{constants } (>0).$$

This form is most general in that it will fit any single-peak distribution. All the constants were determined numerically, using rank statistics* to take into account the limited sample sizes. The numerical fits of data were just as good when $x_0 = 0$ as when x_0 was allowed to vary. Hence, the fitted constants listed in Table I.15 were based on $x_0 = 0$. These represent a 90% confidence interval (i.e., 5-95% ranks). The term R, as used in Table I.15, is the "goodness-of-fit" parameter.

As a performance comparison, the experimental scatter-bands for the data are represented in Fig. I.3 along with other measurements, and the results of BEMOD calculations and of the PNL swelling

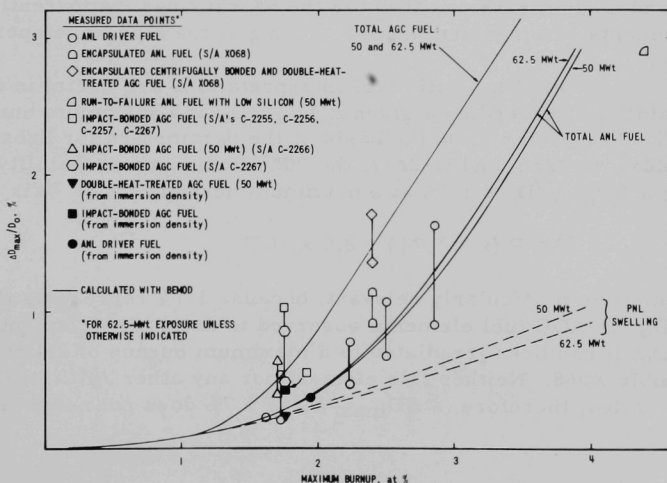


Fig. I.3. Comparison of Measured and BEMOD-calculated $\Delta D_{\max} / D_0$ for Mark-IA Fuel Elements

*L. G. Johnson, Theory and Technique of Variation Research, p. 7, Elsevier, New York (1964).

correlation.* The BEMOD calculations for the AGC fuel were made with an assumed starting fuel-pin diameter of 0.148 in. and thus reflect an earlier contact of fuel with cladding than with the normal 0.144-in.-dia pin used in the ANL-fabricated fuel elements. This larger pin diameter was used to take into account the observed U(C, O, H) surface phase on the AGC fuel elements. The cladding of all the fuel is Type 304L stainless steel.

The conclusions to be gathered from the statistical and comparative interpretations are as follows:

(a) ANL fuel elements exhibit smaller diameter increases than AGC fuel elements at a given burnup.

(b) There is a significant difference in the performance of AGC fuel elements at 50 MWt (Subassembly C-2266) and at 62.5 MWt. The $\Delta D_{\max}/D_0$ values are approximately 34% higher for the range of exposures at 62.5 MWt shown in Table I.15.

(c) There is no significant difference (95% confidence) between the data from controlled-flow subassembly C-2267 and the data obtained at 62.5 MWt (from Subassemblies C-2255, C-2256, and C-2257).

(d) The statistical interpretations of the data indicate that there is a tendency to sample $\Delta D_{\max}/D_0$ values on the high side of subassembly distribution. This is evidenced by better fits being obtained for the 95% and median rankings than for the 5% rankings. Apparently, most of the elements sampled are those operating at the highest temperatures.

(e) The statistical interpretations are useful in determining the probability of exceeding a given $\Delta D_{\max}/D_0$ at a maximum burnup of ~ 1.8 at. %. For example, on the basis of the parameters for Subassemblies C-2255, C-2256, and C-2257, the 90%-confidence probability of obtaining a $\Delta D_{\max}/D_0 \geq 1.7\%$ at a maximum burnup ~ 1.8 at. % is

$$1.5 \times 10^{-15} \leq P(x \geq 1.7\%) \leq 8.5 \times 10^{-9}.$$

This example is particularly relevant, because 1.7% represents the largest $\Delta D_{\max}/D_0$ for AGC fuel elements observed to date. One element had this $\Delta D_{\max}/D_0$; it had been irradiated to a maximum burnup of 2.4 at. % in Subassembly X068. Neither this element nor any other AGC Mark-IA element has failed; therefore, a $\Delta D_{\max}/D_0$ of 1.7% does not necessarily imply failure.

*T. T. Claudson, R. W. Barker, and R. L. Fish, The Effects of Fast Flux Irradiation on the Mechanical Properties and Dimensional Stability of Stainless Steel, Nucl. Appl. and Technol. 9, p. 10 (July 1970).

- b. Advanced Fuel (Mark II). G. L. Hofman (Last reported: ANL-7825, p. 1.21)

(1) Swelling of Cladding of Mark-II Fuel Elements. Immersion-density measurements performed by the ANL Materials Science Division on Types 316 and 304L stainless steel cladding of Mark-II elements confirm the presence of creep as a component in the deformation of the Type 304L cladding. Within the uncertainty in $\Delta D_{\max}/D_0$ values, there appears to be no creep in the Type 316 cladding.

Table I.16 and Fig. I.4 show the $\Delta D/D_0$ due to swelling, as calculated from the immersion-density measurements, and the total $\Delta D/D_0$ as measured. The last column of the table lists the $\Delta D/D_0$ due to creep.

TABLE I.16. Comparison of Measured Total $\Delta D/D_0$ with Diameter Increases Obtained from Immersion Densities

Subassembly No.	Element No.	Maximum Burnup, at. %	Maximum Neutron Fluence ($E > 0.1$ MeV), 10^{22} n/cm ²	Cladding Material (Type of Stainless Steel)	Fuel Enrichment, %	$\Delta V/V_0$, ^a %	$\Delta D/D_0$ due to Swelling, ^b %	Total $\Delta D/D_0$ Measured, %	$\Delta D/D_0$ due to Creep, %
X071	218	6.6	4.0	304L	93	4.69	1.56	2.24	0.68
X071	219	5.5	4.0	304L	80	3.92	1.31	1.72	0.41
C-2203S	64	3.2	2.9	304L	64	1.49	0.49	0.84	0.35
C-2203S	54	3.2	2.9	316	64	0.62	0.21	0.29	0.08

^a From immersion-density measurements.

^b Assumed to be 1/3 the volume change measured by immersion density.

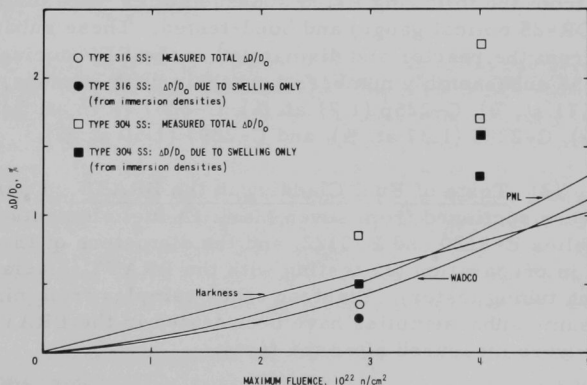


Fig. I.4. Increase in Diameter of Cladding of Mark-II Fuel with Irradiation; Curves Show Swelling as Calculated with Three Models Used in BEMOD Code

In addition to showing the presence of creep, the data indicate that the swelling behaviors of Types 316 and 304L stainless steel are different. None of the swelling models used in the BEMOD modeling code distinguishes between the two types of steel. The diameter increases due to swelling as calculated by three recent models (WADCO, PNL, and Harkness)* are shown in Fig. 1.4 for comparison. At the higher fluence, the measured swelling of Type 304L stainless steel is substantially higher than the calculated swelling. Differences in temperature arising from different fuel enrichments may account for some of the difference between the two sets of points at the fluence of 4×10^{22} n/cm². (The lower set of points is for an element containing 80%-enriched fuel, the upper set for one containing 93%-enriched fuel.) However, local variations in flux may also be important.

The few density data collected to date show that significant discrepancies are present between calculated and measured swelling of the cladding of EBR-II driver fuel. Additional density determinations and fluence measurements are being made on cladding material from other Mark-II subassemblies. These measurements should help provide the necessary information to develop an empirical model for stainless steel swelling that can be used in BEMOD calculations for driver fuel.

- c. Surveillance Support. J. P. Bacca, N. R. Grant, A. K. Chakraborty, and G. C. McClellan (Last reported: ANL-7825, p. 1.32)

Summarized here is the postirradiation surveillance work performed under the various programs of this task.

(1) Mark-IA Fuel Elements from Surveillance Subassemblies. Elements from the following listed subassemblies were diameter-measured (with the DR-25 optical gauge) and bond-tested. These subassemblies were received from the reactor and dismantled in the FEF during this reporting period. The subassembly numbers (and their peak burnups) are as follows: C-2255 (1.71 at. %), C-2256 (1.71 at. %), C-2257 (1.76 at. %), C-2277 (1.64 at. %), C-2295 (1.37 at. %), and C-2297 (1.50 at. %).

(2) Tests of Fuel Cladding in the BRATT. Fourteen cladding samples were sectioned from seven Mark-IA fuel elements selected from Subassemblies B-3120 and B-3122, and the diameters of the samples were measured in preparation for testing with the BRATT (biaxial rupture-anticipating tubing tester). Eighteen other samples from nine elements from the same subassemblies have been tested in the BRATT, and their diameters were measured after the tests.

*WADCO: J. L. Straalsund and J. F. Bates, A Note on the Interdependency of Swelling Void Diameter and Void Number Density in Annealed AISI Type 304 Stainless Steel, WHAN-FR-15 (Oct 1970); PNL: T. T. Claudson, R. W. Barker, and R. L. Fish, The Effects of Fast Flux Irradiation on the Mechanical Properties and Dimensional Stability of Stainless Steel, Nucl. Appl. and Technol. 9, p. 10 (July 1970); Harkness: S. D. Harkness and C. Y. Li, A Model for Void Formation in Metals Irradiated in a Fast-neutron Environment, ANL-7588 (Aug 1969).

C. Engineering

1. Systems Engineering. B. C. Cerutti (02-068)

- a. Surveillance, Evaluation, and Studies of Systems (Last reported: ANL-7825, p. 1.34)

(1) Replacement of Control-rod Thimble (J. B. Waldo). During routine fuel handling for Run 49F, a subassembly could not be inserted into grid position 5E4. This position is between the No. 4 and 5 control-rod thimbles. Neither of these thimbles had ever been replaced. Several attempts to insert different subassemblies in position 5E4 were unsuccessful. The No. 4 thimble was then selected for replacement. The scalloped dummy subassemblies were installed in the surrounding positions, and the thimble was removed and transferred to the FEF without difficulty. A new thimble was installed, and the reactor was returned to operation.

Visual examination of the No. 4 thimble in the FEF air cell revealed that the hexagonal can of the thimble had increased in length sufficiently to project above the hexagonal cans of the surrounding subassemblies. Deformed areas, made by the core-holddown mechanism, were evident on the top edges of all six flats of the thimble. Rather bad score marks were also apparent on the flats of the core region, where irradiation swelling had occurred. An evaluation is being made to decide whether all original thimbles in the reactor should be replaced soon.

2. New Subassemblies and Experimental Support. E. Hutter (02-046)

- a. Experimental-irradiation Subassemblies (Last reported: ANL-7758, p. 34)

(1) Mark-J19A and Mark-J37A Irradiation Subassemblies (R. V. Batch and O. S. Seim). The Mark-J19A irradiation subassembly is an improved design of the Mark-J19 irradiation subassembly (see ANL-7618, p. 25). Design of the Mark J19A was initiated to simplify remote assembly and disassembly. The Mark J37A is a duplicate of the Mark J19A, except for the number and size of the test capsules. The Mark J19A uses 19 test capsules, each 40 in. long by 0.375 in. OD and wrapped with 0.030-in.-dia spiral spacer wire to give a pitch-to-diameter ratio of 1.08. The Mark J37A uses 37 test capsules, each 40 in. long by 0.250 in. OD and wrapped with 0.040-in.-dia spiral spacer wire to give a pitch-to-diameter ratio of 1.08.

Both subassemblies, shown in Fig. I.5, are vehicles for testing cladding materials at higher-than-normal reactor temperatures. An annular gas plenum allows higher element-bundle temperatures while flow orifices control the bypass flow to give the desired subassembly exit temperature after the capsule and bypass flows mix.

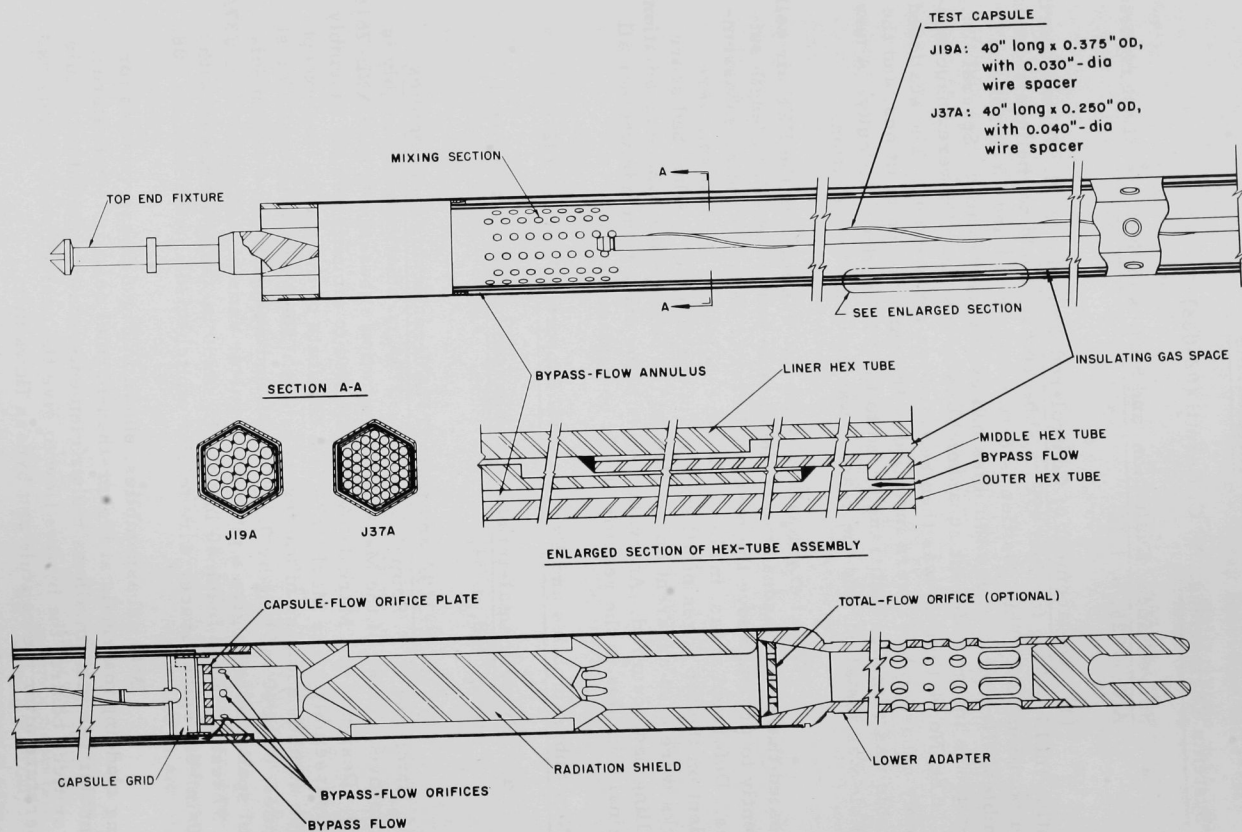


Fig. I.5. EBR-II Mark-J19A and Mark-J37A Irradiation Subassemblies. ANL Neg. No. 104-86 Rev. 1.

Only the top fixture and the lower adapter of the subassemblies are standard hardware items. Within the outer hexagonal tube is an inner hexagonal-tube assembly, a double-walled structure consisting of an inner hexagonal liner within a specially constructed hexagonal tube (called the middle hex tube in Fig. I.5). This construction provides a sealed annular space between the inner liner and lower portion of the middle hexagonal tube that extends from 2 in. above the reactor core to the grid. Argon gas trapped in this annulus when the subassembly is loaded into the reactor serves as insulation for the capsules. The walls of the inner liner and of the lower section of the middle hexagonal tube are stepped to provide a 0.016-in.-wide gas annulus throughout the length of the core and a 0.032-in.-wide annulus between the core and the grid.

The liner and the middle hexagonal tube are designed to expand and contract independently without exceeding the allowable stress.

Sodium coolant enters the lower adapter through the standard inlet holes in the adapter and passes up through the shield. At the top of the shield, orifices divide the flow into bypass flow and capsule flow. The bypass flow passes through six radial orifice holes in the shield. These holes are sized to provide a subassembly exit temperature about equal to that of the adjacent subassemblies when the bypass flow mixes with the hotter flow from the capsules. The bypass flow passes through the annulus between the outer hexagonal tube and the middle hexagonal tube and enters the mixing section of the subassembly, which is immediately above the upper ends of the test capsules.

The capsule flow passes through an orifice plate at the top of the radiation shield and enters the capsule bundle. The holes in the orifice plate are sized to provide the desired capsule temperature. After passing through the capsule bundle, the flow enters the mixing section, where it mixes with the cooler bypass flow.

Mixing is accomplished when the bypass flow leaves the annular passage through $96\frac{1}{8}$ -in.-dia holes and enters the mixing section. The holes are sized and positioned to create a turbulent, swirling action within the mixing section. Photographic studies were made of the mixing process during development of the Mark-C irradiation subassembly, which uses the same mixing arrangement. These studies indicate complete blending of the capsule and bypass flows before they reach the top end fixture of the subassembly.

Both the Mark J19A and the J37A were flow-tested in the pressurized-water test loop. To ensure accurate data, the loop was previously calibrated with a standard core subassembly used as a calibration reference. Table I.17 lists the standard values for each row. The first series of tests was made to determine the pressure drop across the radiation shield and lower adapter in each row position and at different flows.

For these tests, only the lower adapter, radiation shield, outer hexagonal tube, and top end fixture were used. Results for each data point were converted to sodium-flow values at 800°F. Figure I.6 shows the results of these tests.

TABLE I.17. Reference Flow-test Values for EBR-II Standard Subassembly

Reactor Row	Effective Pressure Drop, ^a psi	Flow of 800°F Sodium, gpm
1 and 2	38	140.5
3	39	123.3
4	34.5	93.7
5	34.0	78.0
6	40.8	31.0

^aWith depleted-uranium radial blanket in reactor.

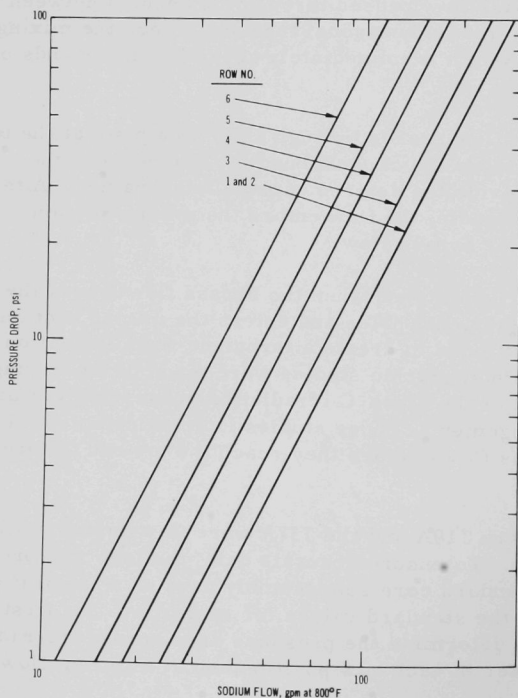


Fig. I.6

Pressure Drop vs Flow across Lower Adapter and Shield of Mark-J19A and Mark-J37A Subassemblies

A fully assembled subassembly was used in the second series of tests, but the bypass holes were eliminated from the radiation shield so all flow would go through the capsule channel. The pressure drop across the capsule-flow orifice plate was recorded at various flow rates for both the 19- and 37-capsule subassemblies. The size of the holes in the orifice plate was varied from $1/16$ to $9/32$ in. in $1/32$ -in. increments. Figure I.7 shows the pressure-drop versus flow characteristics of the capsule orifice plate and capsule bundle for the 19-capsule subassembly. Figure I.8 shows the corresponding characteristics for the 37-bundle subassembly.

In a third series of tests, a fully assembled subassembly was again used, but this time the orifice plate was left undrilled to allow only bypass flow. The size of the bypass orifice holes was varied from $1/16$ to $9/32$ in. in $1/32$ -in. increments. Figure I.9 shows the results of these tests.

Both the Mark J19A and the J37A provide many combinations of bypass and capsule flows, thereby allowing a wide range of experiments at elevated temperatures. The hole sizes for both the bypass- and the capsule-flow orifices that will produce the capsule flow necessary to satisfy a particular experiment can be readily determined.

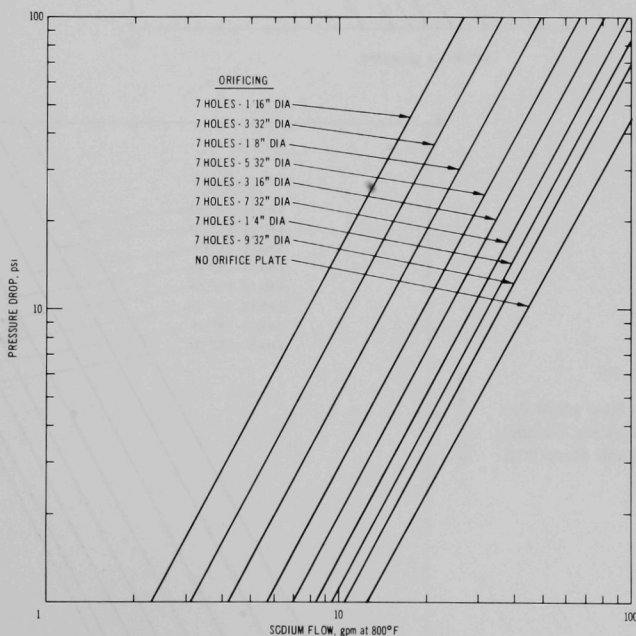


Fig. I.7. Pressure Drop vs Flow across Capsule-flow Orifice Plate and Capsule Bundle of Mark-J19A Subassembly

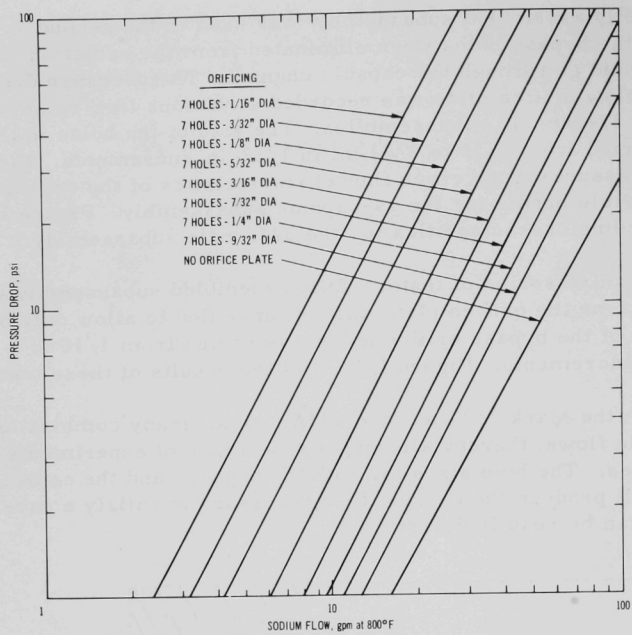
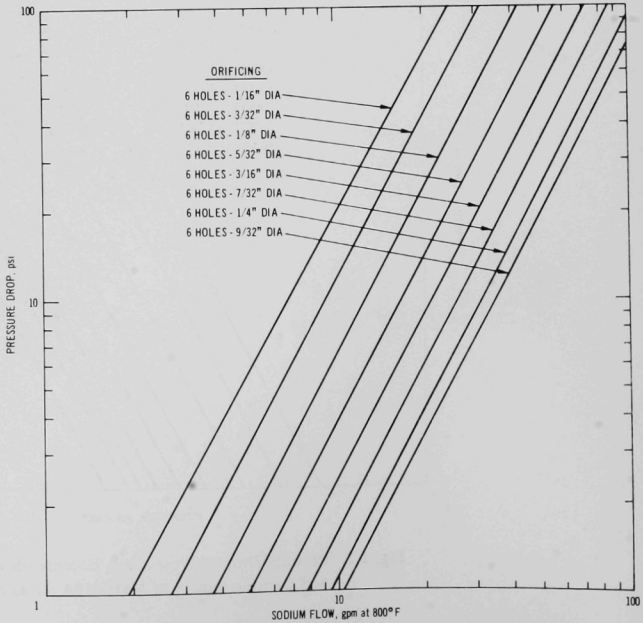


Fig. I.8
Pressure Drop vs Flow across
Capsule-flow Orifice Plate
and Capsule Bundle of
Mark-J37A Subassembly

Fig. I.9
Pressure Drop vs Flow across By-
pass Orifice Holes and Channel
of Mark-J19A and Mark-J37A
Subassemblies



PUBLICATIONS

Eddy Current Inspection Technique for Detection of Cracks in Irradiated Fuel Element Cladding

W. N. Beck

Mater. Eval. 29, 25A-26A (July 1971) Note

Effect of Boron on the Ductility and Strength of Inconel 600 and Types 304 and 316 Stainless Steel at Hot Metalworking Temperatures

A. K. Chakraborty, C. K. H. Du Bose,* and W. R. Martin*

ORNL-TM-3316 (May 1971)

*Oak Ridge National Laboratory.

II. LMFBR DESIGN SUPPORT

A. Heat Transfer and Fluid Flow. R. P. Stein (02-097)

Analytical and experimental investigations of liquid-metal heat transfer and fluid flow in components and systems are conducted to provide information of immediate interest to the FFTF and LMFBR Programs. Fundamental studies in heat transfer and fluid flow also are conducted to improve current, or to devise new, engineering prediction methods essential to the advancement of reactor technology in general.

1. LMFBR Flow Stability Studies. R. R. Rohde

This activity covers (1) the acquisition and analysis of experimental data on the vaporization and superheating of sodium in operating ranges (pressures, flow rates, temperatures, and equivalent diameters) and flow circuits of interest to the LMFBR Program; and (2) the determination, by both experiment and analysis, of two-phase flow phenomena related to flow stability. An LMFBR Simulation Heat Transfer Loop is being constructed for the experiments.

a. Preparation of Apparatus (Last reported: ANL-7833, p. 2.2)

The status of construction of the LMFBR Simulation Heat Transfer Loop is as follows: The 15 temperature controllers for the trace heating system were installed in the controller panel. Louvers for the loop-enclosure cooling system were installed, and the air operators used to open or close the louvers were checked for proper performance. Other installations completed included thermocouples for monitoring air temperature from the heat exchanger, and protective enclosures which allow ventilation around electrical equipment such as autotransformers for loop equipment and filament transformers for the electron-bombardment heaters.

Supporting analytical work completed included: (1) calculation of final pressure-versus-drop flow characteristic curves for the unheated portion of the test section; and (2) calculation of the possibility of subcooled boiling in the heated section. Data from the latter calculation are being analyzed.

2. Nonboiling Transient Heat Transfer. R. P. Stein

The objective of this activity is to develop improved engineering prediction methods to account for nonboiling forced-convection heat transfer in ducts during transients.

a. Analysis of Heat-flux Transients (Last reported: ANL-7833, p. 2.2)

A careful review was made of previously unsuccessful attempts to apply the new prediction methods to a sample case in which heat generation

within the walls is specified. One significant numerical error was discovered and corrected. Several alternate formulations to account for the inlet condition were considered. However, as before, attempts to use the computer program that is based on the new prediction methods resulted in numerical instabilities.

Additional analysis leads to the consensus that the difficulty lies within the numerical methods used in the computer program.

3. Liquid-metal Heat Transfer in Pin Bundles. T. Ginsberg

The objectives of this activity are to: (1) develop and evaluate analytical models for predicting steady-state temperature distributions in LMFBR fuel assemblies, and (2) develop empirical data and correlations for use in the analytical models. The latter objective includes development of a model that describes the interchannel-mixing mechanism in fuel assemblies containing helical-wire-wrapped fuel elements.

a. Analytical Investigations (Last reported: ANL-7776, p. 83)

A modified version of the swirl-flow model for fuel assemblies containing helical spacers has been applied to the EBR-II. This evaluation is being carried out with the cooperation of T. Bump (MSD) and AUA Summer Engineering Practice School participants.

4. Electron Bombardment Heater (EBH) Development. R. D. Carlson

Electron-bombardment (EB) heaters are being developed to supply heat fluxes greater than 1.5×10^6 Btu/(hr)(ft²) to liquid metals. These heaters will be used as backups to resistance-type heaters in various heat-transfer and reactor-safety experiments pertinent to the LMFBR Program. Current effort is directed toward EB pin-type heater test sections containing simulated LMFBR fuel pins for use in these experiments. Such heaters (1/4-in. OD x 24 in. long) have supplied heat fluxes up to 2.3×10^6 Btu/(hr)(ft²) to water.

a. MHD Characteristics of EB-versus-Resistance-type Heaters (Last reported: ANL-7825, p. 2.5, under Preparation of Single Pin)

A computer program has been written for calculating the magnetohydrodynamic characteristics of various-sized bundles of electrically heated pins (up to 37 pins) at heat fluxes up to 10^6 Btu/(hr)(ft²).

5. Heat Transfer in Liquid-metal-heated Steam Generators. D. M. France (Last reported: ANL-7833, p. 2.3)

A detailed description of the operational characteristics of the test loop was prepared and reviewed at a design review meeting held on

June 28, 1971. The loop is being readied for experiments on a concentric, double-pipe, mercury-boiling Freon-heat-exchanger test section at conditions approximating LMFBF sodium-water steam generators. As a result of the design review, several additions will be made to the loop, predominantly to the mercury flow circuit. The Freon flow circuit is being leak-tested.

The computer code for predicting test conditions was successfully executed. Results indicate that two phases of testing probably will be necessary. One phase will focus on measuring the departure from nucleate boiling condition (DNB) and local boiling heat transfer. The other phase will attempt to reproduce the ALCO-BLH steam generator test series at LMEC, during which anomalous "flips" were observed.

B. Engineering Mechanics. G. S. Rosenberg (02-099)

Stress-analysis methods based on various continuum theories are developed to resolve reactor design problems that are not amenable to conventional engineering approximations or direct numerical computations employing general-purpose computer programs. Studies of structure-fluid interaction dynamics also are conducted to develop new methods of analysis and testing that can be used by designers to minimize the potential of detrimental flow-induced vibration of reactor components.

1. Structure-fluid Dynamics. M. W. Wambsganss

- a. Parallel Flow-induced Vibration. S. S. Chen and M. W. Wambsganss (Last reported: ANL-7833, p. 2.4)

For purposes of illustration, the results of the analysis described in ANL-7833 were used to study the dynamic characteristics of tubes in the ATR primary heat exchanger to determine the stop and propagation bands for moment waves. A simplified model of the tube along with pertinent data* are shown in Fig. II.1.

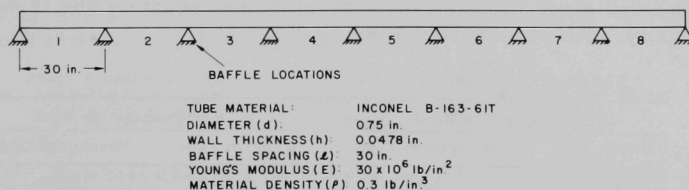


Fig. II.1. Simplified Model of ATR Primary Heat Exchanger Tube

*H. A. Nelms and C. L. Segaser, Survey of Nuclear Reactor System Primary Circuit Heat Exchangers, ORNL-4399 (Apr 1969).

Consider the system as an infinite, periodically supported tube. If the bending moment at the n th support is $M_n e^{i\omega t}$, then the bending moment at the j th support will be

$$M_j = M_n \exp[i\omega t - (j - n) \mu], \quad (1)$$

where μ is the propagation constant and is a function of flow velocity u , fluid pressure ν , axial force Γ , mass ratio β , and frequency Ω . The propagation constants for an ATR tube are shown in Fig. II.2, where $\Gamma = 0$ and 4.0, $u = 0$, $\nu = 0$, $\beta = 0.6852$, and $\Omega = \omega/39.58$. In the propagation band, the bending wave will propagate through the structure; in the stop band, the bending wave is attenuated as it propagates.

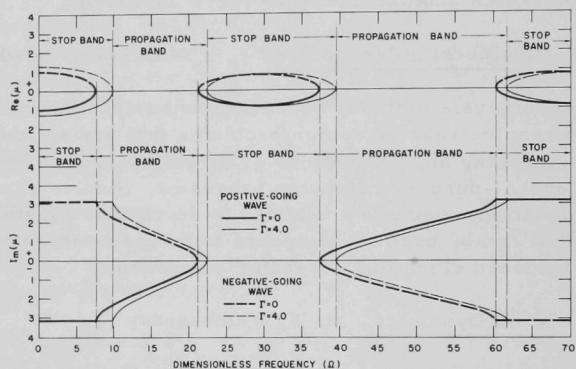


Fig. II.2. Flexural Wave Propagation in Periodically Supported Heat-exchanger Tube of ATR Design

Next, we calculate the natural frequency of the eight-span tube as shown in Fig. II.1. Two cases are considered: (a) uniform continuous tube (i.e., the system parameters are the same in every span); and (b) non-uniform continuous tube (i.e., the dimensionless axial force is taken to be 4.0 in the fourth and fifth spans and zero in the others). The frequency equation is obtained by using the three-moment equation and is solved numerically. The results are given in Table II.1.

TABLE II.1. Dimensionless Natural Frequencies of Continuous Tubes

First Propagation Band		Second Propagation Band	
Uniform Tube	Nonuniform Tube	Uniform Tube	Nonuniform Tube
9.86	9.00	39.48	38.81
10.30	10.23	40.41	40.34
11.51	10.94	42.84	42.16
13.28	12.94	46.17	45.81
15.41	15.09	49.96	49.57
17.71	17.24	53.91	53.34
19.91	19.76	57.63	57.46
21.66	21.19	60.53	59.87

The corresponding mode shapes of the first four modes are shown in Fig. II.3. Note that there are eight natural frequencies in each propagation band. In general, for a continuous tube with n spans, there are n natural frequencies in each propagation band. No natural frequencies exist in the stop band for a uniform tube. However, certain frequencies do exist in the stop band for a nonuniform tube; in this case, the stop band of one portion of the structure may be the propagation band of another portion of the structure.

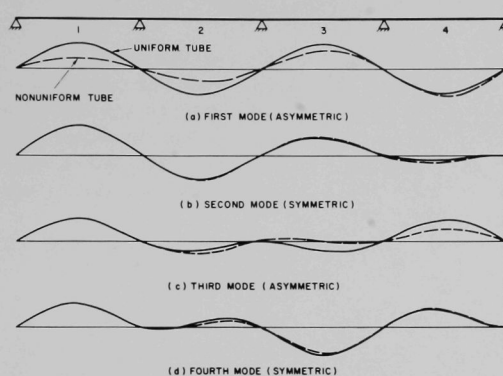


Fig. II.3. Mode Shapes for Uniform and Nonuniform Continuous Tubes

For example, for $7.51 < \Omega < 9.91$ in Fig. II.2, the flexural wave propagates freely for $\Gamma = 4.0$, but is attenuated for $\Gamma = 0$.

If natural frequencies exist in this range, the shape of the modes will differ markedly from that for a uniform tube; these modes are called energy-trapping modes. There are two energy-trapping modes for the nonuniform tube given in Table II.1: $\Omega = 9.00$ and $\Omega = 38.81$. The mode shape for $\Omega = 9.00$ is shown in Fig. II.3. Here, the absolute amplitude of the uniform tube is the same in each span, while for the nonuniform tube, the amplitudes in the fourth and fifth spans are much larger than the others; a large portion of the energy is confined in the center two spans. Thus if the excitations approach this particular frequency, the vibration energy is trapped in the center portion of the tube.

In summary, identification of the propagation and stop bands associated with an infinite, periodically supported tube is useful in determining: (1) the frequency bands in which the natural frequencies of a finite tube will be found; and (2) for nonuniform tubes, which frequencies are associated with an "energy-trapping" mode.

- b. Crossflow-induced Vibrations of Cylinders. H. Halle and P. L. Zaleski (Last reported: ANL-7833, p. 2.6)

The test chamber to be used for crossflow-induced experiments in the Structural Dynamics Test Loop has been fabricated and hydrostatically tested. Design of the chamber support structure is 80% complete.

III. INSTRUMENTATION AND CONTROL

A. Instrumentation Development for Instrumented Subassembly. T. P. Mulcahey (02-024)

Instruments for in-core measurement of flow, fuel and coolant temperatures, and fuel-pin pressure are being developed consistent with requirements defined by the EBR-II Instrumented Subassembly test program. Development encompasses instrument design, performance analysis, fabrication, and tests leading to specifications and quality-assurance procedures for procurement from commercial vendors.

1. Instrumented Subassembly (ISA) Flowmeters. G. A. Forster (Last reported: ANL-7758, p. 26)

One of the four Mark-III flowmeters procured from General Electric Company has been installed in the Sodium Flowmeter Calibration Facility. The flowmeter will be calibrated at sodium temperatures up to 800°F. It will then be removed, cleaned, and stored for use in future EBR-II instrumented subassemblies.

2. Fuel-pin and Coolant Thermocouples. A. E. Knox (Last reported: ANL-7833, p. 3.1)

Capsules No. 2 and 7, which were irradiated in EBR-II Test ISA XX01, were disassembled in high-level caves and the fuel elements removed with the sheathed lead wires of the thermocouples intact. The sheaths were partially stripped back to expose the alumina insulation, and the Type 308L stainless steel and Alumel lead wires. In each instance, the alumina had changed from a white powder to a white coherent mass. This mass was slightly flexible, but broke if bent sufficiently. The lead wires were strong and flexible. Measured wire-to-wire and wire-to-sheath resistances were less than 0.2 ohm.

The stripping operations and resistance measurements were repeated several times on each thermocouple and with the same results. Apparently, the "alumina" mass is electrically conductive; samples have been prepared for chemical analysis to determine the cause of the low resistance. There was no evidence of shorting while the ISA was in the EBR-II.

Photographs of metallographic sections of Capsule No. 1 taken in the region of FCTC 1 were received from EBR-II, Idaho, and are being examined by the staff of Engineering and Technology Division.

Postirradiation examination of the EBR-II Test ISA XX02 inlet thermocouple is in progress.

B. FFTF Instrumentation Development.
R. A. Jaross (02-025)

Prototypes of permanent-magnet, eddy-current, and magnetometer probe-type flowsensors are being designed, fabricated, and flowtested to establish detailed specifications and design for the FFTF permanent-magnet probe-type flowsensor, and to provide technical guidance to ensure competence in commercial fabrication of probe-type flowsensors. Supporting tests are conducted to determine long-term thermal effects on permanent-magnet materials of interest, and to study the effects of simulated fission-gas release on flowsensor response.

1. Magnetometer Probe-type Flowsensors. D. E. Wiegand (Last reported: ANL-7825, p. 3.4)

In the gradiometer version of the flowsensor, two opposed fluxgate elements are symmetrically mounted coaxially with a single field magnet. A computer program (GRAFLOM), based on an analysis of this configuration, shows that signal levels and required mechanical and magnetic precision are very nearly the same as in the magnetometer configuration (two magnets, one fluxgate).

Tests on a mockup of the gradiometer configuration have demonstrated its feasibility.

The gradiometer is insensitive to magnetic disturbances which have space uniformity, even though they may be time-varying. Which configuration is the better depends on the ambient magnetic noise conditions in the reactor. Present plans are to continue with the magnetometer version. However, since only a variation in positioning of the same basic elements is involved, a switch to the gradiometer concept could be made at any time.

The fluxgate in Magnetometer Flowsensor No. 2 (MFS-2) required the use of an external attenuator to prevent overloading of the lock-in amplifier equipment. More recent fluxgate designs have output signals at reduced levels, but much lower excitation requirements. For example, in one of these units, an optimum excitation current of 0.38 A at 10 kHz was supplied through 35 ft of Chromel-Alumel thermocouple wire in a 1/8-in.-OD sheath. The voltage at the sending end was 23 V. The voltage and power requirements appear satisfactory.

The test equipment has been moved to a trailer adjacent to the Annular Linear Induction Pump (ALIP) Test Facility. The new location will facilitate flow tests in the thimble of the ALIP as well as out-of-sodium tests.

To provide increased reliability in the calibration of fluxgates and electromagnets to be used in the flowsensor, a Helmholtz coil system has

been installed. Preliminary measurements with this system are in close agreement with previous measurements using a solenoid.

Cores for electromagnets and fluxgates have been fabricated from Hiperco 27 (cobalt-iron material), which has a high Curie temperature. These cores were annealed in argon to remove the effects of cold work. The postanneal blue oxide coating does not appear to have a serious effect on the performance in our application. If later tests show adverse effects, the parts will be re-annealed in hydrogen, as recommended by the supplier.

A fluxgate consisting of a Hiperco strip in a coil wound with high-temperature ceramic-coated gold wire required a lower optimum excitation current and evidenced lower residual signal components than units with iron wire cores tested previously. The lower residuals reflect an increased sensitivity or a simplification in the signal-processing equipment, and the lower excitation requirement simplifies the problem of transmitting primary power over a long cable.

Two electromagnets fabricated with Hiperco cores and high-temperature coils showed lower magnetic field strengths than anticipated. However, the signal levels should still be adequate, particularly in view of the improved sensitivity of the Hiperco fluxgates.

C. Neutron-detector Channel Development. G. F. Popper (02-138)

Development under contract with industrial vendors is focused on complete neutron-detection channels, including cabling and circuitry to transmit, process, and display information from high- and low-temperature ionization chambers and self-powered detectors in out-of-core and in-core regions of LMFBRs. Advanced circuitry for intermediate- and wide-range applications, and high-temperature neutron detectors are procured commercially; vendor tests are administered; and parameter determination and operational tests are performed in ANL and EBR-II nuclear-instrument test facilities.

1. Intermediate- and Wide-range Systems. G. F. Popper (Last reported: ANL-7825, p. 3.5)

A preliminary draft of RDT Standard C15-8: Direct Current Power Range Channel was prepared and issued to selected reviewers for comment. Preparation of Draft RDT Standards C15-10: Logarithmic Count Rate Source Range Channel, and C15-6: Logarithmic MSV Intermediate Range Channel is in progress.

An unnumbered Draft RDT Standard: General Nuclear Instrumentation was reviewed and comments forwarded to WARD.

2. High-temperature Neutron-detector Technology. G. F. Popper, A. Hirsch, and G. E. Yingling (Last reported: ANL-7825, p. 3.5, under Out-of-core Detectors and Cables)

A Draft RDT Standard C15-7: Fixed, Electrical Gamma Compensated Ionization Chamber Assembly was completed and forwarded to RDT for review and approval.

The failure-mode analysis of Reuter-Stokes (R-S) RSN-286 M401 was initiated by the vendor approximately two months after the request was made. A failure report supplement covering nondestructive tests, including radiographs, performed by R-S was submitted to ANL. Both R-S and ANL conclude that no obvious defects could be detected from the test results.

The destructive tests were witnessed by ANL representatives. During disassembly of the detector, it was observed that a spring washer was missing from the bottom end of the detector. The reason for this omission is not known.

The detector was not disassembled with the necessary precision to determine, with any degree of certainty, the cause of intermittent low resistance observed during vendor testing. However, there was visible evidence of arcing on the electrodes and rough electrode coating. This lends support to the theory that a dendrite growth of the coating caused the low resistance which could be cleared with a capacitator discharge.

The cable end of the detector was clean and in good condition, but there was some evidence of foreign material on the underside of the bottom support insulators. Improper cleaning is the probable cause.

The evacuation tube, which is specified to be made of pure nickel, broke off while the detector was being radiographed. The tube had become extremely brittle and crystalline. Reuter-Stokes will determine the composition of the tube by wet chemical analysis. The results of the analysis, along with recommendations for rebuilding or redesigning the detector, will be included in a complete failure report supplement to be submitted to ANL.

The second redesigned Westinghouse WX-31384 fission counter was delivered to ANL.

3. High-temperature Neutron-detector Cable Technology. A. Hirsch and A. E. Knox (Last reported: ANL-7825, p. 3.5, under Out-of-core Detectors and Cables)

Oven testing of Reuter-Stokes RSN-202-BG and Westinghouse WX-31353-25 cable assemblies to 850°F, consistent with RDT Standard F3-39, has been completed. Technical notes describing the results of these tests are being prepared.

A length of high-temperature mineral-insulated cable, produced by Sodern (France) has been received from ORNL for testing. The cable does not have high-temperature end seals or connectors. The ends of the cable are only sealed with heat-shrink tubing.

Radiographs were made of the R-S, Westinghouse, and Sodern cables, and the Westinghouse end seals and connectors. Although specifications indicate coaxial cable, the Westinghouse cable was actually triaxial, with the inner sheath floating. Westinghouse has been requested to document, from their material records, the type of cable delivered to ANL.

4. NITF Test Program. V. J. Elsbergas (Not previously reported)

A request for approval-in-principle for testing detectors in the EBR-II Nuclear Instrument Test Facilities was approved by RDT. Following approval by EBR-II Project Staff, the WX-31384 and RSN-286 M402 detectors were installed in the EBR-II O-1 thimble prior to Run No. 50 and calibrations started.

Drawings were prepared and fabrication started on a holder for the WX-30950 Compensated Ionization Chamber to be installed in the EBR-II J-2 thimble.

D. Advanced Technology Instrument Development. T. P. Mulcahey (02-096)

New and unique instrumentation is being developed to diagnose performance and detect abnormalities in the LMFBR cores. Included are sensors and techniques for acoustical detection of sodium-coolant boiling, monitoring of flow-rate-related phenomena that could detect imbalances between cooling and power, and the measurement of vibrations that might disturb overall reactor stability.

1. Acoustic Surveillance. T. T. Anderson

a. Development of High-temperature Detector. A. P. Gavin (Last reported: ANL-7825, p. 3.8)

Two sensors of the HT-6 series (HT-6-2 and HT-6-3) were fabricated and then exposed for more than 14 days to temperatures in excess of 1200°F in the Furnace Calibration Facility; included were several cycles to room temperature. Because resistance and charge response cannot be measured simultaneously on one unit, the resistance of one unit and the response of the other to a constant 350-Hz excitation are monitored and recorded together with shaker acceleration level and temperature on a four-pen strip-chart recorder.

Plots of periodic response versus frequency at 250-500 Hz, with a standard acceleration level on the piston drive, showed very little change in response with exposure to 1200°F for two weeks. Resistance of a given unit at a given temperature also was stable when the internal oxygen pressure was maintained between 200 and 400 mm Hg by means of the vent tube.

The vent tube of HT-6-3 was then sealed with an internal oxygen pressure of 200 mm Hg and the unit returned to test at 1210°F. For 16 hr, the response, as measured by a charge amplifier, remained constant, then increased rapidly to a meaningless off-scale value, indicating that the resistance had dropped below the range of the amplifier. After the vent tube was reopened, and the unit evacuated and refilled with oxygen to the same pressure, the resistance again increased rapidly, but after 24 hr the value was the same as before the tube was sealed.

Subsequently, the vent tube of HT-6-2 was sealed with an internal oxygen pressure of 400 mm Hg, and tested at 1210°F. In 8 hr, the resistance dropped to less than 5000 ohms, and continued to drop to a minimum of 45 ohms in 20 hr. After the vent tube was opened and the unit evacuated and refilled with oxygen to the same pressure, the resistance increased to 10,000 ohms in less than 10 min, and to 18,000 ohms in 24 hr.

Future tests will explore the internal oxygen pressure required for continuous high-temperature operation.

X-ray diffraction studies of 12 recently purchased piezoelectric crystals indicate that variation between crystals is within specified limits, but do not provide a check on crystal orientation.

- b. Development of Acoustic Waveguides. T. T. Anderson (Last reported: ANL-7798, p. 52)

An acoustic-waveguide test assembly has been constructed to simulate both the FFTF instrument guide tube and an acoustic-vibration-transmission member of the EBR-II Test ISA XX03. Briefly, the assembly consists of a Type 304 stainless steel tube (20 ft long, $1\frac{1}{4}$ in. OD, $1\frac{1}{8}$ in. wall), which is open at one end. This end is immersed (vertically) 6 in. into a water-filled tank. The upper end is terminated by a 645-g steel mass, to which is attached an accelerometer.

Vibration response at the accelerometer was determined for sound waves impinging tangentially on the immersed portion of the tube. Acceleration response was measured and checked: (1) by a three-parameter analysis of the acceleration amplitude spectrum (25-100 kHz) taken for 0.1-msec increments of time delay after a 0.2-msec duration of sine waves; (2) by oscilloscope traces of the acceleration signal for the train of sine-wave acoustic pressure; and (3) by rms spectrum to reverberant sound pressure (1-100 kHz).

The results were consistent in showing the acceleration response to contain resonances from 34 to 91 kHz (see Table III.1), and to have much lower response at other frequencies. First and second radial modes of the water inside the tube were excited at the 34.2- and 78-kHz resonances, respectively, and were transmitted along the tube at the longitudinal velocity. Dispersive (shear) waves can be identified by the lower transmission velocity (~ 2800 m/sec). Transfer admittance (i.e., ratio of upper termination velocity to the incident pressure of 5×10^{-6} cm²-sec/g for the major resonances) was an order of magnitude higher than an estimate based on transmission in terms of characteristic impedances of water and steel.

TABLE III.1. Summary of Tests on Tubular Waveguide

Resonance Frequency, kHz	First Time of Arrival, msec	Equivalent Velocity, m/sec	Transfer Admittance, 10^{-6} cm ² -sec/g
34.2	1.2	5100	4.6
44	-	-	3.5
49	2.2	2800	4.9
54	-	-	2.0
57	-	-	2.5
62.5	2.3	2700	3.3
70.6	1.5	4100	2.9
77.5	1.3	4700	4.8
91	-	-	1.2

2. Vibration Sensor. T. P. Mulcahey

a. Out-of-pile Tests of Sodium-immersible Commercial Transducers. G. A. Forster (Last reported: ANL-7825, p. 3.9)

Disassembly and inspection of the accelerometer that failed during initial heat-up of the CCTL revealed that excess lead length inside the sensor apparently caused an initial short where the center lead of the triaxial cable touched the sensor housing. During the ensuing 6000-hr flow-test of the FFTF Mark-II fuel assembly, a crystalline deposit (~ 0.005 in. thick) had built up on the lead wires, causing further shorting. This information has been forwarded to the vendor (Gulton) to guide design changes that may prevent similar failures in the future.

Triaxial cables were sent to Gulton for use on accelerometers being procured for flowtesting the FFTF Mark-IIA fuel assembly. This was

a condition on which the June 30 delivery date was based. In turn, Gulton will send the cables they would have used.

E. Plant Dynamics and Control Analysis. W. C. Lipinski, RAS
(02-528; last reported: ANL-7833, p. 3.5)

1. Analysis of Overall Control-system Performance during Mild Transients to Identify and Resolve Control Problems (Not previously reported)

A recent comparison of overall power-plant costs in LMFBRs using various steam-generator concepts (L. A. Sturiale, Steam Generator Concept Selection Study, WARD-4210T2-1, Feb 1971) has indicated economic advantages of once-through steam generators with separate shells for evaporation and superheating. Based on these results, the complete-plant hybrid simulation being used in the ANL study of LMFBR dynamics and control was updated to include a simulation of a separate-shell steam generator. The previous simulation was based on a single-shell model.

Because some superheating occurs in the evaporator module, the basic model for its simulation is identical to that of the single-shell steam generator, except for changes in parameter values. The model for the superheater module is the same as for the reheater previously included in the plant simulation.

PUBLICATION

Eddy-Current Probe-Type Sodium Flowsensor for FFTF Reactor Fuel Channel Flow Monitoring

J. Brewer, R. A. Jaross, and R. L. Brown*

IEEE Trans. Nucl. Sci. NS-18(1), Part 1, 372-377 (Feb 1971)

*WADCO Corp.

IV. SODIUM TECHNOLOGY

A. Sodium Impurity Analysis and Control
(02-593)1. Studies of the Sodium-Oxygen-Hydrogen System. F. A. Cafasso and
K. M. Myles (Last reported: ANL-7798, p. 61)

The objective of this work is an understanding of the behavior of oxygen- and hydrogen-bearing species in liquid sodium.

Elucidation of the phase relationships in the Na-Na₂O-NaOH-NaH system is part of this program. This system may be divided by either of two joins, namely, Na-NaOH or Na₂O-NaH. Two preliminary working diagrams--one based on the Na-NaOH join (the Na-NaOH working diagram) and the other based on the Na₂O-NaH join (the Na₂O-NaH working diagram)--were presented previously.* These were composite diagrams of the room-temperature isothermal section and superimposed liquidus valleys. The essential features of the diagrams and the assumptions made in generating them were also described.

Recent X-ray diffraction results (ANL-7798) provided a basis for the selection of the Na₂O-NaH working diagram as the one to be used to guide further work. Accordingly, this diagram has been updated to make it consistent with our current knowledge about the Na-O-H system. The updated versions are shown in Figs. IV.1 and IV.2.

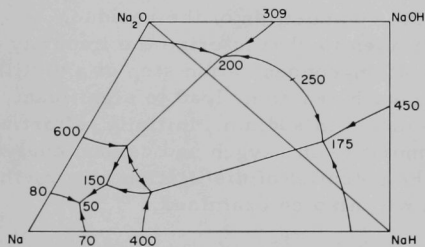


Fig. IV.1

The Liquidus Valleys and the Room-temperature Isothermal Section of the Na-Na₂O-NaOH-NaH System Based on the Reaction $\text{Na}(\ell) + \text{NaOH}(\text{s}) = \text{Na}_2\text{O}(\text{s}) + \text{NaH}(\text{s})$ (temperatures in °C)

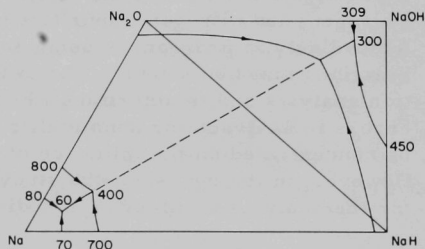


Fig. IV.2

The Liquidus Valleys and the Room-temperature Isothermal Section of the Na-Na₂O-NaOH-NaH System Based on the Reaction $\text{Na}(\ell) + \text{NaOH}(\ell) = \text{Na}_2\text{O}(\text{s}) + \text{NaH}(\text{s})$ (temperatures in °C)

The important difference between the two diagrams is that in Fig. IV.1 the reaction is assumed to be $\text{Na}(\ell) + \text{NaOH}(\text{s}) = \text{Na}_2\text{O}(\text{s}) + \text{NaH}(\text{s})$, whereas

*Sodium Technology Quarterly Report, April, May, June 1970, ANL/ST-3, pp. 4-4 to 4-13; Figs. 4-2 and 4-5 (Sept 1970).

in Fig. IV.2, the assumed reaction is $\text{Na}(\ell) + \text{NaOH}(\ell) \rightleftharpoons \text{Na}_2\text{O}(\text{s}) + \text{NaH}(\text{s})$. The temperatures given in the figures are only reasonable estimates of the, as yet unknown, actual temperatures. Present work is addressed to determining which of the two diagrams is correct; this information will aid in the prediction of reactions occurring in sodium-oxygen-hydrogen systems.

2. Vacuum Distillation as an Analytical Method for Impurities in Sodium.

F. A. Cafasso and R. A. Blomquist (Not previously reported)

The work of Walker *et al.**,** has demonstrated that vacuum distillation is a useful method for determining oxygen in sodium and that it has potential for determining carbon in sodium. In the analysis for oxygen, the work of Walker *et al.** has shown that, provided the oxygen exists in sodium as Na_2O or Na_2CO_3 , it may be determined indirectly by this method; however, the possibility has not been explored that the presence of other impurities, especially those known to exist in the sodium (e.g., Na_2C_2), might introduce errors in the analysis. In the analysis for carbon, experiments have shown that carbon in the form of either carbonate† or elemental carbon* is not lost (due to degradation of the carbonate or formation of carbon monoxide via the reaction of elemental carbon with sodium oxide) during distillation at 350°C. Tests have not been done to demonstrate that similar results are obtainable, regardless of the form of the carbon or the type and concentration of other impurities in the sodium.

Clearly, to exploit the full potential of this method for oxygen and carbon analyses and to place the method on a firm and fully tested basis, experiments are needed that examine the effects of added carbon, oxygen, hydrogen, and nitrogen impurities on the composition of the residue. Accordingly, a program is being undertaken to characterize the impurity reactions that may occur in the evaporation-concentration step of a distillation analysis and to determine whether such reactions lead to significant errors in analyses for nonmetallic elements in sodium. Initially, effort will be concentrated on the influence of impurities in oxygen and carbon analyses. However, in the course of the study, the potential of distillation as a method for the analysis of nitrogen in sodium will also be examined.

The requisite tests will be done by adding measured quantities of carbon-, oxygen-, hydrogen-, and nitrogen-bearing impurities, singly and in combination, to 1 kg of sodium. The mixture will then be heated inductively to distill away the sodium, and the residue and off-gases will be collected and analyzed by appropriate physical methods. A 1-kg still†† has been constructed for this study and is currently being assembled. Experimentation will begin as soon as optimum operating conditions of the still have been established.

*J. J. Walker, E. D. France, and W. T. Edwards, *Analyst* **90**, 727 (1965).

J. J. Walker and E. D. France, *Analyst* **90, 228 (1965).

†V. M. Sinclair, J. L. Dummond, and A. W. Smith, TRG-Report-1185(D) (1965).

††C. C. Miles of EBR-II, Idaho, provided the design of the still.

B. Nonmetallic Impurity Interactions in Sodium-Metal Systems (02-137)

1. Development of Equilibration Methods for Determining the Activity of Nonmetallic Impurities in Sodium. T. F. Kassner and D. L. Smith (Last reported: ANL-7798, p. 59)

The purpose of this work is to develop methods for accurately measuring the activities of nonmetallic elements (e.g., O, C, N, and H) in sodium at the low concentrations of interest for LMFBR applications.

a. Development of the Vanadium-wire Equilibration Method for Determining Oxygen Activity in Sodium

A procedure has been developed* for determining the oxygen activity in liquid sodium by equilibrating vanadium wires in sodium, measuring the oxygen content of the wires, and correlating the results with previously obtained data** for the distribution coefficients of oxygen between sodium and vanadium at 600, 650, 700, and 750°C. This method of analysis can be used at any temperature within this range or 50°C on either side by interpolation or extrapolation of the data. Equilibration of 0.25-mm-dia wire for 4 hr at 750°C is appropriate for LMFBR applications, and these conditions have been recommended as a standard to facilitate and improve comparison of interlaboratory analyses. Additional distribution-coefficient measurements have been made under these conditions to enhance the reliability of the values and to establish the precision of the method. The results are plotted in Fig. IV.3. The oxygen concentrations in the sodium were determined from solubility data† at the cold-trap temperature, which was carefully controlled in these experiments. The oxygen analyses of the vanadium wires were obtained by an inert-gas fusion technique,†† Analyses of wires equilibrated simultaneously generally agreed within $\pm 2\%$.

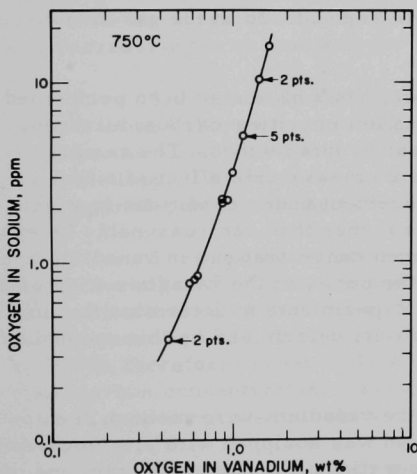


Fig. IV.3. Equilibrium Distribution of Oxygen between Vanadium and Sodium at 750°C. Neg. No. MSD-54652.

*D. L. Smith, Nucl. Technol. 11(1), 115-119 (1971).

**D. L. Smith, Met. Trans. 2(2), 579-583 (1971).

†D. L. Smith and T. F. Kassner, Corrosion by Liquid Metals, J. E. Draley and J. R. Weeks, eds., pp. 137-149, Plenum Press (1970).

††B. D. Holt and H. T. Goodspeed, Anal. Chem. 35, 1510-1513 (1963).

Agreement of the analyses was also good after the oxygen level was changed and then returned to the previous level.

The oxygen concentrations in vanadium at 750°C reported previously* were somewhat lower (for example, 10% at 1.0 wt % oxygen in vanadium) than results obtained in the recent series of tests. This difference is attributed primarily to difficulties in determining the oxygen concentration in sodium at the lower levels, where vacuum-distillation analyses were of limited accuracy. A portion of the original data is now believed to have been obtained under conditions in which the cold trap was slightly depleted of oxygen; this resulted in somewhat high values for the distribution coefficients. In addition, analytical problems associated with the gas-fusion apparatus occasionally resulted in low values for the oxygen content of the vanadium wires. These analytical problems had the effect of obscuring the slight depletion of oxygen in the cold trap and incomplete reequilibration of the loop after the temperature or oxygen concentration was changed. The small discrepancies in the distribution-coefficient data have now been resolved, and the data presented in Fig. IV.3 are considered to be more reliable than the previous values. These data represent three series of tests conducted by cycling the oxygen level in sodium several times from lower to higher values to confirm the reliability of the results. Control samples indicated that no problems were encountered in the gas-fusion analyses of these vanadium wires.

At the request of RDT, experiments have also been performed to investigate the effects of the nonmetallic impurities carbon, nitrogen, and hydrogen on the oxygen measurement by this method. The results, reported elsewhere,** indicate there is no measurable effect of either carbon or nitrogen on the oxygen measurement under conditions in which (1) carbon concentrations in sodium are higher than can reasonably be expected in reactor systems and (2) nitrogen concentrations in vanadium are in a range (i.e., <1000 ppm) typical of the purity of the vanadium wire used in the oxygen-activity measurements. Experiments to determine the effect of hydrogen in sodium on the oxygen activity determined by this method are in progress.

During the development of the vanadium-wire method, the sodium loop in which the data were obtained was equipped with electrochemical oxygen meters as a check on system operation. The emf data from one of these (a United Nuclear Corporation meter having a Cu, Cu₂O reference electrode and a ThO₂-15 wt % Y₂O₃ electrolyte) have been correlated with vanadium-wire results for the oxygen content of the sodium. The oxygen concentrations were determined using the revised distribution-coefficient data described above. The cell was operated at 352°C (625°K), and the

*D. L. Smith, Met. Trans. 2(2), 579-583 (1971).

**Sodium Technology Quarterly Report, January-March 1971, ANL-7817 (in press).

vanadium wires were equilibrated under standard conditions, i.e., 4 hr at 750°C. Noteworthy is the fact that a plot of cell emf versus the logarithm of the oxygen concentration is linear over two orders of magnitude in oxygen concentration, extending to levels below 1 ppm oxygen in sodium.

b. Application of the Equilibration Method to the Measurement of Carbon Activity in Sodium

The application of the equilibration method to the measurement of carbon activity in sodium is being investigated. Considerations leading to the selection of iron and vanadium as detector metals were given in ANL-7798. Experiments to determine the equilibrium distribution of carbon between sodium and these metals are being conducted in the sodium loop described in Sect. IV.C.1 below. Iron foils and vanadium and iron wires are exposed at 750°C to cold-trapped liquid sodium with and without a carbon source in the system. Carbon analyses are then performed on the metal specimens after exposure and on sodium samples obtained during the runs.

The results of 10 runs that have been conducted indicate qualitative agreement between the carbon analyses of the sodium samples and the vanadium wires; that is, both indicate the same trend upon increasing and decreasing the carbon activity in the sodium.

The results for the iron are difficult to interpret because most of the carbon values were in the range of 20-30 ppm and did not increase or decrease as expected when a carbon source was either inserted or removed from the loop. Carbon contents in the iron were expected to range from ~5 to 30 ppm, depending on the carbon content of the sodium.

Three potential problems in the use of iron as a detector are being investigated. First, the high diffusivity of carbon in iron can result in a redistribution of the carbon between sodium and iron during cooling of the specimens. Only 10 min are required to equilibrate a 0.37-mm-dia wire at 750°C; therefore, rapid cooling rates are required to retain the equilibrium carbon concentration. Samples with larger cross sections are being used in an attempt to evaluate and eliminate this problem.

Second, possible chromium transport and deposition on the iron may lead to the formation of chromium carbide, which could account for the erratic carbon contents. Thin surface layers of the iron wires will be removed by chemical etching prior to the carbon determinations in an attempt to determine whether this is a problem.

Third, the effect of low concentrations of carbide-forming impurities (e.g., Si, Cr, and Mn) in the Armco iron must be considered in these experiments. Internal carburization of approximately 100 ppm (total) of

these elements could account for ~10 ppm carbon in the iron upon exposure to sodium with a very low carbon activity. To examine this possibility, the Armco iron previously used and higher-purity iron will be equilibrated simultaneously in sodium.

High-purity iron-nickel alloys are also being considered for measurement of carbon activities in sodium. The use of these alloys may overcome one of the principal problems associated with Armco iron, namely, the extremely rapid equilibration and subsequent redistribution of carbon upon cooling.

C. Sodium Effects on Mechanical Behavior of Stainless Steel (02-213)

1. Studies of Carbon Transport in Sodium-Steel Systems. T. F. Kassner and K. Natesan (Last reported: ANL-7798, p. 61)

The objectives of this work are an understanding of the mechanism and kinetics of carburization-decarburization processes involving austenitic and ferritic steels and the eventual correlation of results of these studies with mechanical-property data. Thus, predictions regarding the structural integrity of these steels in a reactor system will be made possible.

a. Distribution of Carbon between Iron-base Alloys and Liquid Sodium

Experiments were continued to obtain data on the equilibrium distribution of carbon between sodium and iron-base alloys. Foil specimens (2 mils thick) of iron, Fe-8 wt % Ni, Fe-18 wt % Cr-8 wt % Ni, and Types 304 and 316 stainless steel were exposed to flowing sodium at temperatures between 600 and 750°C in a loop with a molybdenum test section. In several of the runs, a carbon source was present in the system.

The experimental conditions and results for the experiments performed to date are summarized in Table IV.1. Sodium samples for carbon analyses were obtained in "flow-through" samplers. Each value reported is an average of three carbon determinations on each sodium sample; the samples were analyzed* by the oxyacidic flux method. The foil specimens were cleaned with alcohol and water and then analyzed for carbon by a standard combustion method. Each value in the table is an average of three or more analyses.

The experiments show that in the absence of a carbon source in the system, the carbon concentration in sodium is very low (≤ 1 ppm); however, carburization of Type 304 stainless steel occurred between 600 and 750°C (Runs 1 and 2). The presence of a carbon source increased the

*Analyses performed by W. R. Sovereign, ANL-Idaho.

TABLE IV.1. Experimental Conditions and Results of Carbon Distribution
between Iron-base Alloys and Sodium

Run No.	Run Time, hr	Temp., °C	Carbon Concentration in Exposed Foils					Carbon in Sodium, ppm	Cold-trap Temp., °C	Remarks
			ppm in Fe	ppm in Fe-8Ni	wt % in Fe-18Cr-8Ni	wt % in Type 304 SS	wt % in Type 316 SS			
1	750	700	-	-	-	0.090	-	0.70±0.39,	125	No carbon source.
		600	-	-	-	0.11	-	1.31±0.78		
2	3500	750	14	-	-	0.096	-	0.40±0.20	125	No carbon source.
		650	8	-	-	0.129	-	(at 800 hr), 0.70±0.20 (at 2000 hr)		
3	330	750	80	233	0.71	0.643	1.070	Sample not analyzed.	125	Carburized Fe-8Ni source.
		650	21	238	0.91	0.958	1.149			
4	1000	750	89	97	0.96	0.897	0.940	25±1.0	125	Carburized Fe source.
		650	21	63	1.26	1.270	1.330	(at 300 hr), 1.8±0.4 (at 1000 hr)		
5	60	750	39	57	-	-	-	2.5±1.0	125	No carbon source.
		650	28	98	-	-	-	(at 58 hr)		
6	307	750	15	-	-	1.025	1.160	13.7±1.4	175	Carburized Fe source.
		650	12	-	-	1.193	1.279	(at 140 hr), 11.9±2.5 (at 300 hr)		

carbon activity in sodium, as evidenced by the increase in the carbon concentrations in the alloys and in sodium in Runs 3, 4, and 6. In these latter runs the carbon concentration in the Fe-C alloy source decreased from an initial value of ~5 to ~0.1 wt %; however, the source material was still saturated at the conclusion of the runs. This indicates that the equilibrium between the carbon in sodium and the carbon in the saturated alloy was maintained during the entire run, since there is no kinetic limitation in transporting carbon from the source to the sodium in a loop of this size.

This method of adding carbon to the system can introduce some particulate graphite into the sodium as a result of graphitization of the heavily carburized source and the washing away of the surface particles by the flowing sodium. The carbon concentration in the sodium during the course of Run 4 (carbon source present) showed a substantial decrease which may be attributed, in part, to the presence of graphite particles that are eventually precipitated in the cold trap or other locations in the loop. The cold-trap temperature had a negligible effect on the final carbon concentrations in the steels exposed to sodium in these tests.

To achieve and control carbon levels in the sodium over a range that will result in carbon concentrations below 0.5 wt % in the stainless steels, a different method of adding carbon to the sodium has been devised. In this method, thin-wall tubes of Armco iron are filled with graphite powder and welded closed, and the tubes are inserted in a nickel vessel through which sodium is flowed at temperatures between 450 and 600°C. On the basis of distribution coefficients, it is expected that carbon concentrations in sodium in the range 0.3-7.0 ppm can be attained by this method and that the introduction of graphite particles will be avoided.

Further experiments to determine the equilibrium distribution of carbon between liquid sodium and the various steels will be conducted to obtain sufficient data for comparison with calculated carbon distribution curves.*

b. Measurements of Carbon Activities in Fe-Ni and Fe-Cr-Ni Alloys

Additional data to establish the activity of carbon in Types 304, 316, and 347 stainless steel as a function of the carbon concentration have been obtained at 600°C. The experimental method involves equilibration of the steels in Vycor capsules with Fe-8 wt % Ni alloys whose carbon activities are known or are being determined. The carbon concentrations in the alloys, after an equilibration period of 2800 hr, are given in Table IV.2. The range of carbon activities, as reflected by the carbon concentrations in the Fe-8 wt % Ni alloy in the three experiments, was not as large as was

*K. Natesan and T. F. Kassner, J. Nucl. Mater. 37(2), 223-235 (1970).

desired. Several additional runs at 600°C will be made at higher carbon levels to complete this work. Experiments to establish the carbon activities in the Fe-8 wt % Ni alloy as a function of carbon concentration and temperature are still in progress.

TABLE IV.2. Carbon Analyses of Commercial Alloy Samples
Equilibrated at 600°C for 2800 hr

Capsule No.	Carbon Concentration, ppm			
	Fe-8 wt % Ni	Type 304 SS	Type 316 SS	Type 347 SS
1	30.0	395	425	760
2	50.0	420	455	750
3	55.0	490	540	760

PUBLICATION

Solubility of Helium and Argon in Liquid Sodium

E. Veleckis, S. K. Dhar,* F. A. Cafasso, and H. M. Feder
ANL-7802 (Apr 1971)

*De Paul University.

V. FUELS AND MATERIALS DEVELOPMENT

A. LMFBR Cladding and Structural Materials1. Swelling and Mechanical Behavior of Cladding Alloys (02-605)

- a. Swelling of Type 304 Stainless Steel. P. R. Okamoto, B. J. Kestel, and S. D. Harkness (Last reported: ANL-7833, p. 5.1)

The study of the swelling behavior of solution-annealed Type 304 stainless steel is continuing. Samples prepared from flats 2 and 6 of the guide thimble of EBR-II control rod 5A3 are currently being examined in the transmission electron microscope (TEM) to correlate swelling behavior with microstructure. At present, only four samples have been examined. Average void sizes determined by TEM were used to calculate void number densities from the immersion density measurements. The results, as a function of fluence and irradiation temperature, are summarized in Table V.1.

TABLE V.1. Void Size and Number Densities in Type 304 Stainless Steel from EBR-II Control Rod 5A3

Sample Reference Number	Flat Number	Irradiation Temperature, °C	Fluence, n/cm ²	Immersion Density Change, %	Average Void Diameter, Å	Standard Deviation, Å	Number of Voids Measured	Void Number Density Calculated, 10 ¹⁵ /cm ³
5A3-13	2	398	1.2×10^{23}	-7.7	256	92	762	9.4
5A3-15	2	416	7.4×10^{22}	-5.9	273	68	451	5.8
5A3-48	6	398	1.1×10^{23}	-7.7	243	85	375	10.8
5A3-52	6	450	a	-2.3	164	78	432	10.1

^aNot available.

All samples examined to date exhibited a high number density of voids, incoherent precipitates, and dislocation loops. Selected area diffraction patterns showed $\langle 111 \rangle$ streaking between matrix reflections, indicating that most of the loops are faulted. Another general feature of the microstructure was the association of many of the voids with precipitate particles. This is not entirely surprising, since the form of the point-defect flux to incoherent precipitate particles is expected to be the same as for voids.*

Although only a limited amount of high-fluence TEM data has been obtained to date, a comparison of the present results with electron micrographs obtained from earlier studies on material irradiated in comparable reactor positions to a lower dose indicates that at higher fluences swelling is occurring primarily by void growth.

*S. D. Harkness and Che-Yu Li, Met. Trans. 2, 1457 (1971).

2. Creep, Fracture, and Fatigue Studies on Stainless Steel (02-091)

- a. Low-cycle Fatigue. C. F. Cheng and R. W. Weeks (Last reported: ANL-7825, p. 5.8)

The low-cycle, elevated-temperature, creep-fatigue testing program at ANL is currently providing fatigue data on Type 304 stainless steel in support of FFTF design evaluations and for future LMFBF component design.

The specimens used at ANL to date have been of hourglass configuration and were obtained from the previous General Electric-Nuclear Systems Programs (GE-NSP) low-cycle fatigue research. At GE-NSP, the specimen blanks were annealed at 1092°C for 30 min and air-quenched (about 100°C/min cooling rate) before final machining, and then stress-relieved at 760°C for 15 min and air-quenched after machining. The resultant Vickers Hardness Number was ~139, and the grain size was reported as ASTM 305. The specimens tested at ANL received the same heat treatment as the specimens tested in the former GE-NSP program (see ANL-7825).

Creep-fatigue data generated at ANL are summarized in Tables V.2-V.4. Table V.2 gives ANL base-line results for fully reversed, strain-controlled fatigue tests run to failure. Tables V.3 and V.4 give results obtained in creep-fatigue hold-time tests, where the specimen was subjected to a hold period at the peak of the tensile portion of each strain cycle. It is this interaction of creep and fatigue that is of most concern in design applications, due to the present difficulty in making accurate failure predictions.

We have observed that a thermodynamically unstable microstructure has a significant effect on fatigue life. Figure V.1 is a plot of total axial strain ($\Delta\epsilon_t$) versus time to failure at a $4 \times 10^{-3} \text{ sec}^{-1}$ strain rate on stress-relieved specimens tested at 806, 1050, and 1202°F (Table V.2). Previous GE-NSP* data on stress-relieved specimens (triangles) at 1202°F and BMI** data on annealed and ground specimens (dashed lines) at 1000 and 1200°F are also included in Fig. V.1. Note that at higher strain ranges (0.5-2%) there is a temperature as well as a heat-treatment effect. However, both effects appear to diminish and become negligible as the strain range is lowered to ~0.3%. This is attributed to continuously changing morphology with exposure time, as shown by the time-temperature-carbide precipitation diagrams of Stickler and Vinckier† (Fig. V.2), which indicate that the precipitation of carbide takes place in the

*J. B. Conway, J. T. Berling, and R. H. Stentz, GEMP-702 (June 1969).

**BMI-1903 (Apr 1971).

†R. Stickler and V. Vinckier, Trans. ASM 54, 362-380 (1961).

TABLE V.2. Low-cycle Fatigue Data for Annealed AISI Type 304 Stainless Steel Tested in Air

Test No.	Temp., °F	Axial Strain			Diametral Strain			Strain Rate		Frequency of Loading, cycles/sec	Stress Range $\Delta\sigma$ at $N_f/2$, psi	Fatigue Life			
		$\Delta\epsilon_t$, %	$\Delta\epsilon_p$, %	$\Delta\epsilon_e$, %	$\Delta\epsilon_d$, %	$\Delta\epsilon_{dp}$, %	$\Delta\epsilon_{de}$, %	$\dot{\epsilon}_d \times 10^3$, sec ⁻¹	$\dot{\epsilon}_t \times 10^3$, sec ⁻¹			N_5 , cycles	N_5 , hr	N_f , cycles	N_f , hr
3	806	1.15	0.80	0.35	0.50	0.40	0.10	2.0	-	0.2	82,116	4,290	5.17	4,353	6.22
4	806	2.22	1.66	0.56	1.00	0.83	0.16	2.0	-	0.1	131,440	779	2.32	834	2.47
6	806	0.60	0.37	0.23	0.25	0.19	0.06	2.0	-	0.4	52,800	a	a	29,825	20.71
12	806	2.07	1.65	0.42	1.03	0.91	0.12	-	4.1	0.1	96,208	2,303	6.44	2,361	6.6
21	806	1.07	0.81	0.26	0.48	0.40	0.73	-	4.3	0.2	60,679	10,166	14.12	10,192	14.15
37	806	0.52	0.28	0.25	0.21	0.14	0.07	-	4.2	0.4	57,240	61,806	43.16	61,818	43.17
8	1050	0.58	0.32	0.26	0.24	0.16	0.08	2.0	-	0.4	57,741	11,600	7.89	11,760	8.0
10	1050	2.06	1.58	0.44	0.92	0.79	0.13	-	4.1	0.1	96,248	1,096	2.85	1,139	2.94
11	1050	0.41	0.22	0.20	0.17	0.11	0.06	-	3.3	0.4	44,112	1,024,160	688.5	1,024,330	688.6
13	1050	3.16	2.67	0.49	0.98	0.84	0.15	-	3.8	0.07	108,782	497	2.05	548	2.23
15	1050	1.90	1.46	0.44	0.86	0.73	0.13	1.7	-	0.1	98,323	986	2.71	991	2.72
16	1050	1.18	0.82	0.36	0.52	0.41	0.11	2.0	-	0.2	81,577	2,545	3.47	2,611	3.53
18	1050	3.93	3.40	0.53	1.86	1.70	0.16	3.7	-	0.1	119,162	302	0.84	336	0.93
19	1050	0.99	0.70	0.29	0.44	0.35	0.87	-	3.9	0.2	64,251	a	a	6,708	9.36
22	1050	0.57	0.36	0.21	0.24	0.18	0.06	-	4.5	0.4	43,772	a	a	42,034	29.10
31	1050	0.49	0.29	0.20	0.21	0.15	0.06	-	3.9	0.4	45,216	29,205	19.44	29,568	19.69
32	1050	0.45	0.24	0.21	0.18	0.12	0.06	-	3.6	0.4	47,544	a	a	97,807	67.89
39	1050	1.02	0.67	0.35	0.44	0.34	0.11	-	b	0.002	78,305	1,105	152.7	1,176	162.5
45	1050	0.396	0.195	0.201	0.158	0.097	0.061	-	3.97	0.501	45,110	88,139	48.85	89,513	49.6
50	1050	0.280	0.072	0.209	0.099	0.036	0.063	-	3.74	0.668	46,707	498,576	207.35	506,718	210.74
7	1202	0.60	0.35	0.25	0.25	0.17	0.08	2.0	-	0.4	56,278	6,260	4.25	6,591	4.35
46	1202	0.395	0.181	0.214	0.158	0.091	0.067	-	3.96	0.5	46,149	19,842	11.02	21,524	11.94
47	1202	0.795	0.517	0.278	0.346	0.259	0.087	-	4.25	0.267	59,960	3,457	3.59	3,489	3.63
48	1202	1.61	1.242	0.369	0.737	0.621	0.116	-	4.28	0.113	79,602	904	1.88	1,018	2.12

^aData omitted because of recorder failure.^bStrain rate was 4.1×10^{-5} sec⁻¹.

TABLE V.3. Fatigue Data^a Obtained in Hold-time Tests of AISI Type 304 Stainless Steel in Air

Test No.	Specimen No.	Hold Period, min		$\dot{\epsilon}_t \times 10^3$, sec ⁻¹	Axial Strain Range			Fatigue Life					Temp., °F
		Tension	Compression		$\Delta\epsilon_t$, %	$\Delta\epsilon_p$, %	$\Delta\epsilon_e$, %	N_5 , cycles	N_5 , hr	N_5/N_f	N_f , cycles	N_f , hr	
14	12A-12	600.0	0	4.3	2.13	1.84	0.285	-	-	-	93	919.13	1050
23	14A-1	179.2	0	2.7	1.35	1.05	0.291	224	669.7	0.95	236	704.99	1050
33	15A-4	58.5	0	4.2	1.04	0.75	0.289	476	463.9	0.71	672	655.2	1050
35	15A-5	28.8	0	4.1	1.03	0.738	0.302	478	230.1	0.79	606	290.5	1050
36	15A-6	15.9	0	3.5	0.869	0.451	0.418	329	86.5	0.88	375	99.56	1050
38	15A-8	170.0	0	3.9	1.95	1.646	0.304	132	372.7	0.70	190	539.7	1050
40	15A-10	12.6	0	3.8	0.475	0.241	0.234	2,869	600.76	0.76	3,781	794.27	1050
41	15A-11	15.0	0	4.0	0.997	0.707	0.290	1,112	280.98	0.75	1,509	377.25	1050
44	1A-3	1.0	0	3.94	0.493	0.259	0.234	13,107	217.8	0.91	14,427	240.0	1050
9	12A-6	1.0	0	4.2	2.06	1.76	0.30	295	5.43	0.95	311	5.70	1202

^aControl mode: Axial strain.^bValues are based on the relaxed stress range $\Delta\sigma_r$ at $N_f/2$.

TABLE V.4. Stress Relaxation Data Obtained in Low-cycle Fatigue Tests of AISI Type 304 Stainless Steel in Air

Test No.	Specimen No.	$\Delta\sigma$ at $N_f/2$, psi	$\Delta\sigma_r$ at $N_f/2$, psi	σ_t Maximum at $N_f/2$, psi	σ_t Minimum at $N_f/2$, psi	σ_c Maximum at $N_f/2$, psi	σ_r tension, psi	Total Time under Tensile Stress, hr	Temp., °F
14	12A-12	81,238	63,872	39,321	21,956	41,916	17,365	919.13	1050
23	14A-1	72,295	65,150	35,329	28,184	36,946	3,513	704.99	1050
33	15A-1	73,413	63,653	35,449	25,549	38,103	10,060	655.2	1050
35	15A-5	72,755	67,625	35,848	30,858	36,767	4,990	290.5	1050
36	15A-6	98,503	93,673	48,663	43,832	49,840	4,830	99.56	1050
38	15A-8	80,253	68,002	39,507	27,256	40,746	12,251	539.7	1050
40	15A-10	54,730	52,435	26,487	24,171	28,243	2,295	794.27	1050
41	15A-11	69,920	64,970	33,033	28,084	36,886	4,950	377.25	1050
44	1A-3	54,531	52,375	26,666	24,510	27,864	2,155	240.00	1050
9	12A-6	72,040	65,672	35,821	29,851	35,821	5,970	5.70	1202

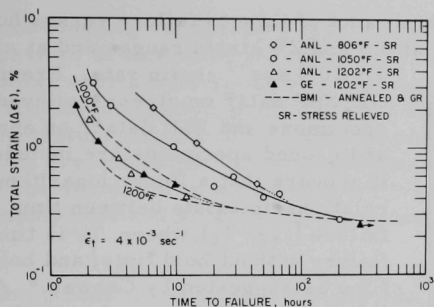
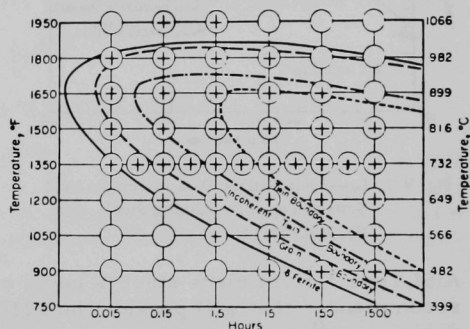


Fig. V.1

Low-cycle Fatigue Data in Fully Reversed Tests of Type 304 Stainless Steel. Neg. No. MSD-54961.

Fig. V.2

Time-Temperature Dependence of Carbide Precipitation. (From Stickler and Vinckier--Type 304 stainless steel, 0.04% carbon.) Neg. No. MSD-54802.



following order: (a) on the austenite-ferrite grain boundaries, (b) on incoherent twin boundaries, (c) on coherent twin boundaries, and (d) inside austenite grains.

Driver* also observed that sensitized austenitic stainless steel (Fe-18 wt % Cr-12 wt % Ni) with carbide precipitation at grain boundaries has a longer fatigue life in the 600-800°C range than when tested in the corresponding solution-annealed condition. Thus a stress-relieved specimen (ANL) is expected to fail later than an annealed and ground specimen (BMI) under a corresponding test condition above 1/2% total axial strain range (see Fig. V.1). The same reasoning can be extended to explain the temperature effect. With extended exposure time (>100 hr), all the specimens in Fig. V.1 tend to approach similar morphology. The question remains whether the temperature effect is significant in the range of 806-1202°F for the thermodynamically stable microstructure. This question is extremely important in furnishing the designer with a realistic failure prediction and will be answered as part of the ANL program.

*J. H. Driver, Metal Science 5, 47-50 (1971).

Figure V.3 is a logarithmic plot of time to failure versus hold time on stress-relieved specimens at 0.5 and 2% strain ranges and at a $4 \times 10^{-3} \text{ sec}^{-1}$ strain rate. Previous GE-NSP data* on stress-relieved specimens and BMI data** on annealed and ground specimens are included. It appears that a linear logarithmic relationship exists between time to failure $[(T_f - T_0)]$, where T_0 is time to failure without hold time and hold time as suggested by Conway.* Additional tests are required to confirm this relationship.

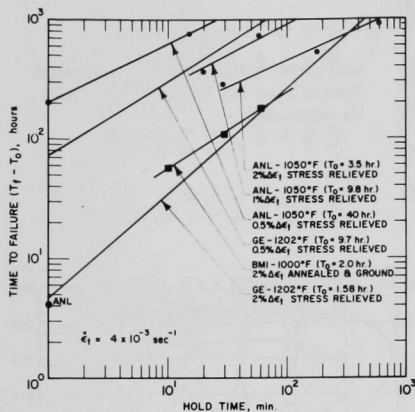
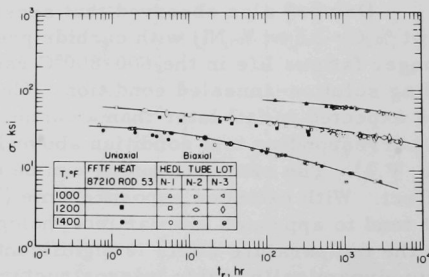


Fig. V.3. Low-cycle Fatigue Data in Tension Hold Tests of Type 304 Stainless Steel. Neg. No. MSD-54811.

AISI Type 316 stainless steel is being evaluated so that a correlation can be recommended that will provide the LMFBR fuel-element and component designer with a confident means of extrapolating the rupture data. Also, this study will aid in determining the remaining areas where data are most needed.

The uni- and biaxial stress-rupture data obtained by WADCO† are summarized in Fig. V.4. The engineering hoop stresses are used in the

Fig. V.4
Stress-Rupture Behavior of
20% Cold-worked Type 316
Stainless Steel. Neg. No.
MSD-54962.



*J. B. Conway, J. T. Berling, and R. H. Stentz, GEMP-702 (June 1969).

**BMI-1903 (Apr 1971).

†L. D. Blackburn et al., Quarterly Progress Report, HEDL-TME-71-43, p. 213 (1971); M. M. Paxton, Interim Report, HEDL-TME-71-59 (Apr 1971).

biaxial loading condition. Figure V.4 illustrates that the creep-rupture behaviors of this material under uni- and biaxial loading conditions are similar over a wide range of stress and temperature. Thus, if this similarity can be firmly established, the biaxial behavior for this stress and temperature range can be readily estimated from the uniaxial results, which are, experimentally, much easier to obtain. The uniaxial results will be discussed in terms of how the biaxial data correlate with the relationship obtained solely from the uniaxial test.

As has been shown,* the rupture life (t_r) under a uniaxial loading condition at elevated temperatures is inversely proportional to the minimum creep rate ($\dot{\epsilon}_{\min}$). Since the minimum creep rate, in turn, can be well correlated empirically** with stress by an expression of the form

$$\dot{\epsilon}_{\min} = A[\exp(-Q/RT)][\sinh(\alpha\sigma)]^n, \quad (1)$$

the rupture life can then be expressed as

$$t_r = A'[\exp(Q/RT)][\sinh(\alpha\sigma)]^{-n}. \quad (2)$$

Here Q is the activation energy for creep and is normally equal to that for self-diffusion in pure metals. The constants α and n may depend on temperature and stress.

Using the values of α and Q deduced by Bates *et al.*[†] on solution-treated Type 316 stainless steel, the minimum creep rates of 20% cold-worked Type 316 stainless steel are presented according to Eq. 1 in Fig. V.5. Excellent correlation is evident. The least-square-fit procedure gives

$$\dot{\epsilon}_{\min} = [\exp(59.64 - 116000/RT)][\sinh(1.79 \times 10^{-5} \sigma)]^{8.82}. \quad (3)$$

The rupture data are then correlated according to Eq. 2, as shown in Fig. V.6. The correlation is again good. Least-square fit of these data yields

$$t_r = \{\exp[-(62.49 - 116000/RT)]\}[\sinh(1.79 \times 10^{-5} \sigma)]^{-8.81}. \quad (4)$$

Equations 3 and 4 clearly indicate that the usual correlation of $t_r \propto \dot{\epsilon}_{\min}^{-1}$ also appears to hold in this material.

The biaxial stress-rupture data in Fig. V.4 are replotted in Fig. V.7 using the same constant as in the uniaxial case. The agreement is fairly good, except in the lower stress range at the highest temperature. In this region, additional biaxial and uniaxial data will be needed to establish whether the correlation is still valid.

*I. S. Servi and N. J. Grant, Trans. AIME 191, 909 (1951).

**F. Garofalo, Fundamentals of Creep and Creep-Rupture in Metals, MacMillan Co., New York (1965).

†J. F. Bates, E. R. Gilbert, and A. J. Lovell, WHAN-FR-25 (Oct 1970).

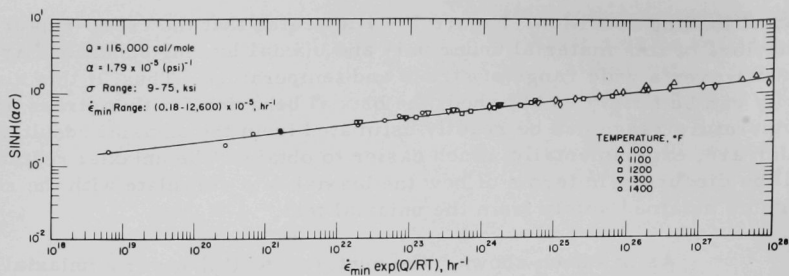


Fig. V.5. Minimum Creep Rate vs Uniaxial Stress of 20% Cold-worked Type 316 Stainless Steel. Neg. No. MSD-54966.

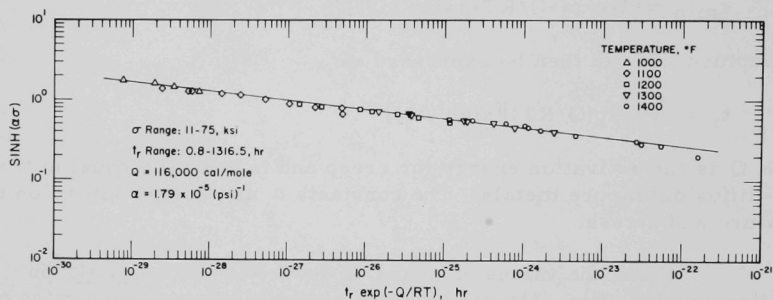


Fig. V.6. Rupture Life vs Uniaxial Stress of 20% Cold-worked Type 316 Stainless Steel. Neg. No. MSD-54965.

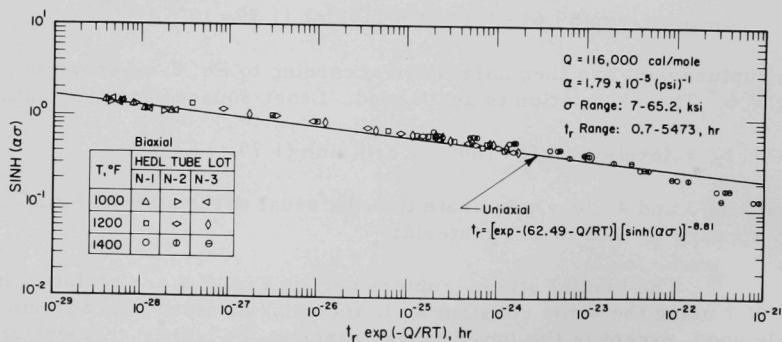


Fig. V.7. Rupture Life vs Biaxial Stress of 20% Cold-worked Type 316 Stainless Steel. Neg. No. MSD-54964.

The above method of correlation is being extended to AISI Type 304 stainless steel.

3. Nondestructive Testing Research and Development (02-092)

- a. Fast-neutron Radiography with ^{252}Cf . H. Berger and N. P. Lapinski (Last reported: ANL-7742, p. 109)

An evaluation of fast-neutron radiography with ^{252}Cf spontaneous fission sources has been completed. The study also yielded information about fission neutron-exposure requirements for several image-detection methods. The investigation was conducted with a 1.99-mg source fabricated at ORNL and loaned to ANL for this purpose. Additional tests were made with a 4.74-mg source available at ANL for other work. In each case, the physical sizes of the sources (approximately right cylinders 3 mm in diameter and 1-2 mm in height) were larger than could be contemplated for a high, specific-activity material such as ^{252}Cf . This large size influenced some of the results by contributing an image with less sharpness than might be achieved under optimum conditions.

Tests were conducted with three detection systems. One involved direct-exposure techniques with fast X-ray film and either fluorescent or plastic screens. In each case (n,p), reactions in the hydrogenous screens and film components provided the primary detection mechanism. Because of the relatively high gamma-radiation background from the source,* direct-exposure tests were conducted with and without lead and bismuth filters (thicknesses 0.3-1.2 cm) near the source. The filters appeared to lead to somewhat improved neutron-radiographic contrast of hydrogenous objects, but yielded noticeably less sharp radiographs, probably the result of scattering in the filter material. Typical exposure requirements for direct-exposure tests are given in Table V.5. The exposures required for the filtered beam are comparable to those found necessary** for exposures of similar detectors to 3- and 14-MeV neutrons.

The other two exposure methods studied were track etch and activation transfer. In each case, essentially no sensitivity to gamma radiation was detected. The track-etch approach yielded outline images of relatively high-contrast objects. Exposures were limited to cellulose nitrate plastics in which reactions such as $^{14}\text{H}(n,\alpha)^{11}\text{B}$, $^{16}\text{O}(n,\alpha)^{13}\text{C}$, and $^{12}\text{C}(n,n')3\alpha$ provided the response.† Tests were made with Eastman-Kodak Type 106-01 and Kodak Pathé Types CA8015 and LR115 film. All gave comparable results and required total exposures on the order of 2×10^{11} n/cm². This is an order of magnitude higher than exposures†† found necessary

*D. H. Stoddard, Radiation Properties of Californium-252, USAEC Report DP-986, Savannah River Laboratory, Aiken, S.C. (1965).

H. Berger, *Mater. Eval.* **27, 245-253 (1969); H. Berger, *Intl. J. Appl. Radiation and Isotopes* **21**, 59-70 (1970).

†A. L. Frank and E. V. Benton, Proc. Intl. Conf. on Nuclear Track Registration in Insulating Solids and Applications, Clermont-Ferrand, France (1969).

††H. Berger, *Intl. J. Appl. Radiation and Isotopes* **21**, 59-70 (1970).

for 14-MeV neutrons, which probably reflects the lower cross sections for the indicated reactions of the lower-energy neutrons from ^{252}Cf .

TABLE V.5. Neutron-exposure Requirements for Direct-exposure Methods

Detector	Beam Filter	Exposure to ^{252}Cf Neutrons for Total Density ^a of 1.5, $\text{n/cm}^2\text{-sec}$
Kodak no screen	None	2.3×10^8
X-ray film with plastic screens ^b		3.9×10^8
Kodak Royal Blue	1.2 cm bismuth ^c	1.6×10^7
X-ray film with Radelin TF fluorescent screens ^d		3×10^7

^aManufacturer's recommended processing (hand method) was used.

^bFilm was sandwiched between two screens of Lucite, each 0.75 mm thick.

^cFilter was placed adjacent to the neutron source.

^dFast-neutron intensity was about $7 \times 10^4 \text{ n/cm}^2\text{-sec}$. Results would be expected to vary for other intensities because of reciprocity-law failures.

From the standpoint of radiographic contrast, the best results were obtained with the transfer-detection method. Useful transfer reactions are given in Table V.6. Exposure requirements for these transfer detectors are given in Table V.7, which also includes some comparisons of results for 3- and 14-MeV-energy, accelerator-produced neutrons. Conditions for the tests involved activation times of 30 min and 16 hr and a time between activation and transfer to film of 2 min for the accelerator results and 10 min for the ^{252}Cf results. (The hot-cell arrangement for the radioactive-source exposures necessitated the longer times.) Exposures were made on fast X-ray film with lead-backed screens. The use of lead screens had previously been shown* to yield an intensification on the order of 20%. Film

TABLE V.6. Characteristics of Transfer-detector Materials

Reaction	Abundance of Target Isotope in Normal Material, %	Threshold Neutron Energy for Reaction, MeV	Half-life	Reaction Cross Section, Millibarns for Neutrons of Energy		
				1 MeV	3 MeV	14 MeV
$^{31}\text{P}(\text{n},\text{p})^{31}\text{Si}$	100	1.8	2.65 hr	-	80	140
$^{32}\text{S}(\text{n},\text{p})^{32}\text{P}$	95	1.7	14.3 days	-	150	220
$^{103}\text{Rh}(\text{n},\text{n}')^{103\text{m}}\text{Rh}$	100	<0.1	57 min	450	800	-
$^{111}\text{Cd}(\text{n},\text{n}')^{111\text{m}}\text{Cd}$	12.7	0.3	48.7 min	130	300	-
$^{115}\text{In}(\text{n},\text{n}')^{115\text{m}}\text{In}$	95.7	0.5	4.5 hr	55	340	-

*H. Berger, Intl. J. Appl. Radiation and Isotopes 21, 59-70 (1970).

TABLE V.7. Neutron Intensities for Transfer-detection, Fast-neutron Radiography^a

Activation Material ^b	Neutron Intensity for 30-min Exposure and Transfer to Fast X-ray Film to Yield Total Film Density 1.5			Neutron Intensity for 16-hr Exposure to ²⁵² Cf Neutrons and Transfer to Fast X-ray Film to Yield Total Film Density 1.5, n/cm ² -sec
	14-MeV Neutrons of Energy, n/cm ² -sec	3-MeV Neutrons of Energy, n/cm ² -sec	²⁵² Cf Fission-energy Neutrons, n/cm ² -sec	
Phosphorus ^c	2.5×10^7	4.4×10^7	1.5×10^8	1.4×10^7
Sulfur ^d	2.3×10^7	2.3×10^7	5×10^7	1.5×10^6
Indium	-	1×10^8	1.4×10^8	8.5×10^6
Cadmium	-	$>10^9$	$>10^9$	$\sim 10^9$
Rhodium	-	$\sim 10^9$	$>10^9$	$\sim 10^9$

^aSee text for conditions of tests.^bMetal foils were used except as indicated.^cPhosphorus was fabricated to sheet form by a mixture of eight parts red phosphorus to one part silicone resin by weight.^dPressed powder pellets and melted layers were used.

exposures were made for three half-lives or more, except for sulfur, for which only one half-life was used. Film results were made equivalent to Eastman-Kodak Type KK or Kodak-Pathé Type Kodirex film. The 30-min activation results for ²⁵²Cf are shown (see Table V.7) for comparison with the previously obtained accelerator-source studies. Longer exposures, such as the overnight time represented by the 16-hr-exposure results, are more practical for the radioisotope source.

An examination of even the long-term results, however, emphasizes some of the difficulties with typical source sizes and radiographic geometries. For the 4.74-mg source of ²⁵²Cf, the required intensity of 1.5×10^6 n/cm²-sec for sulfur dictates a source-to-detector distance of about 24 cm (assuming negligible absorption in the radiographic object). For the more reasonable half-life detector indium, the distance is only about 10 cm. Larger activity and physically smaller sources, multiple activation screens,* and similar variations may lead to some improvements in the relatively poor image-sharpness characteristics that result from these values.

Radiographic studies were conducted with hydrogenous objects (rubber and plastic) on steel plates, inasmuch as the objects appear to represent a reasonable industrial type of application for neutron radiography. Observations of a rubber O-ring, ~4.5 mm thick on 1.27 cm of steel, were marginal when direct-exposure methods were used. A slight improvement in contrast was attained when a lead or bismuth filter was used. Transfer exposures produced improved contrast of this object, indicating that direct-exposure methods were probably seeing some contrast-reducing secondary radiation. However, a further improvement of contrast was obtained with X-ray or γ -ray (¹⁹²Ir) radiographs.

*Ibid., see previous page.

One must therefore conclude that fast-neutron radiography with ^{252}Cf neutron sources offers limited potential for general industrial applications. Complicating situations, such as radioactivity of the radiographic object, may tend to favor the use of neutron techniques. Since this situation would dictate the use of a gamma-insensitive detector (probably the transfer type), one would be faced with poor imaging geometry. For this purpose, physically small (~1 mm or less) sources of relatively large size (10 mg or more) would offer significant advantages.

- b. Thermal-neutron Radiography. J. P. Barton (Last reported: ANL-7825, p. 5.12).

Work is continuing on the evaluation of the potential of ^{252}Cf for thermal-neutron radiography. Using optimum techniques, ^{252}Cf radiographs have now been achieved that are equal in quality to those obtainable with the Juggernaut reactor. Quantitative comparisons of the reactor and ^{252}Cf radiographs have been obtained using the VISQI test system.* An exposure of 120 mg-hr is sufficient to provide a ^{252}Cf source thermal-neutron radiograph equal to that obtainable from the reactor with 1:25 collimation, gadolinium converter, and single R film.

A series of nine scintillator designs has been tested for the ^{252}Cf facility. The scintillators were comprised of a homogeneous mixture of Li^6F , ZnS , and binder; variables were particle size, mixture proportions, and thickness. Scintillators previously used in the ^{252}Cf evaluation consisted of large-grain ZnS (20-40 μ), and a mixture of two parts ZnS to one part Li^6F by weight. Distinct improvements were possible by reducing the grain size of ZnS (7 μ) and increasing the proportion of Li^6F (two parts Li^6F , one part ZnS). Such screens, when used with Kodak Royal Blue film, provided ^{252}Cf radiographs superior in quality to those of gadolinium and no-screen film. These scintillator converters were more efficient than the foil-film combination by a factor of 12.

- c. Development of Pulsed Eddy-current Equipment for Testing Fuel-element Jackets in FEF. C. J. Renken and D. Hutchinson (Last reported: ANL-7825, p. 5.9)

This equipment has been constructed, tested, and shipped to ANL-Idaho. It consists of electronic circuitry, test probes, and a test jig that is designed to permit the testing of 6.34-mm (0.250-in.) nominal-diameter fuel elements with the spacing wire still attached. All the design criteria, which were discussed in ANL-7825, were fulfilled.

*J. P. Barton, A Visual Reading Image Quality Indicator (VISQI) Used for Neutron Radiography, Mater. Res. Stand., to be published.

4. NDT Characterization of Cladding Alloys (02-133)

- a. NDT Measurement of Effective Cold Work in Cladding Tubes.
C. J. Renken and N. J. Carson (Last reported: ANL-7783, p. 70)

The mechanical-modulation method of measuring small amounts of permanent magnetism is being used to check the correlation between magnetic retentivity and cold work in Type 316 stainless steel. The weak permanent magnetism exhibited by Type 316 stainless steel is believed to be the result of the transformation of a small amount of austenite into martensite during cold working. In cold-worked rods produced by pulling in pure tension, good correlation between the retentivity and the true strain was observed. The amount of martensite seemed to be some type of an exponential function of the true strain. Good correlation has also been observed in some lots of tubing. The martensite does not appear to be important in hardening the tube during the working of Type 316 stainless steel. Its usefulness for a nondestructive test of cold work is only as a conveniently measured indicator of the strain history of the metal. If the martensite is to serve as a useful indicator of strain history, however, it is apparently important that the heat treatment before cold work produce a stable and reproducible austenitic structure with essentially no martensite present. This can be accomplished by a heat soak at 1850-1900°F, followed by rapid cooling. Annealing practices in tubing mills do not always meet the requirement of low martensite in as-annealed tubing. The presence of appreciable martensite in the tubing before cold working diminishes the usefulness of magnetic retentivity as an indicator of cold work, especially for low values of cold work. Another problem with magnetic retentivity for cold-work measurements is the presence of excess work in the surface layers of the tube. Since the buildup of martensite in Type 316 stainless steel with cold work is an exponential function of the cold work, the presence of a thin but highly worked surface layer can account for a considerable portion of the retentivity of the tube. This surface layer depends upon such variables as the lubricant used during the reduction and is not directly related to the cold work in the bulk of the tube wall. Experiments are under way to define these two effects on magnetic retentivity as an indicator of cold working in Type 316 stainless steel and to investigate methods of correcting them. Even at this stage of our program, however, it can be concluded that retentivity provides a valuable tool for characterizing the structure of austenitic stainless steel.

B. Fuel Properties

1. High-temperature Properties of Ceramic Fuels (02-094)

- a. Plastic Yielding and Fracture of Mixed Oxides. J. T. A. Roberts and B. J. Wrona (Last reported: ANL-7783, p. 71)

A second batch of high-density (97% TD, O/M \approx 1.97) UO_2 -20 wt % PuO_2 with a grain size of $\sim 6 \mu$ was tested in four-point bending at

a strain rate of $\sim 0.07 \text{ hr}^{-1}$ over a temperature range of $1000\text{--}1700^\circ\text{C}$. The temperature dependence of the strength and yield stress is shown in Fig. V.8.

The brittle-fracture stress σ_F is temperature-dependent and follows the equation

$$\sigma_F(6\mu)(\text{kg/cm}^2) = 629.4 + 0.375 T (^\circ\text{C}).$$

This has a somewhat lower temperature dependence than the $2\text{-}\mu$ specimens tested earlier (see ANL-7783) that obeyed the equation

$$\sigma_F(2\mu)(\text{kg/cm}^2) = 360 + 0.564 T (^\circ\text{C}).$$

However, there is little difference in fracture stress between the two batches at temperatures between 1000°C and the brittle-to-ductile transition T_C .

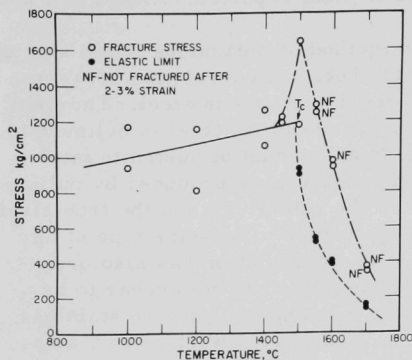


Fig. V.8. Temperature Dependence of the Strength of $6\text{-}\mu$ Grain Size $\text{UO}_2\text{-}20 \text{ wt } \%\text{PuO}_2$. Neg. No. MSD-55109.

As previously observed, T_C is located at the temperature where maximum strength is observed, but it is 45°C higher than T_C for the $2\text{-}\mu$ specimen. Also, as before, the strength decreases rapidly above T_C , and specimens develop extensive ductility and remain unfractured after straining to the limits of the apparatus, i.e., $\sim 2\text{--}3\%$ of the outer fiber strain.

All the fine grain-size ($\lesssim 6\mu$, density range $88\text{--}97\%$ of theoretical) specimens tested to date have exhibited enhanced plasticity at temperatures $\gtrsim 100^\circ\text{C}$ above T_C . In fact, two specimens with a grain size of 2μ were deformed to $\sim 10\%$ strain without fracture by bending in one direction, reversing the specimen, and repeating the procedure. In contrast, in UO_2^* (97% TD, grain size = $8\text{--}31\mu$), fracture normally occurred after $2\text{--}3\%$ strain. Some insight into the mechanism(s) responsible for this ductility can be obtained by determining the strain-rate sensitivity m . In four-point bending, the parameter m_b (equivalent to $m = \partial \ln \sigma / \partial \ln \dot{\epsilon}$) is given by**

$$m_b = \left(\frac{\partial \ln M_b}{\partial \ln \dot{\epsilon}} \right)_\epsilon,$$

where M_b is the bending moment = $Wa/2$ (a = distance between inner and outer loading points), and $\dot{\epsilon}$ is the strain rate.

*R. F. Canon, J. T. A. Roberts, and R. J. Beals, J. Am. Ceram. Soc., **54**(2), 105–112 (1971).

**A. H. Heuer, R. M. Cannon, and W. J. Tighe, Ultrafine Grain Ceramics, Syracuse University Press, Syracuse, New York, 1970, Ch. 16, p. 344.

Using the 2- μ grain-size specimens as examples, m_b values were determined as a function of strain by (a) examination of the strain-rate dependence of the yield stress (elastic limit), (b) effect of strain rate on the plastic flow curves at 1700°C and strain rates of 0.15 and 0.34 hr⁻¹, and (c) stress-relaxation experiments at 1700°C. The results are presented in Table V.8. Data on the yield stress were reported previously (see ANL-7783). The flow curves are plotted in Fig. V.9, and Fig. V.10 shows plots of $\log \partial W / \partial t$ versus $\log W$ used to determine m_b from stress relaxation. (The slope of the line in Fig. V.10 yields m^{-1} , according to the relation $\dot{\epsilon} = A \sigma^n e^{-\Delta H / RT}$, where A is a structure-sensitive constant, ΔH is the activation enthalpy, RT has the usual meaning, and $n = m^{-1}$.)

TABLE V.8. Strain-rate Sensitivity Measurements

Technique	Temperature, °C	Strain Rate, hr ⁻¹	M_b	Strain ϵ_p , %
Effect of strain rate on yield stress (elastic limit)	1500-1700	0.15-0.73	0.5	~ 0
Effect of strain rate on flow curve	1700	0.15-0.37	0.51	~ 0 to 2
Stress relaxation	1700	0.15 and 0.37	0.6	2.78 ^a 2.24
Stress relaxation	1700	0.15	0.66	4.8 ^a

^aSpecimen was turned over and test repeated to obtain 4.8% accumulated strain.

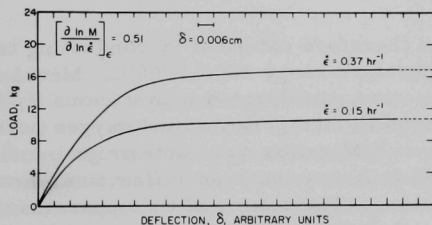
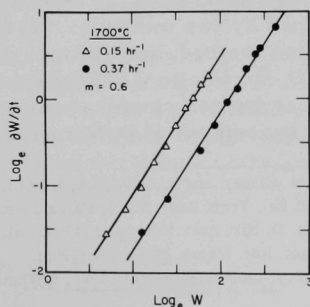


Fig. V.9

Effect of Strain Rate on Flow Curves at 1700°C. Neg. No. MSD-55108.

Fig. V.10
W Plots of $\log_e \partial W / \partial t$ vs $\log_e W$
from Stress-relaxation Tests.
Neg. No. MSD-55107.



The strain-rate sensitivity shows a slight increase with strain and lies in the range 0.5-0.66, as shown in Table V.8. In contrast, values of m equal to 1.0 or 0.2-0.22 (i.e., $n = 1$ or 4.5-5) are generally measured in UO_2^* and other ceramics. The former value is associated with diffusional deformation that includes grain-boundary sliding,** whereas the latter value indicates the occurrence of a dislocation climb and/or glide process.† Intermediate values suggest a combination of both grain-boundary sliding and grain slip, which is only possible if the grain size is small and a sufficient number of independent slip systems are present. These conditions are more generally found in the "superplastic" metallic alloys,†† but the present results suggest that ceramic materials are also capable of exhibiting superplasticity under certain conditions.

b. Thermodynamic Behavior of Mixed-oxide Fuels. N. A. Javed
(Not previously reported)

An integral part of the program to determine the effects of non-stoichiometry on the mechanical properties of mixed-oxide fuels (based on the solid solution of 80% UO_2 and 20% PuO_2) is the provision of the appropriate oxygen partial pressures to maintain the particular oxygen-to-metal ratio (O/M) during testing. Thermodynamic data at relatively low temperatures (800-1100°C) have been reported‡ for solid-solution compositions of $(\text{U}_{0.7}, \text{Pu}_{0.3})\text{O}_{2\pm x}$, $(\text{U}_{0.85}, \text{Pu}_{0.15})\text{O}_{2\pm x}$, and $(\text{U}_{0.89}, \text{Pu}_{0.11})\text{O}_{2\pm x}$, using the electromotive force (emf) technique. However, apart from differences in the plutonium content, these data must be extrapolated to relatively higher temperatures (1400-1700°C) to be relevant to the mechanical-property studies.

This earlier work was therefore extended by conducting transpiration experiments in the temperature range 1000-1700°C. Mechanically mixed granules of $(\text{U}_{0.8}, \text{Pu}_{0.2})\text{O}_{2\pm x}$ were equilibrated with various $\text{H}_2/\text{H}_2\text{O}$ mixtures for 6-28 hr, depending upon the temperature and oxygen partial pressure. Following quenching, the O/M ratios were determined, and some selected specimens were subjected to X-ray, neutron-diffraction, metallographic, and microprobe examinations. The details of the apparatus, the atmosphere-control arrangements, and the X-ray measurements have been described (see ANL-7783, p. 73, and ANL-7825, p. 5.19). The O/M ratios were determined by two methods: (a) total oxygen determination by the inert-gas-fusion method, and (b) measurement of weight changes after adjusting the O/M ratio to 2.000 by equilibration in CO/CO_2 at 850°C (equivalent to an oxygen chemical potential of ~ 97 kcal/mole). The reproducibility and agreement of O/M ratios determined by these methods are

*M. S. Seltzer, A. H. Clauer, and B. A. Wilcox, *J. Nucl. Mater.* **34**, 351 (1970).

**M. F. Ashby and R. Raj, *Tech. Rept. No. 2*, Harvard University (July 1970).

†C. R. Barret and W. D. Nix, *Acta Met.* **13**, 1247 (1965).

††T. A. Alden, *J. Aust. Inst. Metals* **14**(4), 207 (1969).

‡T. L. Markin and E. J. McIver, *Plutonium 1965*, Chapman and Hall, London, p. 845.

within ± 0.005 . X-ray and metallographic examinations of the equilibrated specimens with $O/M < 1.98$ did not reveal the two phases reported by Sari *et al.**.

The results of these experiments have been plotted as $\Delta\bar{G}_{O_2}$ versus O/M for various temperatures, as shown in Fig. V.11. For an $O/M = 1.98-2.06$, the data of Markin and McIver,** extrapolated to high

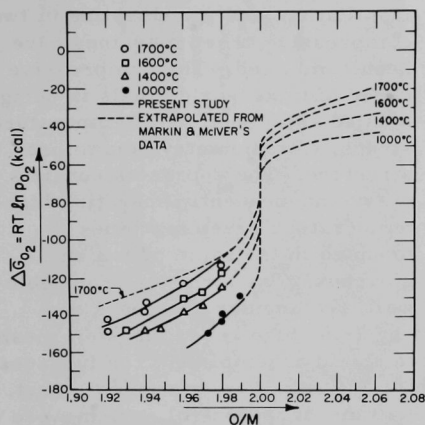


Fig. V.11. Oxygen Chemical Potentials of $(U_{0.8}, Pu_{0.2})O_{2+x}$ vs Oxygen-to-Metal Ratio at Various Temperatures. Neg. No. MSD-55106.

temperatures, have also been plotted to include the hyperstoichiometric region. There is good agreement with the extrapolated values of Markin and McIver to $O/M = 1.96$, but below 1.96, the $\Delta\bar{G}_{O_2}$ values reported in the present study are consistently lower. For example, in Fig. V.11, the 1700°C isotherm shows that at $O/M = 1.92$ the difference in $\Delta\bar{G}_{O_2}$ values is about 7 kcal. Similar discrepancies exist at other temperatures, but the data were excluded to avoid confusion. Possible errors in the present study due to nonattainment of equilibrium or thermal diffusion were insignificant. However, there are at least two reasons for discrepancies in the O/M region < 1.96 . First, possible changes in composition may occur during the cooling period after quenching. It might be mentioned, however, that

the specimens were quenched by turning off the furnace, and, after approximately 1 min during which the maximum temperature drop occurred, an $\sim 10^{-5}$ mm Hg vacuum was substituted for the H_2/H_2O atmosphere to avoid any contamination of the final products with H_2 , H_2O , or oxygen. Secondly, a combination of errors resulting from O/M determinations, impurities in the starting materials, extrapolation, the emf measurements, and different plutonium contents may be responsible for the discrepancies.

A plot of $\Delta\bar{G}_{O_2}$ versus temperature was constructed for various O/M values, as shown in Fig. V.12, from the smoothed isotherm lines in Fig. V.11. The oxygen chemical potentials that can be obtained from the various H_2/H_2O ratios (or dew points) at different temperatures were also included. Figure V.12 will be useful in controlling stoichiometry during sintering and in studying the physicochemical properties of $(U_{0.8}, Pu_{0.2})O_{2-x}$ as a function of stoichiometry.

*C. Sari, U. Benedict, and H. Blank, *J. Nucl. Mater.* **35**, 267 (1970).

**T. L. Markin and E. J. McIver, *Plutonium 1965*, Chapman and Hall, London, p. 845.

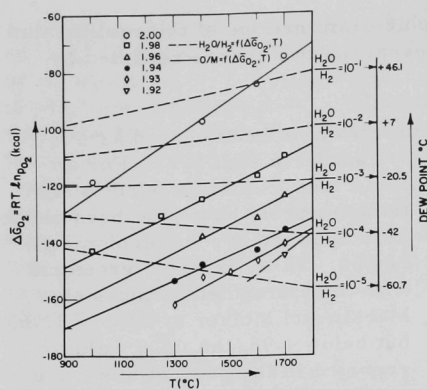


Fig. V.12. Oxygen Chemical Potentials of $(U_{0.8}Pu_{0.2})O_{2-x}$ as a Function of O/M, Temperature, and H_2O/H_2 . Neg. No. MSD-54877.

stainless steel, each housing a 3-in.-dia by 7-in.-high set of tungsten-mesh heating elements and associated radiation shield assemblies. The furnaces are capable of operating to $2500^{\circ}C$, with $\pm 1/4^{\circ}C$ stability, in vacuum, inert, or reducing atmospheres. Details of the atmosphere-control system were reported in ANL-7783, p. 73.

A tungsten compression cage (see Fig. V.13) is used to apply stress to cylindrical samples by means of a deadweight load suspended from the lower pull rod. Loads up to 1000 lb can be transmitted to the specimen through flexible connections at the bottom of both the furnace and glovebox enclosures. Self-alignment of the compression cage is achieved by a ball and socket seal at the top of the upper pull rod. A similar arrangement at the junctions of the pull rod and pull-rod flanges uses boron nitride bushings as a high-temperature lubricant. Contamination of the specimen by the tungsten-load platens is avoided by using thoriated tungsten disks, which also have improved microstructural stability.

The methods used to determine length changes in the sample are by measuring (1) the displacement of the lower pull rod with a linear-variable-differential transformer (LVDT), and (2) the relative displacements of the two platens in contact with the sample by means of a scissors-type extensometer coupled to a second LVDT. Because of the complications with the extensometer arrangement, it has been necessary to rely on measurements of the lower pull-rod movement only.

To check the reproducibility of the continuous deformation-monitoring arrangement, two identical UO_2 -25 wt % PuO_2 pellets were

c. Compressive Creep of Mixed-oxide Fuels.

J. L. Routbort,
N. A. Javed, and
J. C. Voglewede (Not
previously reported)

The design, construction, installation, and proof testing of two compressive creep machines have been completed. The compressive creep of mixed-oxide fuels is being studied as a function of temperature, stress, stoichiometry, and microstructure. The apparatus consists of two independently operating high-temperature creep machines mounted in the same plutonium glovebox. The furnaces are double-wall, rectangular chambers of

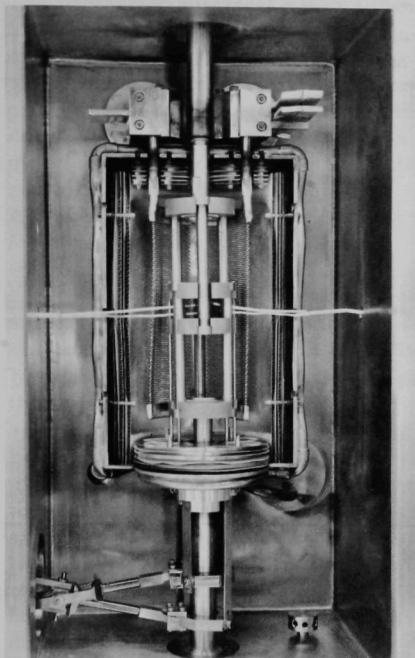


Fig. V.13. Interior of Compressive Creep Furnace. Neg. No. MSD-53705.

structure on creep between 1400 and 1600°C and in the stress range 1500-6000 psi. The other series of experiments will be made to study the effect of stoichiometry ($1.90 < O/M < 2.00$) on creep in similar stress and temperature ranges. Test specimens are UO_2 -25 wt % PuO_2 fabricated by UNC

creep-tested simultaneously at 1500°C and ~3000 psi. The furnace atmosphere during the tests was purified hydrogen, which produced an equilibrium oxygen partial pressure of approximately 10^{-21} atm. The specimens were equilibrated for 16 hr before loading. One of the strain-versus-time curves is shown in Fig. V.14. The results of the two tests are summarized in Table V.9.

The accumulated strains determined from the initial and final lengths of the sample and as measured by the LVDT differ by $\approx 2\%$. This indicates that the deformation in the loading system has negligible effect on the lower pull-rod displacement as measured by the LVDT. Moreover, the 7% difference between the steady-state creep rates is probably due to inherent differences in the specimen microstructures.

Two parallel and related programs are being conducted using these creep machines. One series of experiments will study the effect of micro-

Fig. V.14

Typical Strain-vs-Time Curve.
Neg. No. MSD-54923.

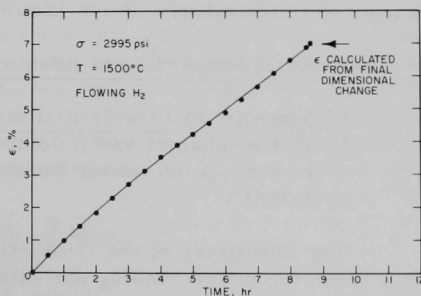


TABLE V.9. Comparison of Creep Apparatus

	Apparatus A	Apparatus B
UO ₂ -25 wt % PuO ₂ Sample number	1402-B	1402-C
Initial length, mm	5.510	5.605
Initial diameter, mm	5.607	5.614
Final length, mm	5.128	5.243
Final diameter, mm	5.853	5.847
Temperature, °C	1500	1500
Stress, psi	2995	3021
Atmosphere	Flowing H ₂	Flowing H ₂
Steady-state strain rate $\dot{\epsilon}$, hr ⁻¹	$7.46 \pm 0.04 \times 10^{-3}$	$6.99 \pm 0.06 \times 10^{-3}$
ϵ , % (calculated from dimensional changes)	6.98	6.46
ϵ , % (calculated from deformation versus time curve)	6.93	6.59

and made available to us by WARD. The initial O/M ratio is ~1.96, the metallic impurity level is <500 ppm (C \approx 150 ppm, Fe \approx 100 ppm), the length-to-diameter ratio is ~1.0, the density range is 89-95% of theoretical, and the grain size ranges from 2 to 25 μ .*

- d. Irradiation Effects in Creep of Oxide Fuels. A. A. Solomon
(Last reported: ANL-7833, p. 5.5)

The second UO₂ creep capsule is continuing to function well in the GETR. Creep rates at ~80°C and a shear stress of ~2400 psi have now been measured at four fission rates, the maximum being $\sim 1 \times 10^{13}$ fissions/cm³-sec. The creep rate increases with an increase in fission rate. This behavior was also observed in the Battelle Memorial Institute in-pile creep experiments at temperatures above 1000°C.

2. Thermochemical Properties of Reactor Fuels (02-162)

- a. Fission-product Oxide Redistribution and Cladding Interaction.
C. E. Crouthamel and I. Johnson, CEN (Last reported:
ANL-7783, p. 86, under Total Effusion of Pu-O and U-Pu-O
Systems)

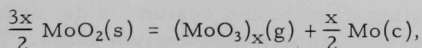
The chemistry of the U-Mo-O system is being investigated to provide a basis for understanding the extensive migration of molybdenum that has been observed in the postirradiation examination of oxide fuels.

*P. M. French et al., "Fuel Characterizations," Oxide Fuel Element Development Quarterly Progress Report, WARD-4135-4 (1971).

The migration of molybdenum during irradiation is believed to be related to the local values of the oxygen potential and the temperature. Furthermore, the migration of volatile molybdenum oxides under the temperature gradient in the fuel will redistribute the oxygen in the fuel matrix; this process would play a major role in oxygen redistribution in high-burnup fuels. In the present investigation, the partial pressures of the gaseous molybdenum oxide species in equilibrium with $\text{UO}_2\text{-MoO}_2$ mixtures are being determined as a function of the O/M ratio and the temperature. A combination of Knudsen effusion and mass spectrometry is being used for these studies.

Preliminary experiments were done to determine the general nature of the interaction of molybdenum oxide with hyper- and hypostoichiometric urania. Samples of MoO_2 , $\text{UO}_{2.08}\text{-10 wt \% MoO}_2$, and $\text{UO}_{1.96}\text{-10 wt \% MoO}_2$ were heated in an iridium-lined Knudsen effusion cell and the vapor species and their relative concentrations estimated by mass spectrometry. In all cases, MoO_2 , MoO_3 , $(\text{MoO}_3)_2$, and $(\text{MoO}_3)_3$ were formed in the gas phase effusing from the Knudsen cell. The total pressure of molybdenum oxide species was greatest over the $\text{UO}_{2.08}\text{-10 wt \% MoO}_2$ mixture and least over the $\text{UO}_{1.96}\text{-10 wt \% MoO}_2$ mixture. For each mixture and pure MoO_2 , the order of decreasing partial pressures was found to be MoO_3 , $(\text{MoO}_3)_2$, MoO_2 , and $(\text{MoO}_3)_3$.

A more detailed study is under way on the interaction of molybdenum oxide with hypostoichiometric urania. In the first experiments in this study, a mixture of $\text{UO}_{1.96}$ and MoO_2 was first equilibrated in a closed Knudsen cell at about 1693°K for 2 hr and the equilibrium vapor composition determined as a function of time at constant temperature. It was found that the partial pressures of the four molybdenum oxide gaseous species decreased slowly to nearly constant values as the effusion proceeded. The partial pressure of gaseous MoO_3 (and its polymers) decreased relatively more rapidly than that of gaseous MoO_2 . The experiment was done by successive additions of 2, 2, and 4 wt % MoO_2 to a sample of $\text{UO}_{1.96}$. The pressure-versus-time behaviors for the three effusion periods were similar, except that after the 4 wt % addition, the partial pressures of the gaseous species remained nearly constant for about 90 min and then decreased to about the same values observed at the end of the two 2 wt % additions. From the weight loss of the samples and the average composition of the vapor, the overall composition of the samples at the end of the effusion stage was estimated. If it is assumed that MoO_3 and its polymers are formed by the disproportionation reactions



then the composition of the oxide phase can be computed. The overall composition of the oxide phase was computed to be $\text{U}_{0.96}\text{Mo}_{0.04}\text{O}_{1.97}$ at the

end of all three effusion steps. X-ray examination of the residue confirmed that metallic molybdenum was present. The lattice constant of the fluorite phase in the residue was slightly smaller than that for stoichiometric urania. From the ratio of the partial pressures of MoO_2 and MoO_3 in the gas phase at the end of the effusion stage and from thermodynamic data,* the oxygen potential ($RT \ln P_{\text{O}_2}$) was estimated to be -81 kcal/mol (at 1693°K). For comparison, the oxygen potential at this temperature over the Mo-MoO_2 system is -71 kcal/mol ,* whereas that over $\text{UO}_{2.0005}$ is about -80 kcal/mol .** These preliminary results suggest a significant effect on the oxygen potential of urania by molybdenum.

- b. U-Pu-O Fuel-Fission-product Interactions. C. E. Crouthamel and I. Johnson, CEN [Last reported: ANL-7783, p. 88, under Phase Diagram Studies of the U-Pu-O System Containing Fission Products (Nonradioactive Isotopes)]

The chemistry of the Pu-U-Cs-O system is under investigation to provide a factual basis for understanding the interaction of fission-product cesium with the $\text{UO}_2\text{-PuO}_2$ fuel matrix under reactor operational conditions. The interaction of cesium with the fuel matrix appears to be important in determining the extent of cladding attack and the magnitude of solid fuel swelling. In the present investigation, the activity of cesium in a mixed $\text{UO}_2\text{-PuO}_2$ matrix will be determined as a function of composition and temperature. The cesium activity is expected to be significantly dependent on the oxygen potential of the system, the cesium content of the solid phases, the nature (structure) of the solid phases, and the temperature.

To gain a rapid insight into the interaction of cesium with a typical fuel oxide, the initial experiments are being conducted using urania as a stand-in for the mixed uranium-plutonium oxide. Samples of the U-Cs-O system have been prepared by heat treatment of mixtures of urania, cesium oxide, and cesium metal in sealed capsules. The phases present in the samples after heat treatment are being determined by X-ray diffraction analysis. The vapor composition over selected samples has been determined as a function of temperature by Knudsen effusion-mass spectrometry.

A series of sample preparation experiments indicated that urania and cesium oxide react when heated at $\sim 720^\circ\text{C}$ to yield cesium uranate (Cs_2UO_4). Depending on the relative amounts of urania and cesium oxide used, the reaction product will also contain either unreacted urania or cesium oxide. Knudsen-effusion, mass-spectrometric experiments have been done with mixtures of cesium uranate and cesium oxide; urania and cesium uranate; and urania, cesium uranate, and cesium oxide. The cesium oxide contained a small amount of cesium peroxide.

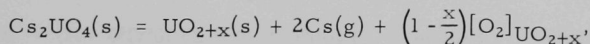
*JANAF Thermodynamic Data, Dow Chemical Company, Midland, Michigan (June 30, 1967).

**K. Hagemark and M. Broli, J. Inorg. Nucl. Chem. 28, 2837 (1966).

When the mixture of cesium uranate and cesium oxide was heated at $\sim 600^\circ\text{C}$ in the Knudsen effusion cell, the rate of weight loss rapidly approached a constant value corresponding to a cesium partial pressure of about 3×10^{-7} atm. After about 20 hr of vaporization, the cesium partial pressure decreased to about 2×10^{-7} atm.

When a mixture of urania and cesium uranate was heated, the rate of weight loss rapidly approached a constant value corresponding to a cesium pressure of 2.6×10^{-8} atm at 585°C .

When a mixture of urania, cesium uranate, and cesium oxide was heated together at $\sim 600^\circ\text{C}$, the rate of weight loss gradually decreased over an 8-hr period. Initially, the rate of weight loss was approximately the same as that observed for the cesium uranate-cesium oxide mixture. The final rate of weight loss was approximately the same as that observed for the mixture of urania and cesium uranate. From these observations it has been tentatively concluded that three different processes are involved. Cesium oxide may vaporize from a liquid oxide phase (the studies were made above the melting point of all cesium oxides) either in the presence of cesium uranate or in the presence of cesium uranate and urania. In the latter case, the cesium oxide melt reacts with the urania concurrently with the vaporization process. Finally, for mixtures of urania and cesium uranate, the vaporization process may be represented by the equation



where the oxygen formed dissolves in the hyperstoichiometric urania present.

The results of these experiments indicate the probable behavior of fission-product cesium in the cooler, unrestructured region of the fuel near the cladding. As the oxygen pressure in this region increases with fuel burnup, there would be a tendency for fission-product cesium to react with the oxide matrix to form cesium uranate rather than cesium oxide. This reaction would maintain a much lower cesium partial pressure in the unrestructured region than would be maintained if all the cesium were gaseous.

C. Fuel Elements

1. Behavior of Reactor Materials (02-086)

- a. Migration of Major Fuel Constituents. R. O. Meyer and D. R. O'Boyle (Last reported: ANL-7825, p. 5.27)

(1) Simplified Method of Calculating Radial Temperature Distribution in Mixed-oxide Fuel. The radial temperature distribution in mixed-oxide fuel rods is needed in many aspects of postirradiation

examination and analysis. To obtain these temperatures, calculations are usually performed numerically* so that the effects of temperature and porosity on the thermal conductivity of the fuel can be included. A method has been developed for an analytical solution to the heat-flow problem that accounts for temperature variations of the thermal conductivity and accounts approximately for porosity variations. This solution is obtained by using simple functions to represent the thermal conductivity over two limited temperature regions.

Several thermal-conductivity functions for mixed-oxide fuels have been reported.** The equation of Biancheria et al., which is the only expression that takes into account the conductivity measurements of Gibby† and van Craeynest and Weilbacher,†† is

$$k(W/cm \cdot ^\circ K) = [3.11 + 0.0272T(^{\circ}K)]^{-1} + 5.39 \times 10^{-13}T^3(^{\circ}K). \quad (1)$$

This expression, sometimes called the FTR design equation, applies to 95% theoretically dense ($U_{0.8}, Pu_{0.2}$) O_2 , which is stoichiometric below $1400^{\circ}C$ but has an oxygen-to-metal ratio of 1.98 above $1400^{\circ}C$.‡ Equation 1 correlates well with recent thermal-conductivity data‡‡ as well as with previous data§ on uranium dioxide. This conductivity function can be approximated quite well over the 500 - $2500^{\circ}C$ range by two simpler functions

$$k(W/cm \cdot ^\circ K) = [8.74 + 0.0213T(^{\circ}K)]^{-1} \quad (\text{Region I: } 500^{\circ}C < T < 1400^{\circ}C); \quad (2)$$

$$k(W/cm \cdot ^\circ K) = 0.0225 \quad (\text{Region II: } 1400^{\circ}C < T < 2500^{\circ}C). \quad (3)$$

These equations are shown graphically in Fig. V.15.

The heat-flow equation in polar coordinates is

$$\frac{\partial^2 T}{\partial r^2} + \frac{1}{r} \frac{\partial T}{\partial r} + \frac{g}{k} = 0, \quad (4)$$

where g in W/cm^3 is the heat-generation rate. Equation 4 can be solved in terms of analytical functions when k is given by either Eq. 2 or 3.

*V. Z. Jankus and R. W. Weeks, LIFE-I, a FORTRAN-IV Computer Code for the Prediction of Fast-reactor Fuel-element Behavior, ANL-7736 (Nov 1970).

**Charles W. Sayles, Trans. Am. Nucl. Soc. 10, 458 (1967); W. E. Baily, E. A. Aitken, R. R. Asamoto, and C. N. Craig, Nucl. Met. 13, 293 (1968); A. Biancheria et al., WARD-4135-1, p. 6 (Sept 1969); H. Kämpf and G. Karsten, Nucl. Appl. and Tech. 9, 288 (1970).

†R. L. Gibby, J. Nucl. Mater. 38, 163 (1971).

††J. C. van Craeynest and J. C. Weilbacher, J. Nucl. Mater. 26, 132 (1968).

‡A. Biancheria, Westinghouse Advanced Reactors Division, private communication (1971).

‡‡J. Hôchel, G. Saur, and H. Borchers, J. Nucl. Mater. 33, 225 (1969); J. B. Ainscough and M. J. Wheeler, Brit. J. Appl. Phys. (Ser. 2) 1, 859 (1968).

§International Atomic Energy Agency, Technical Reports Series No. 59, IAEA, Vienna (1966).

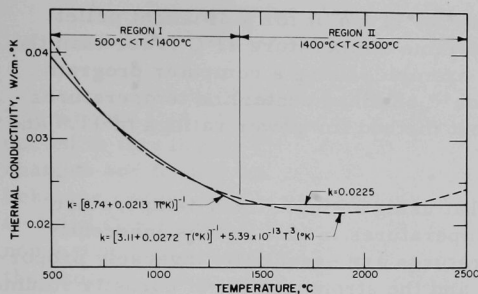


Fig. V.15

Thermal Conductivity of $(U_{0.8}, Pu_{0.2})O_2$, as a Function of Temperature, Approximated over Two Temperature Regions by Simpler Functions. Values apply to 95% theoretically dense material; stoichiometric below 1400°C; and O/M ratio 1.98, above 1400°C. Neg. No. MSD-54981.

As the density of the fuel increases due to restructuring, both the heat-generation rate g and the thermal conductivity k increase so that Eq. 4 becomes less sensitive to porosity than either g or k . Thus, if the heat-generation rate and thermal-conductivity values are adjusted to some average porosity value, variations in porosity will be compensated for in an approximate manner. For fuel in a fast-neutron flux, the heat-generation rate can be taken proportional to the fuel density, whereas the thermal conductivity can be corrected with the Maxwell-Eucken factor $(1 - P)/(1 + \beta P)$, where P is the volume fraction of porosity, and β is a porosity shape factor.* After adjusting g and k to an average porosity value, let G represent the heat-generation rate and let Eqs. 2 and 3 be represented by

$$k = (A + BT)^{-1} \quad (\text{Region I}) \quad (5)$$

and

$$k = K \quad (\text{Region II}), \quad (6)$$

where G , A , B , and K are now constants.

The solutions of Eq. 4 involve Bessel functions and simpler functions. The calculations needed to evaluate integration constants can all be performed by hand; however, the existence of a Bessel-function subroutine in the ANL Program Library has made the use of the computer desirable. A short computer program has been written to evaluate these solutions.

The above method of calculating temperatures has been compared with several more complicated methods using the same thermal-conductivity function, and the results were satisfactory. A modified version of the LIFE code yielded centerline temperatures that were 11°C lower and 14°C higher, respectively, in two examples** at linear power ratings of

*A. Biancheria, Trans. Am. Nucl. Soc. 9, 15 (1966); G. P. Marino, J. Nucl. Mater. 38, 178 (1971).

**R. B. Poepfel, ANL, private communication (1971).

7 and 14 kW/ft. In another example* at 14 kW/ft for a different pellet density, the LIFE code gave a centerline temperature 41°C lower than the present method. In two additional examples using a computer program called MARGE, Marr and Thompson** obtained centerline temperatures 127 and 90°C higher than the present method for power ratings of 11.9 and 17.2 kW/ft, respectively.

It is our opinion that using a single fixed-temperature boundary condition to calculate temperatures in fuel rods is inherently unreliable. The calculated temperatures are essentially inversely proportional to the thermal conductivity, and the strong effects of porosity volume and morphology,† stoichiometry,†† and burnup‡ on thermal conductivity are well recognized. Under these circumstances, an approximate method of calculating temperature that is easy to use and with limitations that are clearly evident has considerable merit.

2. Oxide Fuel Studies (02-005)

- a. Fuel-swelling Studies. L. C. Michels and G. M. Dragel (Last reported: ANL-7798, p. 68)

Full radial examination by fracture-replica electron microscopy of a transverse section from the mixed-oxide portion of NUMEC fuel element C-1 is being conducted. This element was irradiated in EBR-II to a peak burnup of 10.9 at. % at a peak linear power of 14.7 kW/ft. The transverse section being examined was taken from the peak power portion of the element. A preliminary analysis of these results at high burnup provided confirmation of two important observations made in lower-burnup elements (see ANL-7798, p. 68). These are, first, the existence of grain-edge openings in the unrestructured region of the fuel, and second, the existence of inter-linked elongated bubbles on the grain boundaries and along grain edges in the columnar-grain-growth region of the fuel. From these preliminary observations, it has not been possible to determine if a burnup dependence exists for these phenomena. A significant change in the morphology of the grain-edge openings and the fission-gas bubbles might help to explain the increase found in fission-gas release with burnup.

*M. Katsuragawa, ANL, private communication (1971).

**W. W. Marr and D. H. Thompson, Trans. Am. Nucl. Soc. 14, 150 (1971).

†H. Kämpf and G. Karsten, Nucl. Appl. and Tech. 9, 288 (1970); A. Biancheria, Trans. Am. Nucl. Soc. 9, 15 (1966); G. P. Marino, J. Nucl. Mater. 38, 178 (1971).

††J. C. van Craeynest and J. C. Weilbacher, J. Nucl. Mater. 26, 132 (1968); R. L. Gibby, BNWL-927 (Jan 1969).

‡H. Kleykamp, Karlsruhe (Germany) Report EURFNR-817 (July 1970).

- b. Fuel-element Performance. L. A. Neimark, J. E. Ayer, and J. D. B. Lambert (Last reported: ANL-7737, p. 116)

(1) Groups O-4 and O-5, Cladding Deformation Mechanisms.

The Groups O-4 and O-5 series of the EBR-II experiments are being conducted to investigate the mechanisms that cause fuel-element dimensional changes and to test and improve models now used in the ANL fuel-element behavior codes. Of the 34 elements required for the first loading of the O-4 and O-5 irradiations, 25 elements are complete and are undergoing nondestructive examination. Of the nine elements remaining, four are in the process of final assembly, the fuel for four additional elements is being heat-treated to yield an oxygen-to-metal (O/M) ratio of 1.94, and the last element, containing solgel fuel, will be loaded in the near future.

The completed elements have been individually radiographed alongside a length standard. This length standard will accompany the elements through their interim and final postirradiation examinations. Diameter scans of each element at 0, 45, 90, and 180° orientations are being generated with a profilometer that is identical to the one in-cell in the Materials Science Division Hot Cells. A lapped diameter standard is being used for instrument calibration. This standard, which is screwed into the top end of each element in turn, will also be used for postirradiation profilometry. Overall length measurements will be obtained with a jig, which will be similarly used in-cell. In this way, quality assurance of element measurements before and after irradiation will be maintained. Similar procedures will be applied to measurements on the capsules.

Reduction of the O/M ratio of the fuel for four of the elements is being performed by N. Javed with apparatus that has been described previously (ANL-7783, p. 73). The experimental technique involves the passage of commercial-grade hydrogen over stoichiometric fuel held at ~1500°C for 16-20 hr. The first firing of 75 g of (U,Pu)O₂ fuel successfully reduced the O/M value from 1.98 (nominal) to 1.938 (measured gravimetrically by equilibration in CO/CO₂ at ~850°C). Reproducibility in the final O/M value appears to be ±0.005.

The safety of the fuel elements at the beginning of life during postulated accident conditions in EBR-II* is being evaluated by using the THTB transient heat-transfer code.** Temperatures that are achieved during flow-coastdown and inadvertent reactivity insertion have been determined for the peak-rated element in the Group O-4 subassembly. The temperature-time plots are given in Figs. V.16 and V.17. During flow-coastdown (Fig. V.16), the maximum cladding midwall and coolant temperatures are 720 and 680°C, respectively, and these occur some 10-12 sec after

*Guide for Irradiation Experiments in EBR-II, Rev. 4.

**THTB(GE)--Three Dimensional Transient Heat Transfer, Program Library 2209/RE 322, Applied Mathematics Division, ANL (Aug 1966).

the coolant flow starts to decrease. Because of the low diffusivity of the $(U,Pu)O_2$ and the fuel-cladding interface, temperatures in the fuel decrease from time zero. A second temperature surge of smaller magnitude occurs at ~60 sec. At neither time will the element be unsafe due to stresses generated by increased temperature.

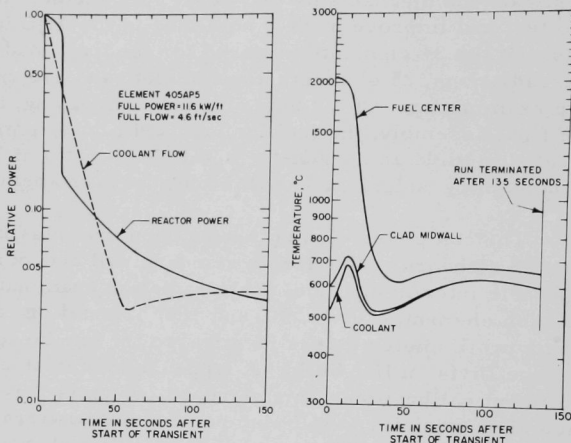


Fig. V.16. Calculated Maximum Temperatures Achieved in the Peak-rated Element in Group O-4 during a Postulated Flow-coastdown in EBR-II (power and flow conditions shown at left). Neg. No. MSD-161264.

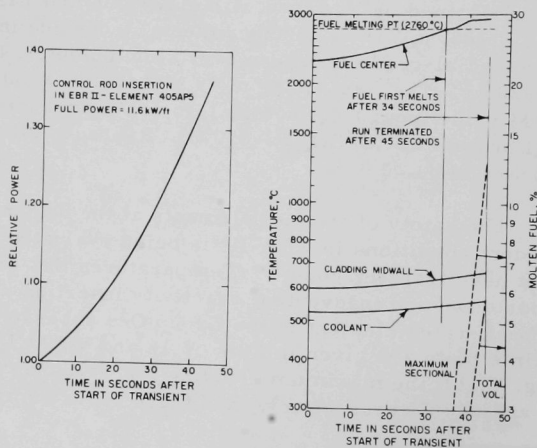


Fig. V.17. Calculated Maximum Temperatures Achieved in Peak-rated Element in Group O-4 during Postulated Reactivity Insertion in EBR-II (shown at left). Neg. No. MSD-161265.

During the postulated reactor power ramp (Fig. V.17), the $(U,Pu)O_2$ is first seen to undergo center melting (slightly below the center plane of the element) 34 sec after the start of the transients, when the reactor power is ~125% of full power. After 45 sec, more extensive fuel center melting has occurred, although the amount is still insufficient to supply a hydrostatic loading to the cladding. (Available voidage in the fuel will probably accommodate the 10% volume increase on melting.) Also, at this time the capsule and coolant temperatures are some 150-200°C below their boiling points. As remedial action is taken, approximately 10-12 sec after the start of the power transient, the fuel elements should be safe. The calculations are being repeated for the peak-rated element in the Group O-5 subassembly, which will operate at a peak power rating of 16 kW/ft.

(2) High-burnup NUMEC Elements. J. D. B. Lambert and W. F. Murphy (Last reported: ANL-7833, p. 5.15). Twelve mixed-oxide fuel elements of the NUMEC Group C have been removed from EBR-II (Subassembly X080) for interim examination at a peak burnup of 13 at. % (9.8×10^{22} nvt, total). Neutron radiography of the encapsulated elements has revealed no obvious indications of element failures. Elements C-10 and C-13 will be destructively examined at ANL-Illinois. The remaining ten elements, plus four other previously irradiated NUMEC elements (C-7, C-8, B-6, and B-7), will be assembled into a reconstituted Subassembly X080A for continued irradiation to a peak burnup of 16 at. %.

PUBLICATIONS

Neutron Radiography for Nondestructive Testing

Harold Berger

Electronics World 86(2), 40-44 (Aug 1971)

Surface Diffusion, Surface Free Energy, and Grain-Boundary Free Energy of Uranium Dioxide

P. S. Maiya

J. Nucl. Mater. 40(1), 57-65 (July 1971)

Adiabatic Elastic Constants of Uranium Monocarbide

J. L. Routbort

J. Nucl. Mater. 40(1), 17-26 (July 1971)

High-Temperature Thermodynamic Properties of Hypo- and Hyper-stoichiometric Uranium Carbides

M. Tetenbaum and P. D. Hunt

J. Nucl. Mater. 40(1), 104-112 (July 1971)

VI. FUEL CYCLE

A. Molten-metal Decladding of LMFBR Fuels.

R. D. Pierce (02-173)

A liquid-metal decladding procedure is being developed as the head-end step for the aqueous processing of fast-breeder-reactor fuels. In this process, stainless steel cladding is dissolved in liquid zinc (at 800°C), the zinc-steel solution is pressure-transferred from the dissolution vessel to cylinders where the excess zinc is evaporated for recycling, and the cylinders containing the waste steel are sealed for burial; the fuel oxide remains in the dissolution vessel and is reduced to metal by heating in a Zn-Mg-Ca reduction solvent; the metal solution is transferred to an evaporator, where the solvent metals are removed, and the residual U-Pu alloy is cast into ingots, which are fed to the nitric acid dissolution step. This process is also applicable to the removal of Zircaloy cladding.

If a high-zinc reduction alloy is used, both uranium and plutonium are dissolved in the alloy upon reduction; if a low-zinc reduction alloy is used, plutonium but very little uranium is dissolved. Successful reductions of UO_2 pellets [a stand-in for $(\text{U,Pu})\text{O}_2$ pellets] have been made with each alloy in combination with a CaCl_2 - CaF_2 salt.

1. Engineering Concepts, Analysis, and Evaluation (Last reported: ANL-7753, p. 135)

The Fuel Cycle Branch of RDT has asked ANL to evaluate melting of the stainless steel components of a subassembly (1500°C) as a decladding method alternative to the zinc head-end process described above. Procedures considered for separating the stainless steel from the pellets are as follows:

1. Melting the steel and allowing it to solidify around the oxide, then separating the components by acid dissolution of the oxide only.
2. Heating the fuel subassembly in a vertical crucible that has holes in its base to allow drainage of the liquid stainless steel from UO_2 pellets and fines (ANL-7765, p. 79).
3. Melting the cladding while the fuel subassembly rests on a crucible wall sloped downward at a small angle to promote flow of molten metal away from the pellets (ANL-7776, p. 91).
4. Melting the stainless steel in an upright crucible, then tipping the crucible to pour off the steel, leaving the oxide in the crucible (currently being investigated; see below).

5. Lowering the fuel assembly slowly into a furnace so that as the steel melts, the mixture of steel and fuel falls onto a cooled surface (ANL-7783, p. 83). The steel forms platelets that may be separable from the fuel.

Investigation of these procedures on a small scale led to a conceptual design based on alternative 4 above. A tilt-pour melt-decladding furnace (see Fig. VI.1), installed in a process cell, would be capable of handling 1 metric ton of spent nuclear fuel per 8-hr day. In this concept, two vertically suspended fuel subassemblies in a cooled transport chamber are brought to the top of the furnace. The transport chamber is fastened into position and the lock is opened to allow the subassemblies to be lowered into the magnesia-lined graphite susceptor, which is inductively heated. The rate of lowering is controlled to correspond to the rate at which the stainless steel melts. The furnace temperature is between 1550 and 1600°C. After the meltdown period (about 1 hr), the crucible is tilted to about 10° below horizontal and the molten steel is poured into a waste-steel transport mold that has the capacity to contain the steel from eight subassemblies (~1.5 metric tons). At the end of the day, the transport mold is removed from the furnace through a lock. After the steel is poured, the crucible assembly is tilted in the opposite direction 45° past horizontal to dump the UO_2 - PuO_2 pellets into a chute leading to a lock. The pellets are then dumped into a transport vessel, moved to a cooled storage area, and subsequently fed to the dissolver (i.e., to the nitric acid dissolution step).

An argon closed-cycle atmosphere is maintained in the furnace at slightly below process cell pressure during the melt-decladding operation. Because fission-product gases are released during the operation, the furnace pressure tends to increase. The increase is limited by withdrawing some of the gas through a reactive bed to remove iodides and iodine and then compressing it into intermediate storage tanks. The waste gas is eventually compressed into cylinders for permanent storage.

An advantage of melt decladding as a potential head-end step is its basic simplicity; however, some development work would have to be done on the control of both volatile and nonvolatile wastes to make the technique feasible.

2. Engineering Development (Last reported: ANL-7833, p. 6.1)

a. Melt Decladding

One concept for melt decladding of LMFBR fuel (alternative 5 in Sect. 1 above) involves lowering a vertically suspended subassembly into a heated zone, permitting the shroud and cladding metal to melt and drip off and the oxide fuel to fall (ANL-7783, p. 83). The fuel and steel would

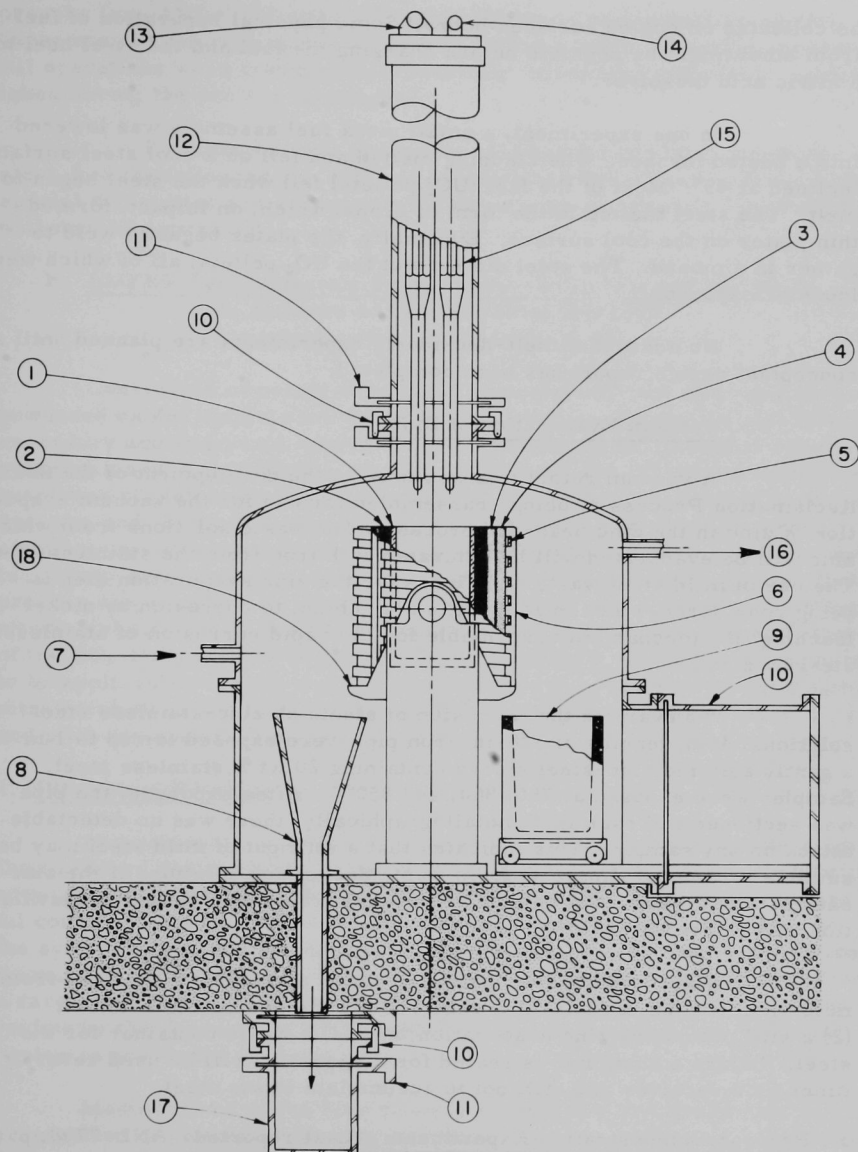


Fig. VI.1. Tilt-Pour Melt-decladding Furnace. 1. MgO Liner of Crucible. 2. Graphite Susceptor. 3. SiC Insulation. 4. Zirconia Insulation. 5. Induction Coils. 6. Coil Support. 7. Argon Supply. 8. $\text{UO}_2\text{-PuO}_2$ Fuel Chute. 9. Waste Steel Mold. 10. Locks. 11. Lock Gates. 12. Transfer Chamber. 13. Elevating Mechanism for Fuel Subassemblies. 14. Transfer-chamber Cooling-gas Inlet. 15. Fuel Subassemblies. 16. Argon + Fission-product Gas to Recycle and Storage. 17. Pellet Transport Vessel. 18. Tilt-Pour Mechanism for Crucible.

be collected on cooled surfaces below. Some physical separation of fuel from steel might be possible before charging the fuel and the steel heel to a nitric acid dissolver.

In one experiment, a small mock fuel assembly was lowered into a heated furnace. The cladding melted and fell on a cool steel surface inclined at 45° . Most of the fuel (UO_2 pellets) fell when the steel began to melt. The steel melted in the form of drops, which, on impact, formed thin plates on the cool surface. Eventually, the plates began to weld together in a mound. The steel did not wet the UO_2 pellets, all of which were loose or exposed.

No additional melt-decladding experiments are planned until a conceptual design report has been completed.

b. Vacuum Evaporation of Zinc

A vacuum retort that was used in the development of the Skull Reclamation Process is being reassembled for use for the vacuum evaporation of zinc in the zinc head-end process. The waste solutions from which zinc will be evaporated will be saturated with iron from the stainless steel. The use of mild steel waste containers for the zinc evaporation step is being considered, since mild steel is not subject to corrosion by nickel leaching (the mechanism responsible for the rapid corrosion of stainless steel by zinc).

To evaluate the corrosion of steels by zinc-stainless steel solutions, 4-in. lengths of $3/8$ -in. iron pipe were exposed for up to 1 hr to a gently agitated zinc-steel slurry containing 20 wt % stainless steel. Samples were exposed at 750, 800, and 850°C . After exposure, the pipe was sectioned and examined metallographically; there was no detectable attack on any sample. This indicates that a still pot of mild steel may be suitable for evaporating zinc from waste decladding solutions if the zinc is saturated with iron. The effects of thermal gradients inherent in distillation will be evaluated.

Experiments are planned in which a crucible fabricated from mild steel will be used as (1) a receiver for the decladding solution, (2) a still pot during zinc evaporation, and (3) a waste container for the steel. Before a container is sealed for disposal, it will be used several times as a receiver and still pot to accumulate waste steel.

3. Process Demonstration Experiments (Last reported: ANL-7798, p. 80)

a. Irradiated-fuel Experiments

Experimental apparatus has been installed in the Chemical Engineering Division's Senior Cave to investigate the liquid-zinc head-end

process (see ANL-7798) with ~100-g quantities of highly irradiated fuel. An experimental run with unirradiated UO_2 fuel was made using this apparatus. All operations were completed successfully. Chemical analyses of samples taken during the run are incomplete.

The next run will involve the dissolution of highly irradiated steel, and the following run will use unirradiated PuO_2 -bearing fuel. If no special difficulties are encountered in these runs, irradiated UO_2 - PuO_2 fuel will then be processed.

B. LMFBR Fuel Materials Preparation--U/Pu Nitrates to Oxides.

A. A. Jonke and N. M. Levitz (02-157;

last reported: ANL-7798, p. 81)

Conversion of uranyl nitrate and plutonium nitrate solutions to powdered oxides suitable for the fabrication of fuel shapes (pellets) is a necessary and important step in the nuclear-fuel cycle. Incentives for developing a new high-capacity, continuous process are (1) the increased quantities of plutonium needed for LMFBR and plutonium-recycle fuel systems and (2) the growing concern over shipping plutonium as nitrate solution. A conversion process under investigation based on fluidized-bed technology shows a high potential for meeting process requirements. Basic process steps include fluidized-bed denitration of uranyl nitrate-plutonium nitrate solutions to UO_3 - PuO_2 powder, followed by fluidized-bed reduction of the UO_3 - PuO_2 with hydrogen to UO_2 - PuO_2 powder. The process appears to be applicable over the entire concentration range of uranium-plutonium nitrate solutions and to plutonium nitrate alone. An integrated laboratory and pilot engineering program is in progress.

1. Pilot-plant Program

As previously reported, a pilot-scale facility containing a 4-in.-dia fluidized-bed denitration reactor was constructed and tested for operability with uranyl nitrate feed solution (ANL-7742, pp. 120-121). After successful completion of this phase of the program, modifications were made to the system to permit safe operations with plutonium-bearing feed solutions. Because several kilograms of plutonium will be handled in these operations, a careful analysis of nuclear criticality aspects is required. Criticality review by the appropriate ANL authorities has been completed, and AEC review is now under way.

Modifications of the feed makeup system to a design suitable for preparation of plutonium-bearing solutions has been completed. The feed makeup system comprises a 4-in.-dia by 36-in.-tall dissolver, a 16-in.-dia by 25-in.-tall feed storage vessel,* and a 3-in.-dia by 40-in.-tall feed tank.

*Vessels in the glovebox with diameters greater than 4 in. are filled with boron-glass Raschig rings as a fixed nuclear poison.

The total quantity of plutonium is minimized by recycling product back to the feed system. Small batches of oxide product from the denitrator are redissolved in nitric acid, and the solutions from several batches are blended in the large feed-storage vessel, where the composition (e.g., acidity and actinide concentration) is adjusted. Quantities of the feed solution are transferred to the feed tank as needed during a run for metering into the 4-in.-dia fluidized-bed denitrator (see ANL-7726, p. 139).

In the current period, a shakedown run of the system was made to test the procedures that will be used in handling (U,Pu) nitrates and oxides. Eight 3.2-kg batches of UO_3 were dissolved in nitric acid to prepare ~50 liters of 1.9M uranyl nitrate feed solution containing 1.4M excess acid. Dissolution of each batch of UO_3 in 5 liters of 6.0M HNO_3 required 1-2 hr. The feed-makeup system functioned satisfactorily.

A 10.5-hr denitration run, U-7, was successfully carried out using glovebox techniques to simulate plutonium handling. The starting bed was 10 kg of UO_3 powder, and the bed temperature was 300°C. Uranyl nitrate solution was initially fed at 65 ml/min, then for ~7 hr at 95 ml/min. The latter is equivalent to a UO_3 production rate of 80 lb/(hr)(sq ft). The inlet fluidizing-gas rate corresponded to a superficial linear gas velocity of ~0.9 ft/sec at column conditions (300°C, ~5 psig). The product was collected continuously as it overflowed from the bed through a nominally 1/4-in. pipe sidearm mounted at the 12-in. level; the bed level thus remained fairly uniform.

The run was evaluated largely on the operability of the unit, which was good. Sieve analyses of hourly samples of UO_3 product showed no gross trends in particle-size distribution. About 7% of the 10-kg final bed consisted of coarse material (+10 mesh) formed during the run.

A duplicate run with uranyl nitrate feed is planned, to gain additional operating experience. Final mechanical work on the glovebox proper (e.g., sealing of glovebox windows and a glovebox leak-check) is in progress.

C. LMFBR Fuel Fabrication--Analyses and Continuous Processing.

A. A. Jonke and M. J. Steindler (02-158)

A program is under way to develop rapid, precise, and accurate in-line analytical methods applicable to the fabrication of LMFBR oxide fuels. Such methods are expected to lead to decreased costs and automated procedures. The starting criteria selected for evaluation of analytical requirements are the specifications of preirradiation fuel properties (and the associated precisions) for the Fast Flux Test Facility (FFTF) project. The fuel properties, specifications, precisions, and acceptable methods of measurement for FFTF were discussed in ANL-7735, p. 59.

The fuel for the first commercial LMFBR is expected to be uranium-plutonium oxide. Since the plutonium/uranium (Pu/U) ratio and the oxygen/metal (O/M) ratio will have to be evaluated in every conceivable fabrication procedure, these have been selected for initial study.

1. Plutonium/Uranium Ratio in Fuel (Last reported: ANL-7833, p. 6.4)

The originally defined specification* for fuel in the core zone is that the plutonium constitutes $20.0 \pm 0.1\%$ of the actinide content, which corresponds to a relative standard deviation of 0.5%

X-ray fluorescence (XRF) analysis is being evaluated as a nondestructive, in-line analytical method for determining Pu/U in fuel materials at high analysis rates. In XRF, the characteristic radiation of the element is excited by incident X rays of energy higher than the absorption edge. Instrumental choices, sample presentation procedures, and material effects are being evaluated. To attain the desired relative precision in the analysis of solid oxide in the form of powder or pellets, effects on the fluorescence signal of properties of the solid, i.e., high absorption coefficients, enhancement (secondary fluorescence), crystallite size, bulk density, etc., must be proven insignificant or predictably measurable.

$\text{ThO}_2\text{-UO}_2$ is being used as a stand-in for $\text{UO}_2\text{-PuO}_2$ for initial investigations, since experiments with plutonium would have to be done in a glovebox, entailing complications and delays. This substitution is practical because of the identical relationship of the atomic numbers and thus of the relevant properties** for each pair of elements.

The XRF method, using the La spectra, has been shown to be free of interferences by any other elements that can reasonably be expected to be present in a fuel sample.[†] Consideration of a desirable sampling procedure to accommodate a high production rate and extension of the limitations imposed by counting statistics led to the use of wider collimating slits to decrease the analysis time per sample to less than 1 min.** With a slit width of 20 mils, adequate resolution of the pairs of peaks to be counted has been demonstrated. Improvements in the sample presentation procedure increased the counting rate and decreased the background rate.^{††} The counting equipment has been calibrated for high count rates to account for dead time.[†]

*D. S. Webster et al., Chemical Engineering Division Fuel Cycle Technology Quarterly Report, April, May, June 1970, pp. 60, 63-64, ANL-7735 (July 1970).

**D. S. Webster et al., Chemical Engineering Division Fuel Cycle Technology Quarterly Report, July, August, September 1970, pp. 45-50, ANL-7755 (Oct 1970).

†D. S. Webster et al., Chemical Engineering Division Fuel Cycle Technology Quarterly Report, January, February, March 1971, pp. 36-41, ANL-7799 (in press).

††D. S. Webster et al., Chemical Engineering Division Fuel Cycle Technology Quarterly Report, October, November, December 1970, pp. 30-31, ANL-7767 (Jan 1971).

a. Analysis of ThO₂-UO₂ Pellets

Additional work has been done to determine whether the relative standard deviation of $\pm 0.5\%$ desired for plutonium analysis can be achieved in the analysis of mixed-oxide fuel materials. In ANL-7833, relative standard deviations of 0.2-0.6% had been measured for mixed oxide pellets. Current work was performed to determine whether, at the 95% confidence level, the variability of measurements of different pellets of the same nominal composition differed significantly from the variability of measurements on the same pellet.

Four pellets, each of ThO₂-10 wt % UO₂, ThO₂-20 wt % UO₂, and ThO₂-30 wt % UO₂, were prepared from mixed powders. Four UO₂ pellets also were prepared from pure UO₂ powder. The pellets were sintered in a 6% H₂-He atmosphere at 1750°C for 4 hr, and the flat surfaces were polished with 600-grit paper.

To determine the functional reproducibility of the XRF measurements on pellets, five measurements were performed on each of the four pellets of each composition. Each measured count rate was an average of three counts of ~200,000 each. The relative standard deviation for the counting statistics ranged from 0.09 to 0.13%. Each count rate was corrected for dead time.

An analysis of variance* was performed in which it was assumed that the errors of the method and counting statistics are independent and that the variances are additive; this allowed the relative standard deviation (RSD) of the method to be calculated from the variance of the measurements. Table VI.1 presents the RSD's for the measurements, for the counting statistics, for the variability between pellets, and for the errors of the method, derived from both uranium and thorium count rates.

As expected, for the pure urania pellets, the variability between pellets is not statistically different from the variability within pellets. The RSD for the method applied to pure UO₂ pellets, considering counting statistics and measurements, is 0.11%. For the 70% ThO₂-30% UO₂ pellets, the variability in thorium analysis between pellets is not statistically different from that within pellets, but in the uranium analysis, the variability between pellets is significant.

For the 80% ThO₂-20% UO₂ and 90% ThO₂-10% UO₂ pellets, the RSD for measurements for both UO₂ and ThO₂ leads to a range of RSD of the method of 0.24-0.31%. The 95% confidence limits of the RSD can be estimated by using the appropriate degrees of freedom in reference tables.**

*O. L. Davies (ed.), Statistical Methods in Research and Production, 3rd Ed. Hafner Publishing Co., New York (1961).

**O. L. Davies, op. cit., p. 107.

At the 95% confidence level, the upper limit of the RSD of measurements is 0.48%. Thus, the XRF method has been demonstrated on pellets to achieve the goal of 0.5% RSD at the 95% confidence level.

TABLE VI.1. Relative Standard Deviations for XRF Analysis of Fired $\text{ThO}_2\text{-UO}_2$ Pellets

Comp. wt %		Relative Standard Deviations (%) for			
ThO_2	UO_2	Measurement ^a	Count ^b	Method ^c	Pellet ^d
<u>Uranium</u>					
0	100	0.14	0.086	0.11	e
70	30	0.15	0.11	0.10	0.62
80	20	0.34	0.13	0.31	1.84
90	10	0.33	0.13	0.30	0.87
<u>Thorium</u>					
70	30	0.27	0.11	0.24	e
80	20	0.27	0.10	0.24	1.12
90	10	0.26	0.099	0.24	0.60

^aRSD derived from five measurements on same pellet.

^bRSD derived from average of three counts corrected for dead time.

^cRSD derived from square root of the difference of the squares of the RSD of the measurement and the RSD of the count.

^dRSD for four different pellets of same nominal composition.

^eNull hypothesis (F test) indicates that there was no significant difference between pellets.

The range of RSD between pellets is 0.60-1.84%, indicating variation in excess of that attributable to the method. The excess variability may be due to mixing, sampling, or material properties of mixtures.

b. Analysis of $\text{ThO}_2\text{-UO}_2$ Mixed Powder

Five measurements of three samples of 70% ThO_2 -30% UO_2 powder were subjected to an analysis of variance similar to that for pellets. The powder mixtures were prepared from pure ThO_2 and from UO_2 that had been reduced from NBS U_3O_8 . Three sample cups were loaded with each powder and were counted sequentially.

The RSD's for the measurements were 0.29% for thorium and 0.21% for uranium, which lead to RSD's for the method of 0.27 and 0.17%, respectively. The RSD's at the 95% confidence level are again shown to be below 0.5%.

The thorium analysis showed no significant variability between samples; the uranium analysis showed an RSD of 3.1%. This greater variability between samples of powder (3.1%) than between pellets (0.62%) of the same nominal composition suggests there is a material effect in powder that is greater than in pellets. Studies of the effects of particle size and bulk density on the XRF signal are expected to identify the limiting precision of the method applied to powder samples.

c. Conclusions

The adequately low variability of the method indicates that XRF has the potential to achieve better than 0.5% RSD at the 95% confidence level. The larger variability between samples of powder and pellets compared with the low variability of the method indicates that a problem exists due to mixing, sampling, or material properties. By study of particle-size and bulk-density effects on the XRF signal using pure materials and mixtures, evaluation of the precision obtainable for pellet and powder should be possible.

2. Oxygen Content of Fuel (Last reported: ANL-7688, p. 214)

The initial ratio of oxygen to metal (O/M) in the charged fuel affects compatibility of fuel with cladding during irradiation, as well as thermal conductivity. The probable desired range of values for the O/M ratio is 1.95-1.99. Earlier, data from ANL-7735 (see footnote on p. 6.7), p. 71, were used in calculating the following correlation between the lattice parameter and O/M ratio for (U,Pu)O₂ of known Pu/(Pu+U) ratio (ANL-7688, p. 214):

$$a_0 = 6.1127 - 0.534 (\text{Pu}) - 0.321 (\text{O/M}) + 0.229 (\text{Pu})(\text{O/M}), \quad (1)$$

where a_0 is the lattice parameter, (Pu) is the plutonium atom fraction, and (O/M) is the oxygen-to-metal ratio. With this equation, the O/M ratio of stoichiometric oxide can be determined from its lattice parameter when the Pu/(Pu+U) ratio is known.

Recently, data were collected by Martin* on the relationship between lattice parameter and O/M ratio for U_{0.8}Pu_{0.2}O_{2±x}. Martin's data were plotted, and the slope of the curve was observed to be closer to the slope for Gibby's data** than to that for Markin and Street.† The intercept 5.4530 Å for stoichiometric oxide (O/M = 2.0) is lower than the 5.4555 Å value predicted by the Vegard relationship (ANL-7688, p. 214) for pure UO₂-20% PuO₂.

To compare Martin's data with the correlation (Eq. 1), O/M ratios were calculated from Martin's lattice parameters, and lattice parameters were calculated from his measured O/M ratios (see Table VI.2). The deviations of the calculated O/M ratios from the measured ratios ranged from 0.0006 to 0.016 unit, with an RSD of 0.49%. The deviations of the calculated a_0 values from the measured values ranged from 0.0002 to 0.0044 Å, with an RSD of 0.049%.

*A. E. Martin, Argonne National Laboratory, private communication (May 1971).

**R. L. Gibby, The Effect of Oxygen Stoichiometry on the Thermal Diffusivity and Conductivity of U_{0.75}Pu_{0.25}O_{2-x}, BNWL-927 (1969).

†T. L. Markin and R. S. Street, J. Inorg. Nucl. Chem. **29**, 2265-2280 (1967).

TABLE VI.2. Comparisons of Recent O/M Data^a for
 UO_2 -20% PuO_2 to Lattice Parameter Correlation^b

Calc. a_o	Meas. a_o	Meas. O/M	Calc. O/M
5.4808	5.4819	1.908	1.9041
5.4761	5.479	1.925	1.9146
5.4715	5.4713	1.942	1.9426
5.4594	5.4749	1.986	2.0022
5.4572	5.4551	1.994	2.0015
5.4572	5.454	1.994	2.0055
$\sigma_{a_o} = 0.049\%$		$\sigma_{\text{O/M}} = 0.49\%$	

^a A. E. Martin, Argonne National Laboratory, private communication (May 1971).

^b D. S. Webster *et al.*, Chemical Engineering Division Fuel Cycle Technology Quarterly Report, April, May, June 1970, pp. 71-80, ANL-7735 (July 1970).

Martin's data conform reasonably well to the earlier correlation, supporting the concept that nondestructive X-ray diffraction may be an adequate measure of O/M ratio.

VII. REACTOR PHYSICS

A. ZPR Fast Critical Experiments1. Fast Critical Facilities; Experiments and Evaluation--Illinois (02-179)a. Clean Critical Experiments. R. A. Lewis (Last reported: ANL-7833, p. 7.1)

(1) Small Sample Reactivity Worths and ^{238}U Doppler Effect Measurements at the Center of the Voided High-240 Plutonium Core (E. M. Bohn, J. E. Marshall, and J. F. Meyer). The High-240 Plutonium (H-240) zone (see ANL-7833) was constructed in ZPR-6 Assembly 7 by replacing regular plutonium fuel containing 12 wt % ^{240}Pu with plutonium fuel containing 27 wt % ^{240}Pu . Regular fuel was replaced with H-240 fuel along the entire height of the core in a central region out to a radius of 24.3 cm. The sodium-voided High-240 Plutonium (VH-240) zone was constructed by removing sodium from the H-240 zone along the entire height of the core in a central region out to a radius of 19 cm. Radial and axial cross sections of Assembly 7 with the VH-240 zone are shown in Figs. VII.1 and VII.2.

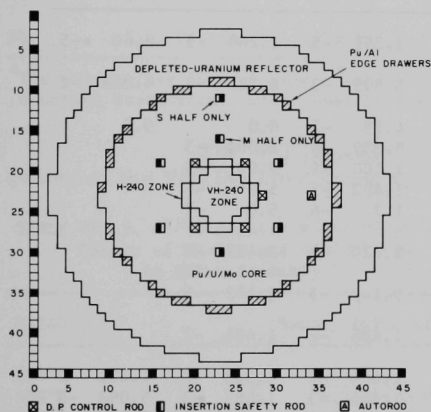


Fig. VII.1. Radial Cross Section of Assembly 7, Showing the High-240 Plutonium (H-240) and Sodium-voided High-240 Plutonium (VH-240) Zones.

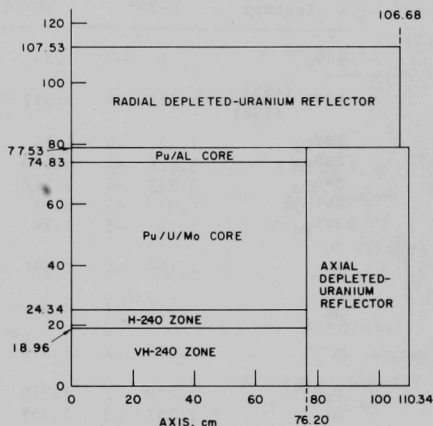
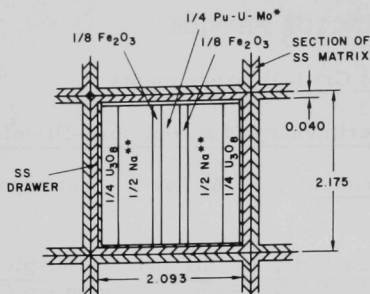


Fig. VII.2. Axial Cross Section of ZPR-6 Assembly 7, Showing the High-240 (H-240) Plutonium and Sodium-voided High-240 Plutonium (VH-240) Zones.

The removal of sodium from the central region was accomplished by replacing two columns of 1/2-in.-thick sodium-filled stainless steel cans with empty stainless steel cans. The unit-cell drawer loadings for Assembly 7, including the VH-240 region, are shown in Fig. VII.3. The atom concentrations in each region of the assembly are given in Table VII.1.



*ZPPR METAL FUEL

11-1/2 w/o ^{240}Pu -NORMAL CORE

27 w/o ^{240}Pu -HIGH 240 ZONE (H-240 ZONE)

**SS CANS FILLED WITH SODIUM IN NORMAL CORE AND H-240 ZONE, EMPTY SS CANS IN VH-240 ZONE.

ALL DIMENSIONS
IN INCHES

Fig. VII.3

The Unit-cell Drawer Loadings
for ZPR-6 Assembly 7

TABLE VII.1. Homogeneous Compositions of Assembly 7 Regions

Isotope	Atoms/cc $\times 10^{-24}$ for each Region							
	H-240		VH-240		Pu/U/Mo Core		Pu/Al Core	
^{235}U	1.25	-5	1.25	-5	1.251	-5	1.260	-5
^{238}U (+ 234 + 236)	5.592	-3	5.592	-3	5.805	-3	5.723	-3
^{238}Pu	1.14	-6	1.14	-6	4.18	-7	0.0	0.0
^{239}Pu	8.378	-4	8.378	-4	8.889	-4	1.064	-3
^{240}Pu	3.217	-4	3.217	-4	1.180	-4	5.00	-5
$^{241}\text{Pu}^a$	6.01	-5	6.01	-5	1.492	-5	5.0	-6
^{242}Pu	1.74	-5	1.74	-5	1.7	-6	5.0	-7
Mo	2.196	-4	2.196	-4	2.270	-4	2.427	-4
Na	9.294	-3	0.0		9.142	-3	9.142	-3
O	1.398	-2	1.398	-2	1.486	-2	1.486	-2
$\text{Fe}^+(b)$	1.278	-2	1.279	-2	1.358	-2	1.343	-2
Ni	1.357	-3	1.357	-3	1.345	-3	1.483	-3
Cr	2.710	-3	2.711	-3	2.705	-3	2.678	-3
Mn	2.31	-4	2.30	-4	1.97	-4	-	8.57
Al	0.0		0.0		0.0		1.01	-4

$^{241}\text{Pu} \rightarrow ^{241}\text{Am}$ decay corrected to January 1, 1971.

$^b\text{Fe}^+$ is Fe plus all 304 SS constituents other than Ni, Cr, or Mn.

The reactivity worths of several small samples were measured at the center of the VH-240 zone. (The experimental technique has been described in ANL-7798.) The results are given in Table VII.2. Compared to similar measurements in the H-240 zone (see ANL-7833), the

worths of all materials except the scattering materials (stainless steel and sodium) are less in the VH-240 zone.

TABLE VII.2. Small-sample Reactivity Worths Measured at Center of Voided High-240 Plutonium (VH-240) Zone in ZPR-6 Assembly 7

Sample	Composition by Weight Percent	Weight, g	Specific Worth, ^a Ih/kg
MB-10	97.8 ²³⁹ Pu, 1.0 ²⁴⁰ Pu, 1.2 Al	9.956	167.1 ± 0.8
MB-11	(same as MB-10)	21.409	168.4 ± 0.4
Pu-11	85.4 ²³⁹ Pu, 11.0 ²⁴⁰ Pu, 2.6 ²⁴¹ Pu, 1.0 Al	15.123	152.5 ± 0.6
Pu-23	45.3 ²³⁹ Pu, 41.2 ²⁴⁰ Pu, 11.2 ²⁴¹ Pu, 2.3 Al	13.923	104.7 ± 0.4
²³⁵ U	93.2 ²³⁵ U, 6.8 ²³⁸ U	3.084	119.8 ± 2.1
²³⁸ U	99.8 ²³⁸ U, 0.2 ²³⁵ U	25.988	-8.88 ± 0.25
Na	100 ²³ Na	17.044	-7.58 ± 0.37
B (nat.)	19.9 ¹⁰ B, 80.1 ¹¹ B	0.555	-530 ± 12
Ta	100 ¹⁸¹ Ta	5.772	-70.1 ± 1.2
SS	71.5 Fe, 9.5 Ni, 18.5 Cr, 1.5 Mn	43.818	-5.60 ± 0.11

^aThe uncertainty in each measurement includes only the uncertainty due to counting statistics. Other sources are small.

The ²³⁸U Doppler reactivity worth was measured at the center of the VH-240 zone using a natural UO₂, freely expanding Doppler

TABLE VII.3. ²³⁸U Doppler Worth Measured at Center of VH-240 and H-240 Zones in ZPR-6 Assembly 7

H-240	Worth, Ih/kg of ²³⁸ U
297°K	0.0
508°K	-0.329 ± 0.007
792°K	-0.652 ± 0.008
1054°K	-0.870 ± 0.005
VH-240	
300°K	0.0
505°K	-0.182 ± 0.004
760°K	-0.360 ± 0.009
1034°K	-0.510 ± 0.010

sample containing 1.1 kg of ²³⁸U. The experimental equipment and technique are described elsewhere.* The results of the measurement are given in Table VII.3, along with the results of a similar measurement in the H-240 zone. The worth of the ²³⁸U Doppler sample is approximately 40% less in the VH-240 zone. These results indicate the importance of the study of the interaction of the ²³⁸U Doppler coefficient and the sodium-voiding effect in an LMFBF core.

*C. E. Till, R. A. Lewis, and E. F. Groh, "Doppler-Effect Measurements on a Dilute Carbide Fast Assembly--ZPR-6 Assembly No. 4Z," Reactor Physics Division Annual Report: July 1, 1965 to June 30, 1966, ANL-7210, pp. 129-137 (Dec 1966).

b. Mockup Critical Experiments. J. W. Daughtry (Last reported: ANL-7833, p. 7.3)

(1) The FTR-EMC Enrichment Experiments (R. B. Pond, A. B. Long, and C. D. Swanson). ANL-7833 covered that segment of the fuel and boron control-rod enrichment experiments from EOC-3 through SUB-7. This report will cover the remainder of the fuel enrichment experiments. The methods and techniques for making the measurements were described in detail in ANL-7833.

(a) Detailed Description of the Fuel-enrichment Experiments from SUB-8 to the Final BOL Configuration. The reactivity values

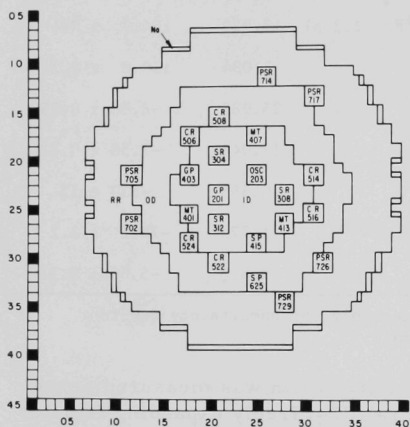


Fig. VII.4. FTR-EMC Core Map, Stationary Half.
ANL Neg. No. 116-744.

given here are those obtained by inverse kinetics corrected to 25°C and include a ± 4 lh uncertainty in reproducing the reactivity of a configuration after the halves have been separated. See Fig. VII.4 in connection with the configuration changes described in the following steps.

1. Subcritical Configuration No. 8 (SUB-8). The main purpose of this experiment was to assess the effect of the one material-test loop inserted in SUB-7 (MT 407) on the worth of three peripheral shim rods.

Starting from SUB-7, remove PSR's at locations 702, 714, and 726 and insert RR. The reactivity of SUB-8 was -1177 ± 12 lh.

2. Subcritical Configuration No. 9 (SUB-9). The main purpose of this experiment was to assess the worth of inserting two additional material-test loops.

Starting from SUB-8 insert MT's at locations 401 and 413. The reactivity of SUB-9 was -2397 ± 62 lh.

3. Beginning-of-life (BOL) Configuration. The purpose of this experiment was to establish the reactivity of the configuration of the FTR at the beginning of life. The configuration is prescribed as follows (see Fig. VII.4; also Fig. VII.3 in ANL-7825).

- (a) The six CR's at locations 506, 508, 514, 516, 522, and 524 banked at 20 in. inserted.
- (b) All fuel depletion removed.

- (c) The three MT's at locations 401, 407, and 413 inserted.
- (d) The OSC at location 203 fully withdrawn.
- (e) The three SR's at locations 304, 308, and 312 fully withdrawn.
- (f) The two GP's at locations 201 and 403 installed.
- (g) The two SP's at locations 415 and 625 installed.
- (h) With the above conditions met, a sufficient number of PSR's fully inserted to establish as near a critical state as possible. The PSR location insertion order is 702, 714, 726, 705, 717, and 729.

Condition (a) above could not be met due to the lack of suitable B₄C piece sizes necessary to mockup a control rod inserted 20 in. A compromise to the desired BOL configuration was necessary. The following steps were therefore taken based upon the assumption that the reactivity effect of six CR's inserted 20 in. is very close to the combined reactivity effect of three CR's inserted 18 in. and three CR's inserted 22 in. Additional steps were also included to verify appropriate correction factors, if needed.

4. Configuration BOL-A. The main purpose of this step was established as near to critical as possible, the reactivity of a BOL configuration having the six control rods banked at 18 in. inserted.

Starting from SUB-9, withdraw and bank at 18 in. inserted the CR's at locations 506, 508, 514, 516, 522, and 524, and insert PSR's to balance the reactivity change. BOL-A was critical with three PSR's inserted (locations 702, 714, and 726) and an excess reactivity of 212.3 ± 4.0 Ih.

5. Configuration BOL-B. The purpose of this step was to assess the worth of six control rods banked at 22 in. inserted.

Starting from BOL-A, insert from 18 to 22 in. the CR's at locations 506, 508, 514, 516, 522, and 524. The reactivity of BOL-B was -1076 ± 14 Ih.

6. Configuration BOL-C. The purpose of this step was to assess the worth of three control rods banked at 18 in. and three other control rods banked at 22 in.

Starting from BOL-B, withdraw and bank at 18 in. the CR's at locations 506, 514, and 522. The reactivity of BOL-C was -408.1 ± 4.4 Ih.

7. Configuration BOL-D. The purpose of this step was to assess the subcriticality of the BOL configuration with five PSR's inserted when three control rods are banked at 18 in. and three at 22 in.

Starting from BOL-C, insert PSR's at locations 705 and 717. The reactivity of BOL-D was -1205 ± 11 Ih.

8. Configuration BOL-E. The main purpose of this step was to establish, as near to critical as possible, the reactivity of a BOL configuration having three control rods banked at 18 in. and three other control rods banked at 22 in.

Starting from BOL-D, remove PSR's until near criticality is achieved. PSR's 705, 717, and 726 were removed. With two PSR's inserted (702 and 714), the BOL-E configuration had an excess reactivity of 13.6 ± 4.0 Ih.

(b) Data Tabulation. Table VII.4 summarizes the various core configurations assembled in the transition from SUB-7 to BOL-E.

Table VII.5 is a tabulation of all the major reactivity measurements and exchange worths obtained from EOC-3 through BOL-E. The table shows the condition of each PSR, CR, and MT in the following manner: In EOC-3 (loading 26), all are in the withdrawn condition, indicated by W. In SUB-1 (loading 28), all six PSR's have been inserted, indicated by I. Where no symbol appears for a PSR, CR, or MT in a given configuration, the state of that subassembly is unchanged from the previous configuration. In SUB-3, +25% means that the B_4C concentration was increased by 25% in the designated control rods. The superscripts on I and W indicate the number of inches that the control rod is inserted or withdrawn

TABLE VII.4. Core Configuration for Various Stages of Transition from SUB-8 to BOL-E

Configuration	Number of Material Test Regions Present	Number of Peripheral Shim Rods Present	Position of Row 5 Control Rods	Highest Remaining Depletion Number	Fissile Mass, kg	
					$^{239}\text{Pu} + ^{241}\text{Pu}$	^{235}U
SUB-8	1	0	6 fully inserted	0	542.259	3.919
SUB-9	3	0	6 fully inserted	0	530.259	3.815
BOL-A	3	3	6 banked at 18 in. inserted	0	530.259	3.815
BOL-B	3	3	6 banked at 22 in. inserted	0	530.259	3.815
BOL-C	3	3	3 banked at 18 in. inserted & 3 banked at 22 in. inserted	0	530.259	3.815
BOL-D	3	5	3 banked at 18 in. inserted & 3 banked at 22 in. inserted	0	530.259	3.815
BOL-E	3	2	3 banked at 18 in. inserted & 3 banked at 22 in. inserted	0	530.259	3.815

TABLE VII.5. Reactivity Measurements and Exchange Worths for Steps EOC-3 through BOL-E

onfiguration	Loading	PSR						CR						MT			Depletion Tubes	k excess at 25°C, Ih	Error, Ih	Exchange Worth, Ih		Error, Ih
		702	705	714	717	726	729	506	508	514	516	522	524	401	407	413				Ih	Ih	
EOC-3	26	W	W	W	W	W	W	W	W	W	W	W	W	W	W	W	63	+147.5	4.0			
SUB-1	28	I	I	I	I	I	I										63	-2058.9	37.2	-2206.4	37.4	
IC1	30																45	+13.2	4.0	+2072.1	37.4	
SUB-2	32	W	W	W	W	W	W		I		I		I				45	-1714.8	24.0	-1728.0	24.3	
IC2	39																26	+125.9	4.0	+1840.7	24.3	
SUB-3	40								+25%		+25%		+25%				26	-434.6	5.0	-560.5	6.4	
SUB-4	41							I ¹⁸	-25%	I ¹⁸	-25%	I ¹⁸	-25%				26	-1545.0	19.8	-1110.3	20.4	
IC3	43																13	+29.8	4.0	+1574.8	20.2	
SUB-5	44							I		I		I					13	-1660.3	29.6	-1690.1	29.8	
IC4-1	46																0	-272.1	4.8	+1388.2	30.0	
IC4-2	47																0	-261.7	4.2	+10.3	6.4	
SUB-6	48	I		I		I											0	-1447.8	18.7	-1186.1	19.2	
SUB-7	49														I		0	-2250.3	65.1	-802.5	67.7	
SUB-8	50	W		W		W											0	-1176.5	11.2	+1073.8	66.1	
SUB-9	52													I		I	0	-2397.1	62.1	-1220.6	63.1	
BOL-A	55	I		I		I		W ¹⁸	W ¹⁸	W ¹⁸	W ¹⁸	W ¹⁸	W ¹⁸				0	+212.3	4.0	+2609.4	62.3	
BOL-B	56							I ²²	I ²²	I ²²	I ²²	I ²²	I ²²				0	-1075.7	13.7	-1288.0	14.2	
BOL-C	57							W ¹⁸		W ¹⁸		W ¹⁸					0	-408.1	4.4	+667.6	14.3	
BOL-D	58		I		I												0	-1205.5	10.9	-797.4	11.8	
BOL-E	59		W		W	W											0	+13.6	4.0	+1219.1	11.7	
	31								I								45	-1213.0	82.7	-1226.2	82.8	
	51															I	0	-1783.1	35.4	-606.6	37.2	
	52													I			0	-2397.1	62.1	-614.1	71.5	
	53	I										W ¹⁸	W ¹⁸				0	-1542.3	17.2	+854.9	64.5	
	54			I				W ¹⁸	W ¹⁸								0	-690.3	4.7	+851.9	17.8	
	55					I				W ¹⁸	W ¹⁸						0	+212.3	4.0	+902.6	6.1	
	29																50	-513.6	9.3	+1545.3	38.4	
	35																38	-1145.0	-	+569.8	-	
	36																32	-449.1	8.3	+695.9	-	
	42																16	-312.4	4.0	+1232.6	20.2	
	45																1	-453.2	5.4	+1207.1	30.1	

in the designated configuration. For example, in BOL-B all six control rods were 22 in. inserted. W corresponds to zero insertion, I means 36-in. insertion. W^{18} is equivalent to I^{18} .

For the location of the depleted driver tubes see Fig. VII.3 in ANL-7825. The values of k -excess given in Table VII.5 are the results obtained by inverse kinetics. At the bottom of the table are two additional groups of measurements obtained as intermediate steps in the series of major configurations listed in the main part of the table. The configuration of the reactor for these measurements is defined as explained in the previous paragraph.

(c) Temperature-coefficient Data. The temperature coefficient of reactivity in the BOL-E configuration was measured on two successive days. On the first day, data were taken with the reactor cooling down from approximately 29.5 to 26.5°C. On the second day, data were initially taken with the reactor cooling between approximately 27.0 and 25.5°C, and then heating up from approximately 25.5 to 30.5°C. The results of the temperature-coefficient data, fitted to a straight line, were -3.925 ± 0.129 , -2.913 ± 0.259 , and -3.161 ± 0.087 $\text{Ih}/^\circ\text{C}$, respectively, for the two cooling and one heating cycles. The average temperature coefficient and standard deviation of these three fits is -3.333 ± 0.305 $\text{Ih}/^\circ\text{C}$. The fit of all data (cooling and heating) on the second day was -3.022 ± 0.070 $\text{Ih}/^\circ\text{C}$.

In addition to the range of results obtained for the temperature coefficient of reactivity, a shift in reactivity of 3-5 Ih was observed on two successive startups with the same loading. This difference is attributed to the nonreproducibility of (1) the gap between the halves, (2) fuel-bearing rod positions when fully inserted, and (3) ^{10}B rod positions when fully withdrawn. As in the FTR-3 experiments, an uncertainty of ± 4 Ih has been added to the standard deviations obtained for each configuration.

In previous temperature-coefficient measurements (see Progress Report ANL-7825, pp. 7.6-7.7) made in the EOC-2, EOC-3, and IC1 configurations, restrictions on the data were placed that selected only that data that indicated a nearly flat temperature profile across the reactor. The results of those measurements were that the temperature coefficient of reactivity was -4.1 ± 0.4 $\text{Ih}/^\circ\text{C}$. If only the restricted data are used from the measurements made in the BOL-E configuration, the cooling and heating data taken on the second day give a temperature coefficient -3.093 ± 0.066 $\text{Ih}/^\circ\text{C}$. Using only the heating cycle data gives a fitted coefficient of -3.141 ± 0.090 $\text{Ih}/^\circ\text{C}$. During the cooling cycles, there were insufficient data that met the "flat-profile" criterion to obtain a useful fit.

Our experience has shown that several hours of operating time are required after startup before the desired "flat" temperature

profile can be achieved. It was decided that this requirement could be relaxed when the average reactor temperature was close to the reference temperature. In this situation, the temperature correction would be small and the uncertainty in the temperature coefficient would be unimportant. Thus, from IC4 through the BOL, the average core temperature was always within about 2°C of the reference temperature, and an uncertainty in the temperature coefficient as large as 1 $\text{Ih}/^\circ\text{C}$ would result in an error no greater than 2 Ih . The best estimate of the temperature coefficient to be used in the BOL configuration is $-3.3 \pm 0.3 \text{ Ih}/^\circ\text{C}$. The value obtained for the EOC configuration was $-4.1 \pm 0.4 \text{ Ih}/^\circ\text{C}$. All the data in this report have been adjusted using the value of $-4.1 \text{ Ih}/^\circ\text{C}$.

2. Fast Critical Facilities; Experiments and Evaluation--Idaho (02-181)

a. Clean Critical Experiments. P. I. Amundson (Last reported: ANL-7833, p. 7.10)

(1) Central Zone Plate/Pin Heterogeneity Measurements in ZPPR Assembly 2 (W. K. Lehto). The central zone of the two-zone Demonstration-plant Benchmark Critical Assembly, ZPPR Assembly 2, was designed to provide a precise compositional match of the plate composition with pin-calandria matrix assemblies containing jacketed nominal 3/8-in.-dia plutonium-uranium oxide pins. The pins are positioned in an axially oriented 4 x 4 array of through tubes welded in nominal 2 x 2 x 12-in. sodium-filled calandria.

The precise relative compositions facilitate measurement of the configurational difference between the plate and pin geometries. Reactivity-difference measurements made to compare pin and plate loadings in a 69-matrix (9 x 9 with corners missing)-size zone at core center, extending 24 in. (18 in. of core plus 6 in. into blanket) into each half of the compositionally matched pin and plate geometries has shown the plate loading to be more reactive by 76.1 Ih .

Since only configuration differences were to be emphasized, considerable care was taken to eliminate or minimize the compositional differences between the two loadings. This was done by carefully selecting and weighing plate components to obtain, drawer by drawer, as close a material match as possible. The procedure followed was to select fuel plates on the basis of fissile plutonium content to match the plutonium in the preselected calandria elements. U_3O_8 plates were then selected to complete the uranium match. The oxygen match was completed by weighing and loading Fe_2O_3 . This procedure was followed in matching material compositions in each of three spatial zones for each drawer. These zones were:

- (1) The front 12 in. of the inner-core composition.
- (2) The rear 6 in. of the inner-core composition.
- (3) The first 6 in. of the axial blanket.

The remainder of the axial blanket (beyond 24 in. in each half) was used for both plates and pins so that no material balance was necessary.

A total of 42 matching calandria-plate drawers were matched in this manner, and the reactivity effect of the 69-matrix-size zone was evaluated by successive placements of these matched drawers. Reference control-rod positions were established with the plate drawers in core which were in turn replaced with matched calandria, and the reactivity changes were then measured by comparison of calibrated control-rod positions.

The above matching procedure allowed no mismatch in fissile plutonium, ^{238}U , and oxygen; however, it invariably results in certain compositional mismatches, primarily in the stainless steel constituents. The correction for these material imbalances was made zone by zone for all 414 matching zones using measured and calculated radial and axial small-sample reactivities averaged over each matching zone. The magnitude of this correction is presently being finalized.

Calculations are being performed to estimate the uncertainty in the measured value. This uncertainty is primarily due to imprecision in the knowledge of the actual mass of each material in each matching unit. The uncertainties, along with precise material densities and corrected step-by-step reactivity differences, will be reported upon completion of the data analysis.

- b. Doppler Experiments. R. E. Kaiser (Last reported: ANL-7833, p. 7.14)

Data from inverse-kinetics measurements of the PuO_2 Doppler sample in ZPPR Assembly 2 have been used to obtain an axial traverse of the reactivity effect in a 12-in. sample due to heating from 300 to 1100°K. The value at core center is negative, as reported in ANL-7825, but becomes positive at the core/axial-blanket interface. Part of this effect is due to sample expansion, since the sample is fixed at one end and expands towards the core center, that is, in the direction of increasing flux. The softer spectrum near the blanket may cause a changed Doppler effect, which could explain the remainder of the reactivity change. Further investigation is being done in obtaining traverse data from inverse-kinetics runs.

B. Support of ZPR Fast Critical Experiments

1. Fast Critical Experiments; Theoretical Support--Illinois (02-134)

- a. ZPR Heterogeneity Method Development. B. A. Zolotar (Last reported: ANL-7798, p. 103)

(1) A Comparative Study of Heterogeneity Treatments for ZPR Plate Cells (B. A. Zolotar and M. Salvatores). Heterogeneity calculations for ZPR plate lattices play an important part in the analysis of fast criticals.

Several treatments of this heterogeneity have been developed, and this work compares the calculation of resonance cross sections by three different methods.

(a) The Standard Argonne Method. The MC² code is used to obtain homogeneous broad-group cross sections for the system under study. Corrections are then made in the resonance range, using equivalence theory and the two-sided E₃ formulation to obtain in-plate capture and fission-resonance cross sections for each absorber plate. Broad-group flux shapes are determined from either S_N or integral transport methods and are used to obtain cell-averaged cross sections which preserve reaction rates. The new MC²-2 code will include the elements of this method.

(b) The RABBLE Method. This is an integral transport code with numerical integration of the slowing-down equation over the resonance range.

(c) The SMC Method.* A modified Monte Carlo treatment is used for the solution of the Boltzmann equation in the resonance region. The energy variation of a neutron history is treated exactly, and the space-angle transport is approximated by a flat-source collision-probability formulation. All SMC results presented here were supplied by B. M. Bingman and E. E. Lewis of Northwestern University.

The comparison was made for a realistic representation of the ZPR-6 Assembly 6 unit cell as given in Table VII.6. An attempt was made to ensure consistency of the cross sections used in the three calculations as far as was possible with the differing code formats. The resolved resonance cross sections were taken from ENDF/B Version I data. Other cross sections were similar, but not identical to ENDF/B. The Standard Argonne Method used integral transport rather than S_N methods. Leakage corrections were not included in any of the calculations.

Table VII.6 shows some of the results for ²³⁸U capture. The two groups shown are Group 17 (2.03-3.35 keV), which includes the sodium resonance, and Group 21 (0.275-0.454 keV), where the light-element cross sections are relatively smooth. The Monte Carlo results are for 1500 histories per group. The agreement between the methods is relatively good with the possible exception of the cell-average value in Group 17. The equivalence theory used in the Standard Argonne Method appears to give reasonable in-plate cross sections, even though the three plates containing ²³⁸U differ (as exhibited by the varying in-plate cross sections). The homogeneous and infinitely dilute values are given to provide a measure of the heterogeneity.

*B. M. Bingman and E. E. Lewis, An Approximate Monte Carlo Treatment of Resonance Absorption in Reactor Lattices, Trans. Am. Nucl. Soc. 14, 219 (1971).

TABLE VII.6. ^{238}U Capture Cross Section, b

	Standard Argonne Method	RABBLE	SMC
<u>Group 17</u>			
Infinitely Dilute	---	1.390	---
Homogeneous	1.160	1.129	---
Plate 2 ^a	1.053	1.023	0.998 ± 0.022
Plate 7 ^a	1.002	0.986	0.990 ± 0.040
Plate 10 ^a	1.050	1.024	1.100 ± 0.051
Cell Average	0.972	1.001	---
<u>Group 21</u>			
Infinitely Dilute	---	3.362	---
Homogeneous	1.197	1.109	---
Plate 2 ^a	1.126	1.077	0.97 ± 0.03
Plate 7 ^a	0.885	0.856	0.86 ± 0.03
Plate 10 ^a	1.064	1.043	0.98 ± 0.06
Cell Average	0.983	0.969	---

^aZPR-6 Assembly 6 Cell Representation

1 2 3 4 5 6 7 8 9 10
M UO Na FO SS U5 U8 FO Na UO

M = Matrix + Drawer
UO = 1/4 in. U_3O_8 Plate
Na = 1/2 in. Na Plate
FO = 1/8 in. Fe_2O_3 Plate
SS = 1/16 in. Stainless Steel Plate
U5 = 1/16 in. ^{235}U Plate
U8 = 1/8 in. ^{238}U Plate

Additional results have been obtained for ^{235}U resonance capture and fission cross sections and for flux shapes in the unit cell.

2. Fast Critical Experiments; Experimental Support--Illinois (02-013)

- a. Maintenance of Support Techniques and Facilities. E. F. Bennett
(Last reported: ANL-7765, p. 9)

(1) Reaction-rate Distributions in Fast-reactor Cells

(W. R. Robinson, M. Salvatores, G. S. Stanford, and B. A. Zolotar). Detailed intracell reaction-rate ratios in the heterogeneous plate-type loading of ZPR-6 Assembly 7* (the Single-zone Demonstration-reactor Benchmark Assembly) have been measured and calculated. The reaction-rate ratios investigated were based on fissions in ^{235}U (^{25}f), ^{238}U (^{28}f), and ^{239}Pu (^{49}f), and captures in ^{238}U (^{28}c). Figure VII.5 shows the results for the central reaction-rate ratios and also indicates the loading pattern for half of the symmetric cell. The experimental cell shown (contained in a 2-in. cube) differs from the normal cell loading in that two half-thickness fuel plates were used.

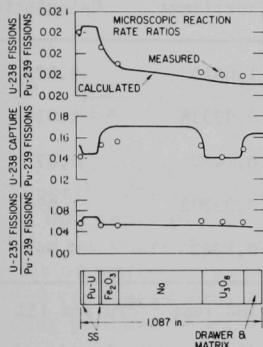


Fig. VII.5

Measured and Calculated Microscopic Reaction-rate Ratios for ZPR-6 Assembly 7. Calculated results have been normalized as indicated in Table VII.7. Absolute errors (1 σ) assigned to the experimental points are $\pm 2\%$ for $^{28}\text{f}/^{49}\text{f}$ and $^{28}\text{c}/^{49}\text{f}$, and $\pm 2.5\%$ for $^{25}\text{f}/^{49}\text{f}$. The relative precision of the points in each curve is $\pm 0.5\%$. ANL Neg. No. 116-745.

The foils were located between the cell components. Calibration of the activated foils was accomplished by three methods: fission chambers (^{25}f , ^{28}f , ^{49}f), simultaneous irradiation in a thermal flux (^{25}f , ^{49}f , ^{28}c), and radiochemistry (^{25}f , ^{28}f , ^{49}f , ^{28}c).

The calculations were based on ENDF/B Version I data, using the MC² code** to generate homogeneous 27-group cross sections. The ^{238}U and ^{239}Pu resonance cross sections were corrected for plate heterogeneity using equivalence theory to obtain self-shielding factors corresponding to the plates[†] and to foils between plates.^{††} Unit-cell fluxes were

*L. G. LeSage, E. M. Bohn, J. E. Marshall, R. A. Karam, C. E. Till, R. A. Lewis, and M. Salvatores, Initial Experimental Results from ZPR-6 Assembly 7, The Single-Zone Demonstration Reactor Benchmark Assembly, Trans. Am. Nucl. Soc. **14**, 17 (1971).

**B. J. Toppel, A. L. Rago, and D. M. O'Shea, MC², A Code to Calculate Multigroup Cross Sections, ANL-7318 (June 1967).

†K. D. Dance, "An Equivalence-Theory Capture Cross Section Code for Plate-Type Cells," Reactor Physics Division Annual Report: July 1, 1967 to June 30, 1968, ANL-7410, pp. 434-435 (Jan 1969).

††K. D. Dance, Resonance Neutron Absorption in a Foil in a Plate-Type Lattice, Nucl. Sci. Eng. **37**, 300 (1969).

calculated both with integral* and S_{16} transport methods, which gave indistinguishable results. Corrections were made for the effects of the normal core loading on the experimental cell spectrum.

The calculated reaction-rate ratios presented in Fig. VII.5 are normalized to give the experimental cell average values. Spatial distributions are closely predicted with the exception of the ^{238}U capture.

Table VII.7 compares the experimental and calculated cell averages. The calculations for the normal core are given to indicate the differences caused by the experimental loading. Auxiliary calculations with ENDF/B Version II data do not remove the discrepancies.

TABLE VII.7. Central Cell Reaction-rate Ratios

	Calculated Normal Core Loading	Calculated Experimental Loading ^a	Experiment	$\frac{\text{Experiment}}{\text{Calculation}}^b$
$^{25}\text{f}/^{49}\text{f}$	1.1588	1.1505	1.0645	0.925
$^{28}\text{f}/^{49}\text{f}$	0.02388	0.02305	0.02338	1.014
$^{28}\text{c}/^{49}\text{f}$	0.1635	0.1641	0.1430	0.871
$^{28}\text{f}/^{25}\text{f}$	0.02061	0.02004	0.02202	1.099
$^{28}\text{c}/^{25}\text{f}$	0.1411	0.1426	0.1343	0.942

^aThe 2-in. cube experimental loading had about 30% less ^{239}Pu and 15% less ^{238}U than the normal cell.

^bUsed for normalization of calculation in Fig. VII.5.

C. Fast Reactor Analysis and Computational Methods

1. Reactor Physics--Applied Computational Methods (02-081)

- a. Cross-section Data Evaluation. E. M. Pennington (Last reported: ANL-7825, p. 7.34)

ENDF/B data testing using the versions of ^{235}U , ^{238}U , and ^{239}Pu from tape 700 has been completed. Table VII.8 shows the values of k_{eff} obtained for ENDF/B benchmark assemblies using the original Version-II (V-II) data, the data modified at the broad-group level according to the suggestions of an ENDF/B task force (BGM), and the data from tape 700. It is

*F. L. Fillmore and L. D. Felten, The CALHET Heterogeneous Perturbation Theory Code and Applications to ZPR-3-48, AI-67-91 (1967); A. P. Olson and J. M. Stevenson, Calculation of Heterogeneity Effects in ZPR-Type Reactors, Trans. Am. Nucl. Soc. 12, 625 (1969).

seen that use of either BGM or tape 700 data gives better values of k_{eff} than were obtained with the original V-II data. The improved values of k_{eff} result largely from a decrease in the capture cross section of ^{238}U and increases in the fission cross sections of ^{239}Pu and ^{238}U .

TABLE VII.8. k_{eff} for Benchmark Assemblies

Assembly	V-II	BGM	700
ZPR-3-48	0.96135	0.99385	-
ZEBRA-3	0.94897	-	0.99166
JEZEBEL	0.98870	-	-
GODIVA	1.00117	-	-
ZPR-3-6F	0.99264	1.00794	1.00912
VERA-1B	0.98926	0.99999	0.99902
ZPR-3-56B	-	-	0.99886

b. Reactor Computations and Code Development. B. J. Toppel
(Last reported: ANL-7833, p. 7.22)

(1) The MC²-2 Code (H. Henryson II, C. G. Stenberg, and B. J. Toppel). The coding and preliminary testing of the resonance module (Area 1) that generates the tabulated scattering and capture cross sections to replace the unresolved and resolved resonance parameters for "light" materials as well as creating file 3 (unresolved resonance data) and file 4 (resolved resonance data) of the MC²-2 library is now complete. Part of the testing process consisted of combining the generated tabulated scattering and capture cross sections with their respective smooth tabulated values given in file 3 of ENDF/B in order to obtain the total elastic scattering and total radiative capture cross sections which appear in file 5 of the MC²-2 library. After the generated tabulated data are added to the smooth ENDF/B data, a check is made to ensure that all resulting tabulated cross sections are positive. If any cross sections are negative, they are arbitrarily reset to 10^{-5} barn. This condition has not been encountered in testing.

The computer core requirements of the resonance module consist of 13,000 words for code instructions and this leaves approximately 37,000 words for the BPOINTER container array if the module is to execute within the 50,000-word limit set forth by the Computer Code Coordination Committee. If we consider a problem execution using materials with the most extreme conditions encountered by Version II ENDF/B data that is MO with its seven isotopes, NB with its three angular momentum states, and revised ^{239}Pu with its 43 unresolved energy points, then the container array has enough remaining space to accommodate generated tabulated and capture cross sections with 3000 energy points.

The coding and preliminary testing of the module (Area 1) that generates the fission-spectra data has been started and is now completed. The generalized fission spectrum is represented by

$$\chi(E, E') = \alpha(E) \frac{E'}{T(E)^2} \exp\left[-\frac{E'}{T(E)}\right] + [1 - \alpha(E)] \sqrt{\frac{4E'}{\pi\beta(E)^3}} \exp\left[-\frac{E'}{\beta(E)}\right], \quad (1)$$

where $\alpha(E)$, $\beta(E)$, and $T(E)$ are calculated average ultrafine-group values, and E and E' are incident and final neutron energies. The first term in Eq. 1 is an evaporation spectrum and is designated by the ENDF/B law $LF = 7$. All the fissionable materials in Version II of ENDF/B neutron data are represented by $LF = 7$ or $LF = 9$ or their equivalent. With the present Version II data, linear combinations of these two laws do not exist for any materials. One of the Version II ENDF/B tapes (namely, tape 204) contains fission-spectra data with $LF = 6$ or 8 . These two distribution laws are not to be used according to the present rules set forth by the ENDF/B data formats.* $LF = 6$ or 8 corresponds to $LF = 7$ or 9 , respectively, in which α , β , and T are energy-independent quantities. The module that generates the fission-spectra data has been coded to cope with laws $LF = 6$ or 8 .

File 5 of the MC²-2 library contains the elastic scattering cross sections averaged over ultrafine groups. The elastic scattering cross section equals the smooth (tabulated ENDF/B) elastic scattering cross section, plus generated resolved resonance scattering, plus generated unresolved resonance scattering cross section. For a "heavy" mass, which is controlled by user option, the elastic scattering cross section does not include the resonance scattering cross sections. In all cases, the elastic scattering explicitly includes the potential scattering cross section. Therefore, to obtain the elastic scattering cross section for a "heavy" mass, the potential scattering cross section must be added to the smooth (tabulated ENDF/B) scattering data if and only if a "heavy" mass has ENDF/B resonance parameters. If no resonance parameters are present for a material, then the smooth (tabulated ENDF/B) scattering data are understood to already include the potential scattering. For the present, the calculation of the potential scattering cross section for "heavy" materials will be taken as constant over the energy of the resonance region; thus,

$$\sigma_p = 4\pi a^2,$$

where "a" is the effective scattering radius. This constant value of the potential scattering will be in error of 3-7% for fissile and fertile materials at the upper unresolved energy region, compared with calculating the potential scattering pointwise over the resonance region.

*M. C. Drake, Editor, Data Formats and Procedures for the Neutron Cross Section Library, BNL-50274 (T-601) (Oct 1970).

An object module library has been prepared for use in constructing load modules for Areas 5, 6, and 6.5. These areas are now being tested using a test library containing ^{239}Pu and ^{238}U . Areas 5 and 6 require about 10,000 REAL*8 locations, and Area 6.5 requires about 6500 REAL*8 locations exclusive of the POINTR container array storage requirements. These areas have now also been modified to cope with the case in which a problem mixture contains no materials having resolved or unresolved resonance parameters. In these cases, the corresponding code area (6 or 5) is not executed. In either case, the interaction Area 6.5 is then not required, and it too is bypassed after determining that certain sets have not been written.

Testing and debugging of Area 7, the module that calculates the chi fission spectrum and the macroscopic cross sections, transfer matrices, and moderating parameters, has been proceeding using ENDF/B-II data for the materials ^{241}Pu and iron. All routines in the module have been debugged to the point of executing without FORTRAN-generated error stops. The numerical results of the calculations are presently being checked. The problem options in the execution were: 2040 groups, consistent B_1 , extended transport order 9, and Improved Greuling Goertzel moderating parameters with the multigroup-CSD partition at 4.99 keV. Area 7 executed in ~1 min 10 sec, and required ~70,400 (double-precision) words of core storage. Most of the time was spent in calculating the elastic matrices (Fe-45%, Pu-23%) and the moderating parameters (24%). Although there is not an exact time comparison with the present version of MC^2 , Area 7 will take more computing time than the comparable module of MC^2 . Several reasons account for this increased running time:

- (a) The present MC^2 does not calculate moderating parameters.
- (b) All materials in MC^2 -2 will be treated by a "rigorous" Legendre algorithm.
- (c) The integration over the source group in calculating elastic matrices is improved, but also slower than MC^2 .

Although the heavy mass approximation seems to be correct, a roundoff problem has been found to exist. Plutonium-241, the heavy mass material in the present study, has three groups of downscatter. The element $\sigma_s^0(j \rightarrow j+3)$ is calculated by balance in Area 7,

$$\sigma_s^0(j \rightarrow j+3) = \sigma_s^0(j) - \sum_{j'=1}^2 \sigma_s^0(j \rightarrow j+j').$$

The element $\sigma_s^0(j \rightarrow j+3)$ is four orders of magnitude smaller than all other elements of the matrix, but has been found to be negative in some groups.

To avoid such nonphysical results, the code will set $\sigma_s^0(j \rightarrow j + 3) = 0$ if the calculation gives a negative cross section, and the other elements of the matrix will be renormalized.

To facilitate debugging of MC²-2, a modified version of BPOINTER has been prepared which provides the absolute core location of variably dimensioned arrays in the traceback prints. This new version of BPOINTER has proven to be so helpful in code debugging that it is being incorporated into all modules of the ARC System.

Testing and evaluation of the inelastic and (n,2n) scattering routine for the spectrum module, Area 8, have been completed in the sense that further testing must await the completion of the remainder of the module. The studies have shown that timing continues to be a problem in this calculation, despite the incorporation of a fast exponential routine.* The times required for the consistent-evaporation-model treatment of (n,2n) scattering, along with its susceptibility to numerical roundoff difficulties, rule this option out of consideration for production use in MC²-2. However, the option seems to be useful in evaluating the ENDF/B (n,2n) statistical data. The studies have shown that the ENDF/B data for ⁶³Cu predict a considerably harder (n,2n) source distribution than the consistent model. An FRA technical memorandum will be prepared to report the results of these studies.

Coding in Area 8 has also been proceeding. Routines are now available to calculate the multigroup and CSD asymptotic spectrum, inelastic and (n,2n) source (see above), and the new values of B² for buckling iteration calculation. The latter routine uses the same algorithms (linear or parabolic extrapolation) as those in the ARC system 1-D diffusion-theory search module.** It is hoped that the use of this more sophisticated algorithm will remove the anomalous behavior characteristic of buckling searches in subcritical systems in the present version of MC².

A preliminary version of the multigroup cross-section file, the lower interface of MC²-2, has been prepared by a subcommittee of the CCCC. The file format will probably require that records with different-length words appear. In the coding of MC²-2 to date, the I/O subroutines REED/RITE were not capable of handling such records. A new version of REED/RITE, which avoids this difficulty, has been prepared. As a consequence of the new method of implementing block-data transfer, all subprograms doing I/O have required minor modifications. Furthermore, the

*A. P. Olson, "A Fast Exponential Subroutine for Calculating Collision Probabilities on the IBM/360,"

Applied Physics Division Annual Report: July 1, 1969 to June 30, 1970, ANL-7710, pp. 446-447 (Jan 1971).

**D. E. Neal, G. K. Leaf, and A. S. Kennedy, The ARC System One-dimensional Diffusion Theory Capability, DARC1D, ANL-7715, p. 355 (May 1971).

I/O strategy is no longer transparent to users of machines with a single-length word, though the change required will amount to only one FORTRAN statement per module. The changes required in BPOINTER are considerably greater than this.

(2) An Assessment of the ENDF/B-II (n,2n) Data for ^{63}Cu Based on a Consistent Evaporation Model (H. Henryson II). In a recent report,* Segev has shown that the energy distribution of secondary neutrons from an (n,2n) reaction may be derived by a careful consideration of the energetics of the (n,n) inelastic scattering reaction. Segev derives an expression for the (n,2n) energy distribution which depends upon the inelastic scattering data and (n,2n) cross sections, but is independent of any statistical (n,2n) temperature data. All the data required for this formulation are available in files 3 and 5 of the ENDF/B tape. The ENDF/B formats, however, provide statistical data for the calculation of (n,2n) energy distributions that are independent of the inelastic scattering data. Calculations have been performed using the data for ^{63}Cu to compare the energy distributions predicted from the ENDF/B (n,2n) data and the consistent-evaporation-model treatment. In this case, the ENDF/B energy distribution is given by**

$$p(E \rightarrow E') = \frac{N}{2} \sum_{k=1}^2 E' \exp[-E'/\theta_k(E)], \quad 0 \leq E' \leq E,$$

where N is a normalization constant. The calculations were performed using subroutines of the multigroup MC²-2 code.[†] A constant lethargy group width of 0.00833 was used, and the maximum energy was taken as 15 MeV. The (n,2n) threshold for ^{63}Cu is 11 MeV (group 38 in the multigroup calculation). Figure VII.6 shows the scattering source from source group 35,

$$S(E) \equiv 2\sigma_{n,2n}(E')p(E' \rightarrow E), \quad 11.205 \text{ MeV} \leq E' \leq 11.299 \text{ MeV}.$$

These results indicate that the use of ENDF/B (n,2n) statistical data would predict too hard a spectrum in reactor calculations. Similar results apply to all the source groups in the calculation, although deviations from the consistent evaporation model become smaller as the source energy increases. The effects of these deviations on LMFBR spectra and multigroup cross sections are being investigated.

*M. Segev, "Inelastic Matrices in Multigroup Calculations," Applied Physics Division Annual Report: July 1, 1969 to June 30, 1970, ANL-7710, pp. 374-381 (Jan 1971).

**M. K. Drake, ed., "Data Formats and Procedures for the ENDF Neutron Cross Section Library," BNL-50274, p. 10.2 (Oct 1970).

[†]B. J. Toppel, "Plans for the New MC² Code, MC²-2," Applied Physics Division Annual Report: July 1, 1969 to June 30, 1970, ANL-7710, pp. 371-373 (Jan 1971).

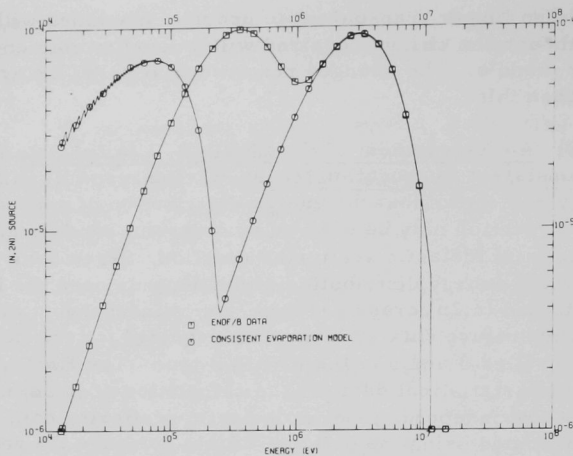


Fig. VII.6. The Scattering Source from Group 35, 11.205 to 11.299 MeV, for ^{63}Cu . ANL Neg. No. 116-777.

Since the consistent evaporation model requires a complete statistical inelastic source calculation for each sink group of the first secondary neutron, the calculation takes considerably longer than the ENDF/B formulation. Consequently, it is not feasible to use the consistent model in multigroup calculations, except as a standard against which to assess the (n,2n) statistical data provided in the ENDF/B files.

(3) Corrections Made to the Two-dimensional Neutron-inventory Module (AJC002) in the ARC System (C. G. Stenberg). The two-dimensional neutron-inventory module (AJC002),* if provided with two-dimensional fluxes, geometry specifications, and cross section data, then computes and prints the following reaction rates: (n, γ), (n, α), (n,p), fission, total, elastic removal, inelastic removal, (n,2n) removal, total removal, power, power density, and maximum-to-average power density; and the following source rates: fission, (n,2n), and scattering. These rates are computed for all isotopes and for specified materials and compositions, in all regions and in specified areas, mesh intervals, and zones. In addition, regional leakage rates, breeding ratios, and conversion ratios are available, as are fission, (n, γ), (n, α), and (n, ρ) foil at specified mesh intervals.

Even though this module has been in the ARC System for several months, user testing of this module has not been active until recently. To correctly calculate the reaction rates for each mesh interval,

*D. A. Schoengold, D. J. Bingham, G. K. Leaf, B. J. Toppel, and P. M. Walker, The ARC System Two-dimensional Adjunct Calculations, ANL-7720 (to be published), Part Two, "Two-dimensional Neutron Inventory Module, INVENT2D (AJC002)."

a few corrections had to be made in subroutines FOIL (controls the calculation of foil reaction rates), ISOFOIL (receives an isotope number, inventory type, and lists of intervals and returns a foil reaction rate at each mesh interval), and FOLCAL (calculates the foil reaction rates for each energy group and each mesh interval in a region). The corrections dealt mainly with properly dimensioning the reaction rates and fluxes as they are passed from one subroutine to another. Both the reaction rates and fluxes are represented as two-dimensional arrays. The reaction rates are represented by an array in which one dimension represents the mesh interval index which includes an entire spacial region and the other dimension represents the energy-group index. The fluxes on the other hand are represented by an array in which one dimension represents the mesh interval index which encompasses all the spacial regions and the other dimension represents the energy-group index. Also corrected in subroutine FOIL was the two-dimensional volume element. In this subroutine as well as others in this module, the two-dimensional volume elements are represented by a one-dimensional array with another auxiliary array supplying the proper indexing.

2. Reactor Code Center. M. Butler, P. Henline, and M. Legan, AMD (02-085; last reported: ANL-7833, p. 7.25)

In July three program packages were added to the Center's program library.

The first of these, HEATRAN,* a finite-element code, solves the heat-diffusion equation over a two-dimensional XY or RZ area of any shape or material distribution. Transfer by radiation across voids is allowed, and special provision is made for narrow gaps. This FORTRAN IV program is from the ENEA Computer Programme Library (E303) and was written and implemented for the ICL 4-70 by the UKAEA Reactor Group at Risley.

Los Alamos Scientific Laboratory contributed the ANCON** (ACC No. 486) program which was written in FORTRAN IV for the CDC-6600. This code solves the point-reactor kinetic equations with thermal feedback. Lump-type heat-balance equations are used to represent the thermodynamics; the heat capacity of each lump can vary with temperature. The reactivity is determined as the sum of a reactivity-feedback function, which is a function of lump temperature, and an impressed-reactivity function, which can be either a polynomial or sinusoidal function.

The third package was an IBM-360 version of the library's SAFE-3D finite element program for three-dimensional elastic analysis of heterogeneous composite structures (ACC No. 332). Oak Ridge National Laboratory prepared the IBM FORTRAN IV package, and it was checked out at the Center this month.

*W. D. Collier, HEATRAN, A Finite Element Code for Heat Transfer Problems, TRG-Report-1807(R) (1969).

**John C. Vigil, ANCON User's Manual, LA-4616 (May 1971).

During fiscal year 1971, 722 program packages were distributed by the Center to AEC contractors, universities, national laboratories, public utilities, and individuals with a professional interest in nuclear-energy computer programs.

D. Acquisition of Nuclear Data

1. Burnup Analysis and Fission Yields for Fast Reactors (02-083)

- a. Development of Analytical Procedures for Fission-product-burnup Monitors. C. E. Crouthamel and R. P. Larson
(Last reported: ANL-7655, p. 98)

An X-ray spectrometric method is being developed for the determination of the five principal rare-earth fission products: lanthanum, cerium, praseodymium, neodymium, and samarium. In the procedure, terbium (a rare earth not produced in fission) is added to the sample as an internal standard; the rare earths are then separated from interferences, electroplated on aluminum, and assayed X-ray spectrometrically. The measured line intensities are corrected for interelemental effects by means of a computer program, and the amount of each rare earth is calculated from the rare-earth-to-terbium line-intensity ratios. Work on the development of this method, which had been deferred to devote more effort to fission-yield experiments conducted in ZPR-3 (see ANL-7679, p. 112), has now been resumed.

Evaluations of the rare-earth X-ray method performed with standard rare-earth mixtures were previously reported (ANL-7618, p. 91). In those tests, when the acid solution of a rare-earth mixture was converted to a dimethylsulfoxide solution and electroplated, the recovery of the individual rare earths was quantitative, and the precision of the measurements for neodymium (the principal rare-earth fission product) was good ($\pm 1\%$). However, the precisions of the lanthanum, cerium, and praseodymium measurements were ± 4 , ± 7 , and $\pm 5\%$, respectively. When the rare earths were separated from a synthetic fuel (uranium plus inactive fission products equivalent to 1% burnup), the recovery of neodymium was again quantitative and the precision good ($\pm 1.6\%$), but the recoveries of lanthanum, cerium, and praseodymium were each $\sim 6\%$ low, and the precisions were ± 3 , ± 7 , and $\pm 3\%$, respectively.

It has now been established that the primary reason for the low recoveries and poor precision in the lanthanum, cerium, and praseodymium measurements has been a variation in background radiation. The amount of continuum radiation from the tungsten X-ray tube, which is scattered from the aluminum plate, varies from plate to plate. The cerium measurements are also affected by the scattering of characteristic radiation from the tungsten tube. (The second-order reflection of the $W\text{L}_{\beta_1}$ and the first-order reflection of the CeL_{α_1} occur at the same 2θ angle of the dispersion crystal.)

The latter problem resulted in the poorer precision for cerium than for any of the other rare earths.

An improved method has been devised for calculating the necessary corrections for background radiations and has been incorporated into the procedure. The resulting improvement in precision is demonstrated by the data given in Table VII.9.

TABLE VII.9. Evaluation of the X-ray Spectrometric Analysis for a Standard Rare-earth Mixture and a Synthetic Fuel Sample

Rare Earth	Amount, μg	% Found	
		Rare Earths Only ^a	Synthetic Sample ^b
La	13.00	98.4 \pm 1.5	97.2 \pm 0.4
Ce	28.79	98.9 \pm 1.0	98.8 \pm 1.5
Pr	11.46	99.1 \pm 2.0	93.3 \pm 0.8
Nd	39.86	100.8 \pm 1.0	100.7 \pm 1.2
Sm	7.25	100 \pm 3	98 \pm 4
Total	100.36	99.6 \pm 1.2	98.4 \pm 0.3

^a The sample containing inactive rare earths only was electroplated directly and was not carried through the separation procedure.

^b The synthetic sample was an inactive mixture of uranium and fission products equivalent to an irradiated solution having a burnup of 1%; this sample was carried through the entire procedure.

The data in Table VII.9 indicate that the praseodymium (and therefore the total rare earths) recovery is low on the synthetic irradiated sample. It is postulated that this is due to the cesium content of the sample. Cesium is not separated from the rare earths in the separation procedure and is partially electroplated. Since the energy of the characteristic emission X ray of praseodymium, L_{α} , is only 0.02 keV higher than one of the characteristic absorption edges of cesium, L_{IIIab} , the probability of absorption of the $\text{Pr}K_{\alpha}$ by $\text{Cs}L_{IIIab}$ is very high. If tests show that the presence of cesium is affecting the praseodymium measurements, the procedure can be readily modified to provide a separation of cesium from the rare earths.

PUBLICATIONS

A Comparison of Measured and Calculated ^{239}Pu , ^{235}U , and ^{238}U Integral Alpha Values in a Soft Spectrum Fast Critical Assembly

M. M. Bretscher, J. M. Gasidlo, and W. C. Redman

Nucl. Sci. Eng. 45, 87-94 (July 1971) Note

Oscilloscope Test Method for Logic Elements

C. E. Cohn

Rev. Sci. Instr. 42, 881-882 (June 1971)

The Fuel Cycle Analysis System, REBUS

L. J. Hoover, G. K. Leaf, D. A. Meneley, and P. M. Walker

Nucl. Sci. Eng. 45, 52-65 (July 1971)

An Integral Measurement of Plutonium-239 and Uranium-233 Alpha

W. Y. Kato, R. J. Armani, R. P. Larsen, P. E. Moreland,

L. A. Mountford,* J. M. Gasidlo, R. J. Popek, and C. D. Swanson

Nucl. Sci. Eng. 45, 37-46 (July 1971)

Application of the Spectral Synthesis Method to the Analysis of Spatially-Dependent Fast Reactor

W. M. Stacey

Nucl. Sci. Eng. 45, 221 (July 1971) Note

Solution of the Neutron Diffusion Equation by Space-Energy Factorization

W. M. Stacey

Nucl. Sci. Eng. 45, 189 (July 1971)

*Atomics International.

VIII. REACTOR SAFETY

A. Accident Analysis and Safety Evaluation.

G. J. Fischer (02-112)

1. Analysis of Fuel Behavior. M. G. Stevensona. Analysis of Fuel Behavior up to Gross Cladding Failure (Last reported: ANL-7765, p. 90)

The new deformation module (DEFORM-II) has been incorporated into SAS2A and is being tested extensively. A test case is reported here. The problem is the transient response of a sixth-row fuel pin in FFTF subjected to a \$30/sec ramp reactivity insertion after about 30 sec of flow coastdown. The power trace is shown in Fig. VIII.1. The initial pin power is 19.12 kW, or 7.89 kW/ft at the midplane. The flow is 30% of the nominal value. The pin is assumed to be fresh, and a radial gap of 3 mils is assumed between fuel and cladding. As shown in Fig. VIII.2, the large temperature drop across the cladding produces a considerable thermal stress up to the time $t_c \approx 55$ msec, when the gap closes at the midplane, loading the cladding through a high contact pressure (Fig. VIII.1). The cladding now yields plastically, giving a rapid increase in the equivalent strain at the outer surface (Fig. VIII.2). Thereafter, the equivalent stress at the outer surface is held to the yield strength. At $t_m \approx 60$ msec, melting

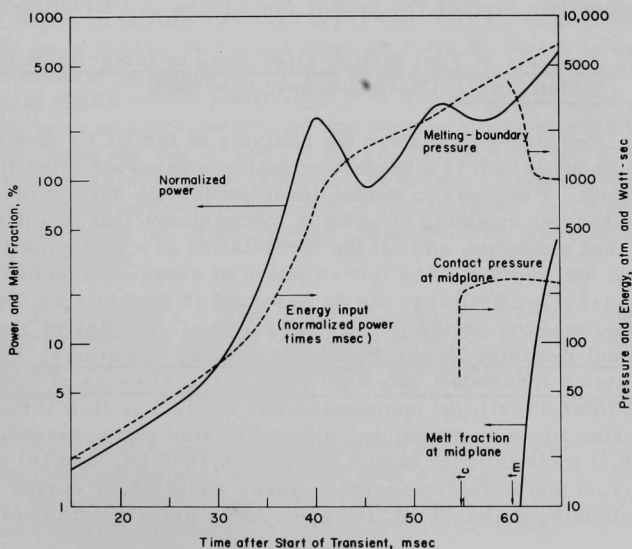


Fig. VIII.1. Power, Energy, Pressures, and Melt Fraction during Transient

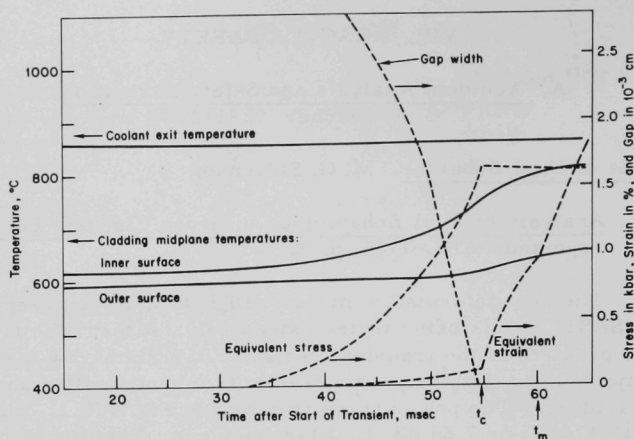


Fig. VIII.2. Temperatures, Stress, Strain, and Gap Width during Transient. Stress and strain are for cladding outer surface at the core midplane.

starts around the midplane. The high pressure of the melting boundary (Fig. VIII.1) further accelerates the increase of plastic flow, which in turn relieves somewhat the melting-boundary pressure in the fuel.

A series of tests, including analyses of TREAT shots, is being planned to confirm further the proper functioning of DEFORM-II.

b. Analysis of Fuel Motion after Loss of Integrity of Pins ("Slumping") (Not previously reported)

One prerequisite for the analysis of the FFTF flow-coastdown accident without scram is a model for fuel-pin behavior after the cladding begins to melt. Progress in model development has been made in two areas: (1) the investigation of various mechanisms that might accelerate or inhibit fuel slumping, and (2) the formulation of a mathematical representation of fuel motion. The investigation of slumping mechanisms has indicated: (a) irradiated fuel can be assumed to maintain an intact geometry until fuel melting begins [R. R. Stewart *et al.*, Studies of Fast Reactor Fuel Element Behavior Under Transient Heating to Failure: III. In-pile Experiments on Irradiated UO₂ Fuel Pins in the Absence of Coolant, ANL-7552 (Mar 1969)], (b) compaction due to viscous flow (creep) from the plenum spring force or remaining plenum fission gas apparently is small up to the fuel melting point (ANL-7825, pp. 5.16-5.18), and (c) significant fuel expansion due to fission-product gases could occur during fuel heatup after the cladding melts (R. B. Poeppel, ANL, private communication, 1971).

Mathematical modeling has been divided into two phases:

- (1) fuel behavior after loss of cladding structural support and before fuel

melting, and (2) fuel motion after melting. Phase 1 is being modeled by depicting fuel as consisting of two mechanically different regions (the columnar-grain-growth and unrestructured zones) connected by a "stick" boundary condition. This picture should be useful for representing any axial compaction from radially symmetric forces. Various ideas are being pursued for fuel motion after initiation of fuel melting. In the most promising approach, slumping is limited by the extent that molten fuel can flow down the subassembly flow channels. Here the available flow area is determined from estimates of fuel swelling. The presence of large incoherence in the voiding pattern of the FFTF equilibrium core suggests that adequate time for development of an antislumping fuel-frothing mode is possible, and the severity of the accident might be reduced.

B. Coolant Dynamics. H. K. Fauske
(02-114 and -614)

1. Liquid-Vapor Dynamics. M. A. Grolmes and H. K. Fauske (Last reported: ANL-7825, p. 8.8)

a. Liquid-film Thickness Criteria

Film-thickness or liquid-fraction data have been obtained for transient voiding in a 19-pin test section, a 7-pin section with and without wire wrap, and an annulus also with and without wire wrap. For these data, taken with air and water in transparent glass sections, the acceleration of the liquid remained constant while the velocity continuously increased for each event. For these data, the film thickness is clearly a function of both the gas velocity U and acceleration A . The data suggest a variation of liquid fraction with $(U/A)^{0.5}$. The data also illustrate the effect of the wire wrap in increasing the amount of liquid left behind in the test section. Data for the 7- and 19-pin sections appear quite similar to the data obtained in the single-pin annulus, except that the difference between wrapped and unwrapped sections is not as large. This suggests that larger bundles would not show marked differences in liquid fraction from that already obtained.

Furthermore, visual observations indicated that, for voiding in multiple-pin geometries with or without wire wrap, it is more appropriate to describe the liquid left behind in terms of a liquid fraction rather than a uniformly distributed film thickness.

For voiding under conditions for which acceleration is important, calculations might well be started with an initial liquid fraction of 0.15 to 0.2, then with it varying with $(U/A)^{0.5}$ as voiding progresses. This provides an initial film thickness or liquid fraction from which to estimate cladding-surface dryout.

2. Mathematical Models of Voiding and Reentry. H. K. Fauske (Last reported: ANL-7833, p. 8.4)

a. Models of Expulsion and Reentry

In analysis of sodium voiding resulting from a loss-of-flow accident, the behavior of the liquid film left behind on the fuel pins is of considerable importance. The dryout of this liquid film is likely to lead to immediate cladding failure. Current voiding models are generally based on the slug-flow regime (one or several large bubbles) and therefore do not consider the possibility of induced motion in the liquid film adhering to the fuel pins. Consequently, the time for dryout of this liquid film is simply based on the rate of radial liquid transport, $W_{\ell,r} = qA_H/h_{fg}$, from a stationary film as a result of evaporation, where A_H is the heated area and H_{fg} is the latent heat of vaporization. For typical LMFBR conditions and an initial liquid fraction of 0.15-0.2, this results in dryout 0.2-0.3 sec after local voiding. Therefore, a study was initiated to examine the effect of axial liquid transport as a result of induced motion in the liquid film caused by vapor drag.

The simplified physical model in Fig. VIII.3 shows the liquid-film pattern immediately following the onset of flooding, which occurs when the local vapor flux exceeds the critical velocity

$$u_g > \rho_g^{-1/2} [gD(\rho_\ell - \rho_g)]^{1/2}, \quad (1)$$

where u_g is the gas velocity, ρ_g is the gas density, D is the equivalent diameter, and ρ_ℓ is the liquid density. The flooding results from a sudden instability and formation of waves in the film several times its own thickness in amplitude. This results in a large increase in the pressure gradient and induced motion in the liquid film. For typical LMFBR conditions, the critical flooding velocity is about 30 ft/sec. A simple energy balance written for the vapor,

$$u_g \approx \frac{qA_H}{\rho_g h_{fg} A_F}, \quad (2)$$

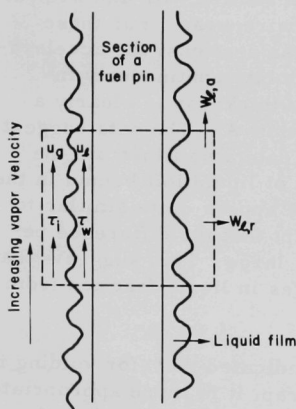


Fig. VIII.3

Simplified Dryout Model following Onset of Flooding

the axial vapor-velocity gradient existing at the time of flooding, the induced motion in the liquid film is nonuniform and therefore gives rise to a net axial transport of mass locally in the liquid film, $W_{\ell,a}$, as shown in Fig. VIII.3.

where A_F is the flow area, indicates that this velocity can be exceeded locally relatively early in the voiding process. As a result of the induced motion in the liquid film is nonuniform and therefore gives rise to a net axial transport of mass locally in the liquid film, $W_{\ell,a}$, as shown in Fig. VIII.3.

An approximate estimate of $W_{\ell,a}$ can be obtained by assuming quasi-steady incompressible flow, neglecting gravity, and specifying the constitutive equations describing the increased wall and interface shear stresses following the onset of flooding:

$$\text{Momentum of both phases: } \frac{dP}{dz} + \frac{4}{D} \tau_w = 0; \quad (3)$$

$$\text{Momentum of vapor phase: } \alpha \frac{dP}{dz} + \frac{4\sqrt{\alpha}}{D} \tau_i = 0; \quad (4)$$

$$\text{Wall shear stress: } \tau_w = \frac{1}{2} C_f \rho_\ell u_\ell^2; \quad (5)$$

$$\text{Interface shear stress: } \tau_i = \frac{1}{2} C_g [1 + 75(1 - \alpha)] \rho_g u_g^2; \quad (6)$$

where P is the pressure, u_ℓ is the liquid velocity, C_f is the liquid friction factor, and C_g is the gas friction factor. Solution of these equations, together with Eq. 3 for LMFBR conditions and an initial liquid fraction of 0.15, leads to the following conclusions: (1) The rate of axial mass transport, $W_{\ell,a}$, can be at least an order of magnitude larger than the radial mass transport, $W_{\ell,r}$; (2) local dryout spots might, therefore, occur as early as 20-30 msec after local voiding; and (3) current voiding models should be extended to include two-phase wavy annular flow between the liquid slugs.

C. Fuel Dynamics Studies in TREAT. C. E. Dickerman (02-117)

1. Transient In-pile Tests of Ceramic Fuel. C. E. Dickerman (Last reported: ANL-7783, p. 101)

a. Effects of Release of Small Amount of Molten Fuel from Seven-pin Cluster of Fresh Fuel with Local Melting (Test D1)

Test D1, performed at TREAT on June 22, used a seven-pin cluster of prototypal FFTF fuel pins with graded enrichments of UO_2 fuel. The central pin contained 1.5 in. of fully enriched pellets, yielding heat generation about 2.03 times that in the balance of the pin. The objective of the experiment was to produce local melting in the "hot" section with more-or-less normal conditions in the other parts of the cluster, so that the effects of release of a small quantity of molten fuel could be studied. Power levels for this first test of the series were specified to produce a linear power rating of 14.6 kW/ft in the "normal" part of the central pin, or about 256 W/g of fuel. The corresponding value in the "hot" section is 520 W/g. A steady reactor power was to be maintained for about 11 sec, so that conditions close to steady state would be attained in the pins.

During performance of trial transients in preparation for Test D1, evidence was obtained of an increase in the sample's power calibration factor during a transient of about 100 MW-sec. The specified powers were adjusted to reflect this apparent increase. Our preliminary estimate is that both the energy release and the average power during the 12.6-sec-long constant-power portion of the transient were within about 5% of the specified values.

Preliminary estimates based on pretest SAS1A-ASH calculations indicate that approximately 30% area melting occurred during the constant-power portion of the reactor power transient, with peak fuel temperatures sufficiently high that some fuel vaporization appears probable. Due to the apparent increase in calibration factor, the sample power would increase during the transient, leading to increasing amounts of melting as the transient progressed.

No flow or pressure anomalies were observed during the test, so pin failure apparently did not occur.

2. Experiment Support. M. B. Rodin (Last reported: ANL-7833, p. 8.22)

a. Procurement of Mark-IIA Loops for In-pile Tests

All six Mark-IIA sodium integral TREAT loops from FY 1970 stocks have been completed. The fabrication records for the last two loops (5A and 6A) are being completed. The closure flange, the main closure clamps, and the rest of the components are being fabricated. All components required to assemble the three ALIP units (for A5, A6, and prototype loops) have been manufactured, and the stator for the A6 ALIP unit has been completed. The coil weldments and magnet assemblies have been completed.

Production planning for the manufacture of additional Mark-IIA loops has been completed. Material has been received and is being examined and analyzed for compliance with the material specifications.

b. Procurement of Stretched Mark-IIC Loops for In-pile Tests

The detailed design of the Mark-IIC loop is proceeding. Stress analyses are under way. The design will comply with applicable RDT standards for a Class-A nuclear vessel.

Both Mark-II-loop TREAT-type shipping casks have been received. The fabrication records for both casks have been completed.

The Mark-II loop containing the E3 test section has been returned from Idaho to Illinois for posttest examination. The shipment was made in the Yankee Single-element Cask using an inner container specially

designed for the Mark-II loop. Due to the great weight of the Yankee cask, the loop was moved from TREAT to TAN in an intrasite shipping container, then transferred to the Yankee cask there. The test section will be removed from the loop in the CP-5 cave.

The new uranium-shielded casks for Mark-II loops are available for on-site use while final audits are under way on their construction, and the loop will be transferred to one of these casks so that the Yankee cask can be released for other use. Because the uranium casks are light enough to be moved into the CP-5 building, the possibility of moving the loop into the cave without using the transfer cask is being investigated.

3. Analytical Support. A. B. Rothman (Last reported: ANL-7783, p. 104)

Data and analyses available from fuel-dynamics Tests E1, E2, H2, E3, and E4 have been evaluated to provide preliminary modeling information on internal and external fuel motion arising from severe transient-overpower conditions. These tests together provide the first picture of LMFBR oxide-fuel behavior under transient overpower in a flow-channel environment provided by TREAT loops. One test (E3) used three irradiated oxide pins with fuel-stack lengths of about 14.5 cm. The other tests used single fresh oxide pins with fuel lengths comparable to the core length of EBR-II. The tests include the important feature that, even for FTR reactivity-input calculations exceeding \$5/sec, maximum accident cladding temperatures occur at the top of the fuel because of the axial heat transport by flowing coolant.

The results tend to support the use of SAS calculations of cladding strain up to the onset of melting. Molten fuel can reach the cladding through cracks in the solid oxide annulus inside the cladding; for sodium temperatures approaching saturation, this mobile molten oxide can melt through the cladding, presumably because the molten oxide produces local sodium vaporization that leaves the steel uncooled in the region of the molten-oxide attack. The available data support calculations predicting cladding failure at the top of the fuel, the hottest region of the cladding. Prefailure movement of molten fuel upward inside the cladding was observed, despite absence of fission-product gases; fill gas inside the fuel stack and any sorbed gas inside the oxide provide the mechanism for movement in this case.

Once failure occurs, the fuel is quite mobile. Despite relatively low conversions of thermal energy to kinetic energy, substantially all the molten fuel generated up to the time of failure was carried away from the fuel-stack region; of this, roughly one-third left the test section in E2. However, there is a tendency for the unmelted oxide to remain relatively in place: for ~30% oxide melting by volume at failure, most of the hollow stack remained; at higher melting fractions, extensive crumbling and fragmentation would be expected.

The posttest fragments of once-molten fuel are small. The distributions found from E2 are somewhat similar to those found after out-of-pile tests in which molten UO_2 was dropped into sodium. The fines of E2 are considerably smaller than those found from the TREAT-autoclave Tests S3 and S4, but are roughly comparable to those from S5 and S6 (ANL-7833, p. 8.23). From the appearance of the fines (which were not rounded "shot-like" shapes), it is apparent that the original sizes of this material were larger and that an unknown amount of fragmentation occurred before the final distributions. No evidence was found for entrapment of sodium inside hollow oxide spheres. From the extensive dispersal throughout the E2 loop, these fines can be carried out of the core. In the event of a power-excursion accident leading to general failure and release of molten fuel, the size distribution of particles involved in postaccident heat removal can be estimated roughly. Fines not resulting from solidification of molten oxide would range in size up to crumbled cylinders or annuli with outer diameters equal to the original fuel-pellet diameters (crumbled oxide fragments from structures like those of H2). Microscopic data are not yet available on fines from irradiated oxide from E3. However, the added phenomenon of fission-gas bubbles growing in the molten oxide would appear to enhance fragmentation. Whether the size distribution is significantly smaller than that of E2 depends on the scale of fission-gas bubble-nucleation sites associated with transient melting. Results of Test E3 indicate that fission-gas-driven oxide mixing with the coolant does promote a more energetic fuel-coolant interaction, but not one approaching overall thermodynamic limits. In all tests, conversion of energy to work on the coolant was low. This observation might be due partly to the effects of noncondensable gas (fill gas, fission-product gas) and transient sodium-vapor condensation. If more fuel is used per unit of surface available for condensation, as would be typical of real LMFBR subassemblies, more energy should be converted, particularly if effects of noncoherence in failure and mixing are not considered. However, there is no evidence in the tests discussed here for explosive fuel-coolant interactions approaching the thermodynamic limits of efficiency.

This picture of prefailure movements, failure mechanisms and modes, and postfailure fuel movement for oxide LMFBR fuel pins is subject to revision as more data are obtained from advanced investigations. Some of the particular points that should be noted for the tests summarized are: (1) only one test was on irradiated fuel; the test was specifically designed as an early checkpoint to guide planning and analysis of fuel-coolant interaction work, and thus did not provide data around the failure threshold in real flow-channel geometry with axial temperature gradients; (2) because of the pin length, and the relatively modest drop in sample power to the top of the fuel stack, potential inhibition of axial fuel movement in a 1-meter-long fuel stack was not simulated completely; and (3) further, because of the short fuel lengths and the fact that no true cluster tests (except for the small three-pin-cluster Test E3) had yet been performed, it is possible

that gross postfailure entrapment and mixing of fuel and coolant could be more effective in promoting energetic fuel-coolant interactions than indicated in these tests.

- a. Modeling of Multiple-pin Behavior. J. C. Carter (Last reported: ANL-7776, p. 112, under Evaluation and Development of Cluster-model Calculation Techniques)

An initial power calibration was performed for the L2 experiment. The physical arrangement of the L2 experiment is that of an assembly of seven pins, each representing the top 34.44 cm of an FTR-type pin. The seven-pin assembly is in the test section of a Mark-II loop. The loop is located in the longitudinal centerline of the TREAT core; the pressure shell of the Mark-II loop is surrounded by a B_6Si filter.

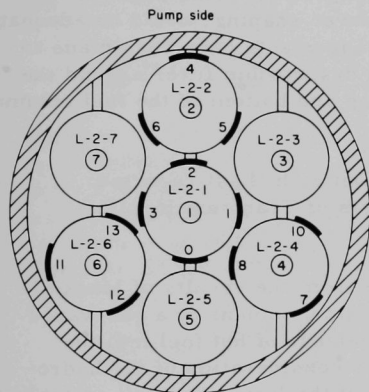


Fig. VIII.4. Location of Foils for L2 Calibration. Midplane sectional view, from top of holder looking down.

geometries. Table VIII.1 compares the estimates and measured values, averaged over the cross section of individual fuel pins, and over the assembly of seven pins.

TABLE VIII.1. L2 Power Calibration Factor

Fuel-pin Location (Fig. VIII.4)	Calibration Factor, (J/g)/MW-sec		
	R-Z	X-Y	Measured
1	1.48	1.39	1.36
2	1.89	1.69	1.48
3	1.89	1.76	1.85
4	1.89	1.64	1.96
5	1.89	1.76	1.94
6	1.89	1.69	1.86
7	1.89	1.76	1.65
Average calibration factors for the seven-pin assembly	1.83	1.68	1.72

The calibration factor was measured by means of enriched foils located on the surface of the pins and radiochemical analyses of oxide of oxide pellets from pins L-2-1 and L-2-2 (see Fig. VIII.4). Before measurements of the calibration factor, estimates were made using the SNARG code, which is based on two-dimensional transport theory and the Argonne cross-section set 201. The estimates were made in both R-Z and X-Y

In the R-Z estimate, the ring of six pins was transformed to a cylinder with approximately the same volume and surface as six fuel pins 34.44 cm long. In the X-Y estimate, the fuel pins were transformed into arrays of rectangular fuel pins. This transformation also preserved the anisotropy of material content and approximately the same surface area. The X-Y estimate was an external source-type calculation with fine mesh in the test section. In both estimates, the nonsymmetry of the Mark-II loop and its pump was not taken into account.

On the basis of this initial calibration, it was decided that the value of the power calibration using this hexaboron silicide (B_6Si) filter, with some further modifications for axial power shaping, would be adequate for the H3 experiment, but not for L2. Arrangements have been made to schedule another calibration for L2 using a dysprosium filter around the circumference of the loop, but only at the top and bottom of the fuel column, to eliminate power peaking there.

- b. TREAT Test Analyses. L. W. Deitrich (Last reported: ANL-7783, p. 105, under Analysis of Transient In-pile Experiments)

An important quantity derivable from the results of Mark-II-loop experiments is the work done on the sodium coolant by a gas-vapor bubble expanding in the test section due to release of hot fuel into the coolant. Evaluation of this quantity requires consideration of the hydrodynamics of flow in the loop and the effects of the loop geometry on coolant motion.

Because the Mark-II loop has only a small plenum above the sodium level and all parts of the loop are directly coupled to the other parts, a complete calculation of coolant motion in each part of the loop is necessary for a proper estimate of the work done on the coolant. Furthermore, the flow paths in the loop are sufficiently constricted that appreciable energy can be dissipated in fluid friction and losses due to area change during the expulsion. This energy would otherwise show up, for example, as coolant kinetic energy. Preliminary results, not including fluid-friction effects, were reported previously (ANL-7783, pp. 105-106).

Because the vapor bubble is assumed to grow in the test section, it is convenient to divide the loop into three sections or legs. The upper leg includes that portion of the flow path above the point of failure and below the junction of the upper bend and the test-section extension. The lower leg includes that portion of the flow path from the junction through the upper bend, the pump, the lower bend, and the test section below the point of failure. The third, or common, leg includes that portion of the flow path above the junction in the test-section extension. If the flow is assumed to be one-dimensional, continuous, and isothermal, the flow in

the upper leg can be determined from the upper-flowmeter readings, and that in the lower leg can be determined from the lower-flowmeter readings. The flow in the common leg is the difference of the two.

The basic equations applied to calculation of the work done in slug ejection are

$$\rho \frac{\partial v}{\partial t} = - \left(\frac{\partial p}{\partial x} + f \frac{\rho v^2}{2D_h} + \rho g + \rho v \frac{\partial v}{\partial x} \right) \quad (1)$$

and

$$\frac{\partial}{\partial x} (vA) = \frac{\partial Q}{\partial x} = 0, \quad (2)$$

where ρ is fluid density, p is pressure, v is velocity, A is flow area, D_h is hydraulic diameter, x is the space coordinate in the direction of flow, t is time, and g is the acceleration of gravity. These are the incompressible-flow momentum and continuity equations. Integration of the momentum equation with respect to x and introduction of the volume flow rate Q and a loss coefficient K lead to

$$\begin{aligned} p_r - p_f = \frac{\rho}{2} |Q|Q \left[\int_{x_r}^{x_f} \frac{f dx}{D_L A^2} + \sum \frac{K}{A^2} \right] + \frac{\rho Q^2}{2} \left[\frac{1}{A_f^2} - \frac{1}{A_r^2} \right] \\ + \rho \frac{dQ}{dt} \int_{x_r}^{x_f} \frac{dx}{A} + \rho g (x_f - x_r), \end{aligned} \quad (3)$$

which relates the pressure at the front and rear of a slug moving through the flow path to the measured coolant flow rates and geometrical parameters. Presence of the pump in the lower leg results in addition of a term $(-\Delta p_{\text{pump}})$ to Eq. 3.

Equation 3 is applied to both the upper and lower legs to find the pressure at the interface between the liquid coolant and vapor. The work done at each interface is found by multiplying the interface pressure by the flow in the leg and integrating with respect to time. The terms involving the pressure at the junction are eliminated from the resulting expressions by applying Eq. 3 to the common leg, and relating the pressures at the junction by Bernoulli's equation. Thus, energy terms related to the common leg are included. The boundary condition applied to the front of the common-leg sodium slug is that the pressure must equal the gas pressure in the plenum. The laws of adiabatic compression of a perfect gas are applied to find the work done at this interface. Finally, one sees that the total work done by the expanding gas bubble on the coolant in a time interval Δt is the

sum of (1) the increase in coolant kinetic energy during Δt , (2) the work done in compression of the loop plenum gas during Δt , (3) the net work done against the pump in moving coolant backward through it, (4) the increase in potential energy of elevation, and (5) energy dissipated in friction and area-change losses.

Because not only the coolant flow rates but also the location of liquid-vapor interfaces are changing with time, it is necessary to use a computer code to do the actual calculations. It is especially difficult to account for the frictional dissipation of energy in a hand calculation. Briefly, the code performs as follows: Each leg is subdivided into sections of constant flow area and hydraulic diameter, each having a loss coefficient due to area change applied at the inlet. Initial gas volume and pressure and sodium volumes are supplied. The flow rates measured at both flowmeters are supplied pointwise as a function of time. It is assumed that flow varies linearly with time between data points. The flow rates are integrated to determine the void volume as a function of time. Then the times at which the vapor-liquid interfaces are coincident with the boundaries of geometrical subdivisions are determined. This determination is necessary to avoid carrying out time integration over discontinuities in the values of the spatial integrals in the kinetic-energy and friction terms in Eq. 3.

Movement of the sodium slugs within the flow passages is accounted for by calculating the fraction of each section filled with sodium at each instant of time. The fill fraction for each section is applied to its length when the integrals with respect to x are calculated. Next, the rates of energy dissipation due to friction, area change, elevation change, and pump work are calculated. The coolant kinetic energy and the work done on the plenum gas are calculated. Then, the rates are integrated with respect to time, with variations of the values of spatial integrals accounted for analytically in the time-integration routines. Finally, the work done on the plenum gas, the coolant kinetic energy, and the values obtained from time integration of the rates of energy dissipation are summed to find the work done on the liquid from the beginning of voiding to the time under consideration.

The method had been applied to three Mark-II-loop power-burst experiments. These experiments (E2, E3, and H2) all resulted in some degree of slug expulsion from the test section.

Experiment E2 was a high-specific-energy-release test using one 0.290-in.-OD pin containing fresh UO_2 fuel as the central pin in a seven-pin cluster. The other six pins were gas-filled cladding tubes containing no fuel. Pin failure occurred at an energy release of about 1900 J/g of fuel. The total energy release in the transient was specified to be about 2600 J/g. At the time of failure, the beginning of rapid coolant ejection from the test section was noted, with the outlet flow (that in the upper leg)

increasing from about $1100 \text{ cm}^3/\text{sec}$ to a maximum of about $3600 \text{ cm}^3/\text{sec}$, and the inlet flow (that in the lower leg) reversing, with values as high as about $-1100 \text{ cm}^3/\text{sec}$. The work done on the coolant by the expanding bubble in the test section increased from zero at failure to approximately 100 J in about 135 msec. The most rapid rate of energy transfer occurred during the first 60 msec of the expulsion, after which a considerable reduction in the rate of energy transfer occurred. During the initial 60 msec, the rate of energy transfer from the vapor bubble to the coolant was about 1400 W.

Experiment E3 was a high-specific-energy-release transient test on three preirradiated UO_2 fuel pins of 0.174-in. OD. The pins had been irradiated to a nominal 6% burnup in a thermal-neutron flux. It was intended that the specific energy release in this experiment would be comparable to that of Test E2. Pin failure occurred at an average energy release of 710 J/g, with 810 J/g release in the hottest pin of the three. Contrary to the results of Test E2, failure occurred before the peak of the transient rather than near the end of the power burst.

Pin failure resulted in rapid expulsion of sodium out both ends of the test section with flow rates as high as 7700 and $-2050 \text{ cm}^3/\text{sec}$ recorded at the outlet and inlet flowmeters, respectively. The work done by the expanding gas bubble on the coolant rises rapidly to about 200 J at a nearly constant rate of about 6000 W. Some uncertainty exists in the results after an elapsed time of about 34 msec, since integration of the flow rate at the outlet indicates voiding of sodium past the upper flowmeter. After this time, a flow-time curve was constructed by assuming that re-entry of the slug past the upper flowmeter occurred at the time at which the initial negative flow was indicated by the flowmeter. Then a smoothed curve of integrated flow against time was used to construct an estimated flow-time curve for the period during which the upper flowmeter was voided.

Experiment H2 was a failure-threshold experiment on a single fresh mixed-oxide PNL-17 type fuel pin, of 0.230-in. OD. The transient was specified to attempt to produce pin failure at or near the end of the transient, so that large amounts of energy would not be released following failure. The energy input at pin failure was about 1220 J/g, about 84% of the total energy release during the transient. Expulsion of coolant from the test section was less vigorous in this case than in the preceding cases, and the work done on the coolant by the expanding bubble was small. A total of about 8.3 J is calculated at about 70 msec after beginning of expulsion. The maximum rate of energy transfer was about 500 W.

Selected results of the calculations are summarized in Table VIII.2, which is an update of the data in ANL-7783. Note that the energy dissipated in friction, area change, and the potential energy change due to elevation are included here and are not included in ANL-7783. Also,

some adjustments have been made in the time during the transient at which results are quoted and in treatment of the pressure-flow curve of the pump. Further, an error made in calculation of the void volume for H2 has been corrected.

TABLE VIII.2. Typical Energy Conversion in Mark-II-loop Experiments

	Experiment		
	E2	H2	E3
	1 pin plus 6 dummy pins	1 pin	3 pre- irradiated pins
Coolant kinetic-energy increase, J	Neg.	Neg.	18
Work done on plenum gas, J	94	5	106
Work done against pump, J	2.2	Neg.	2.4
Energy dissipated in friction and minor losses, J	6.3	2.8	62
Energy of elevation, J	1.2	Neg.	1.3
Work done on coolant, J	102	8.3	189
Fission-energy input to time, J	2.1×10^5	9.3×10^4	5.31×10^4
Work/fission-energy to time, %	0.050	0.009	0.355
Fission-energy input at failure, J	1.7×10^5	8.4×10^4	3.57×10^4
Work/fission-energy to failure, %	0.061	0.010	0.530

One sees that the energy dissipated in friction and minor losses is much greater in Experiment E3 than in the other cases considered, although it is proportionately as important in Experiment H2. This result is due to the high coolant velocities realized in E3, along with the flow-area changes resulting from the presence of thermocouple support structures in the outlet flow path.

Energy-conversion efficiency data for the three experiments are given in Table VIII.2. Two efficiency figures are calculated. One of these is based on the total fission-energy release in the fuel to the time at which the work done by the expanding vapor bubble on the coolant is taken. The other is based on the total fission-energy release in the fuel only to the time of failure. In both calculations, all the fuel initially present in the experiment is considered, and the sample power-reactor power calibration factor is considered constant.

Test H2 resulted in very little energy conversion, with only about 0.01% of the available fission energy at failure converted to work on

the coolant. About 0.05-0.06% conversion was realized in Test E2, which was intended to produce a more vigorous failure than that of H2. The energy conversion in Test E3 was another factor of seven to nine higher than that in Test E2, with values of about 0.5% of the fission energy at failure appearing as work on the coolant.

These results indicate that failure of preirradiated pins having high internal pressure due to fission-product gases produces an energy-conversion efficiency greater than that resulting from failure of fresh pins. Comparison of the results of Experiments E2 and E3 shows that failure of the preirradiated pins in E3 produced a much higher rate of energy transfer to the coolant than was realized in Test E2, in spite of the lower specific-energy input at failure. Although the two experiments might not be directly comparable due to different masses of fuel and geometry, the results do suggest that the presence of high-pressure fission-product gases might promote work-energy transfer from fuel to coolant. Not only do the fission-product gases do work in expanding from their initial pressure, but their presence intermixed with sodium vapor would impede condensation on cold surfaces adjacent to the fuel region.

- c. Hodoscope Development. A. DeVolpi (Last reported: ANL-7783, p. 104, under Automated Handling of Hodoscope Data)

Rather surprising but strong evidence from the hodoscope indicates early major fuel-pin distortion in the first shot (Transient 1336) of the L1 loss-of-coolant series, the distortion starting at 6.5 ± 0.5 sec with an energy input of only 20 ± 5 MW-sec. The onset of this pin movement (without rupture of cladding) confirms flowmeter indications. To expose these rather small pin distortions (with a resolution of 10 mils or less), additional extensions in hodoscope data-analysis techniques were necessary.

Thermal-neutron radiographs show that the fuel pin expanded and distorted during at least one of the three L1 transients, 1336-1338. The extent of distortion on the X-Y plane of the radiograph is about 1.5 mm (60 mils) at the top and perhaps 1 mm (40 mils) in the opposite direction at the bottom. Upward expansion at the top appears to be about 2 mm (80 mils), and about the same at the bottom.

Because the nominal vertical resolution of the hodoscope is approximately 0.875 in., an upward movement of only 10% of the vertical resolution is not likely to be detectable. The horizontal resolution in a transparent capsule is nominally 150 mils; thus the horizontal movements amount to 40% of the design basis. Although the fuel pin was enclosed in the Mark-II sodium loop, which normally degrades horizontal resolution to 250 mils, the sample was a highly enriched pin run without a thermal-neutron filter. Hence the signal-to-background ratio was about 15, far superior to the usual ratio of 2.5.

The resolution spoken of is a nominal figure, based on design and tests for the transparent capsules. The actual ability of the hodoscope to detect fuel motion depends on some factors that worsen and other factors that improve detectability. For the L1 series, it appears that lateral movements better than 10 mils are observable. This statement will be substantiated by the accompanying figures.

Initial examination of the data from L1 indicated that there was a large spread due to poor statistics for each data point. At the peak power of just 22 MW, the expected count accumulation in the nominal 11.5-msec counting interval is only 100 counts. Because the transient lasted for almost 21 sec, we recorded about 8600 frames of data to be scanned on ALICE, processed through the CDC-3600, and then ultimately rendered into graphical form. Our normal procedure is to sample the data to evaluate major trends; this early evaluation did not reveal major movements.

Figure VIII.5 is a visual presentation of the data taken well after the transient was in progress. The pin appears to be as straight as it was at the beginning of the transient.

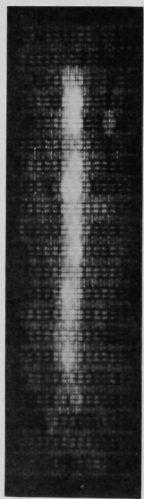


Fig. VIII.5

Fuel Pin in Transient 1336 before Distortion. Subsequent cycles do not depict fuel movement, because the effects are too small for this type of illustration.

However, further examination of the data justified additional efforts in analysis. Accordingly, two new extensions of our data analysis have been incorporated in the program TIMEPLOT, which provides a graphical rendition of the available data. First, the data were integrated from the onset of the transient to shutdown. The partial integrals, from zero to time t , were plotted as a function of t ; these plots reveal significant fuel motions. Originally, we were able to store results from only

four of the six reels of input data onto one reel of output data; thus only two-thirds of the transient could be studied at once. Based on the tentative assumption that fuel motion did not occur until past the midpoint of the transient, these early results showed marked fuel distortion. Eventually, the CDC-3600 program was changed and arrangements made to process all six reels of input tapes.

To rid the graphical output of statistical fluctuations, another feature was added to the program TIMEPLOT, so that it is possible to average the data over preset intervals and plot these averages as a function of time.

Figure VIII.6 is a plot of the power-monitor rates. This distribution closely resembles TREAT SAF-1 data, the only difference being in

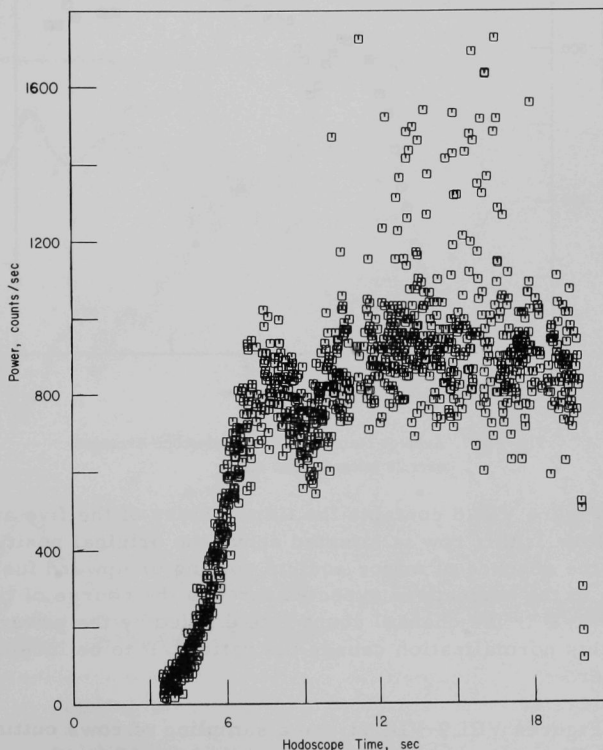


Fig. VIII.6. Average Monitor Rate from 10 Channels Insensitive to Fuel Motion in the Hodoscope Field of View. This monitor average is proportional to the TREAT power. Time resolution is 11.5 msec.

the apparent depth of the valley close to 9 sec. Figure VIII.7 is a replot of hodoscope monitors with the data averaged over 20 intervals (230 msec). All the following figures are plotted with a 230-msec averaging. "Hodoscope time" corresponds to TREAT transient-experiment time.

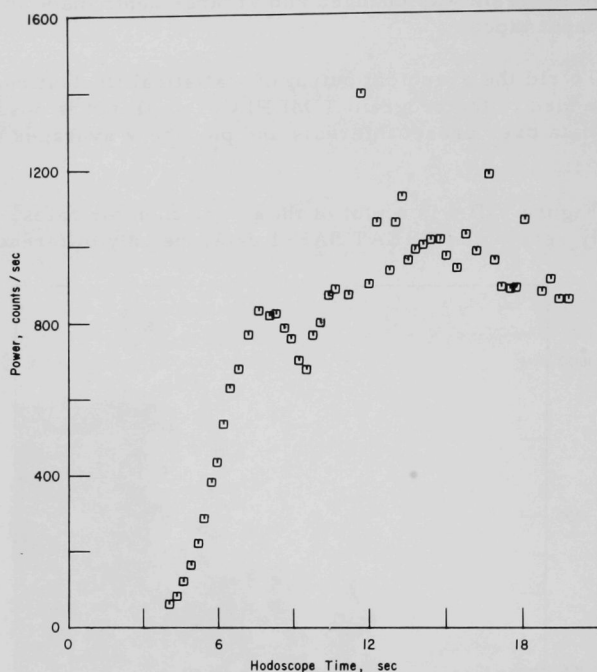


Fig. VIII.7. Average Monitor Rate for Hodoscope Averaged over 20 Intervals (230 msec)

Figure VIII.8 contains the time history of the five affected channels in Row 3; this row is situated above the original position of the fuel pin. In the absence of major sodium voiding or upward fuel movement, little change in the ordinate is expected through the course of the transient. The quantity R/P is the channel count rate divided by the power-monitor count rate; this normalization causes the ratio R/P to be independent of reactor power.

Figures VIII.9-VIII.11 are a sampling of rows cutting across the fuel pin. The pin extends from Rows 4 through 19 (each row having a vertical resolution of 0.875 in.). The fuel pin was originally situated in Columns 7-9, centered mostly between Columns 8 and 9. Horizontal definition between columns is 0.15 in.

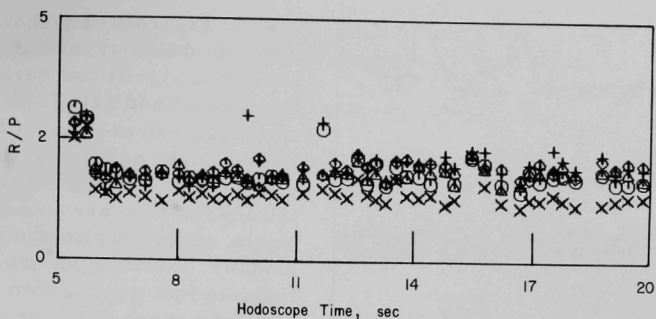


Fig. VIII.8. Power-normalized Count Rates for Five Detectors (Columns 6-10) in Row 3, about 1 in. above the Top of the Fuel Pin. This row is used for reference purposes in examining data from lower rows.

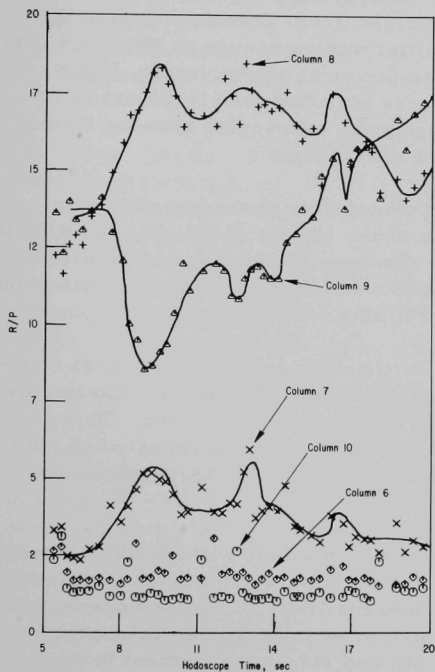


Fig. VIII.9. Fuel-pin Motion as Revealed by Variations in the Power-normalized Count Rates for the Central Columns in Row 5, Which Is about 1 in. below the Top of the Pin

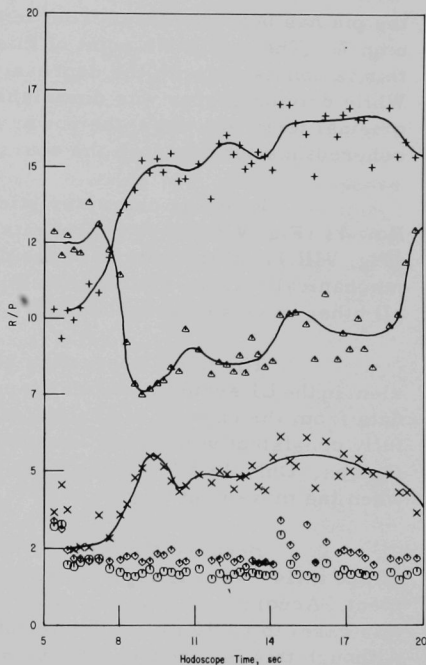


Fig. VIII.10. Fuel-pin Motion near the Middle of the Pin (Row 11)

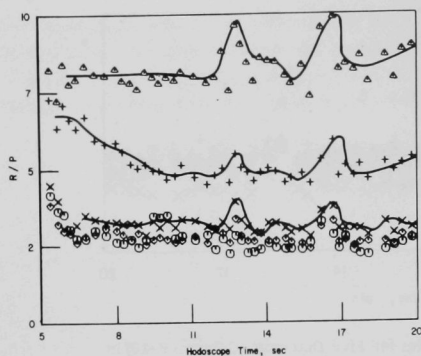


Fig. VIII.11. Fuel-pin Motion in Row 18, about 1 in. above the Bottom of the Anchored Pin

the pin has been displaced from left to right (from Column 9 toward Column 7). The maximum point of this initial motion occurs at about 9.5 sec; this is consistent with the depression in power as shown in Fig. VIII.6. While driving energy was diminishing, the pin attempted to revert to its original form; however, the power input soon recovered, causing further coherent motions through the course of the transient.

Row 5 is characteristic of movements at the top of the pin. Row 11 (Fig. VIII.10) is representative of the middle of the pin, and Row 18 (Fig. VIII.11) of the bottom of the pin. Because the pin was constrained mechanically at the bottom, much less movement was possible. Data from all other rows supports the nature and timing of these pin contortions.

The most interesting and surprising feature of this first transient in the L1 series is the early onset of fuel-pin movement. Flowmeter data from the capsule indicates loss of flow beginning at 6 sec. This is fully consistent with initial variations in pin position, as revealed in the figures. Only 20 ± 5 MW-sec was reached in TREAT integrated power when the movement began.

Because the fuel pin is enclosed in a tube with inside diameter of 320 mils, there is only 90 mils for the maximum extent of lateral movement. Accordingly, we can estimate the sensitivity of the hodoscope, in this case, to be 10 mils, or possibly just a few mils for lateral motion. Although this is a representative sodium and steel environment for the Mark-II capsule, the enrichment of the pin (93%) was large enough to provide excellent signal/background conditions (about 15/1). On the other hand, the power (maximum 22 MW) is relatively low, which leads to a loss of time resolution; for this transient, data were recorded in 12-msec increments, but the most convenient plotting resolution appears to be 230 msec. There is no evidence of any nonlinear behavior on the part of the detection system at this low power.

Figure VIII.9 shows Row-5 data. In contrast to Fig. VIII.8, observe the significant variations in the normalized rate (R/P) as a function of transient time. Channels to the far right and left of the pin (Columns 6 and 10) do not register variations, as they are focused mostly on the capsule walls and the sodium annulus. Positive values of R/P indicate fuel moving into the field of view of a given detector. Variations from the baseline value start at about 6.5 ± 0.5 sec. That Columns 7 and 8 initially reflect a rise in R/P value, and Column 9 a corresponding decrease, is interpreted to mean that

Examination of hodoscope data from the two other transients in this series (1337 and 1338) has been delayed.

D. Fuel-Coolant Interactions. R. W. Wright (02-164)

1. In-pile Simulation Tests: Expulsion and Reentry. C. E. Miller (Last reported: ANL-7776, p. 122)

- a. Detailed Design of the R-series Test Vehicle

An in-pile program is being developed to study the overall consequences of coolant expulsion and reentry following a flow transient in an LMFBR. These tests, the R-series, will simulate (with seven pins) an LMFBR single subassembly as a flow transient occurs during steady-state full-power operation. Specifically, the program has the following objectives: (a) to evaluate the consequences of various flow transients at steady power in a test vehicle that closely simulates current subassembly conditions, and (b) to verify the sequences and establish a time scale for events starting with sodium expulsion and possible reentry leading to cladding failure and fuel melting with possible molten fuel and sodium interaction.

The technical approach to meet these objectives consists of six steps: (1) Define the flow transients to be simulated and evaluate, through parametric calculations, the fuel, cladding, and coolant response to such flow transients as far as present analytical capabilities permit; the first studies are keyed to current FFTF parameters; (2) evaluate the in-pile test requirements in terms of the above studies and provide a conceptual design for a test facility that has provision for seven FFTF fuel pins and is suitable for operation in the TREAT facility; (3) evaluate the TREAT-reactor capabilities for accommodating the test facility and for providing required power to establish initial conditions in the test-facility fuel test section and sustain steady power for sufficient time to justify a meaningful experiment; (4) provide a detailed plan for facilities and operation, including final design of the test facility with instrumentation; then a hazards report and accident analysis for TREAT will be prepared, as will a schedule of experiments and a cost estimate for test-vehicle procurement; (5) formulate a pretest analysis of the anticipated performance of the TREAT reactor and test vehicle for desired flow transients; the time for initiation of coolant voiding, rates of expulsion, the time for cladding dryout and failure, and potential fuel-coolant interaction will be estimated with available models; and (6) perform a posttest analysis of the data consisting of evaluation of the key times, sequences, and importance of the activity following the flow transient; this will also provide a real test of the extent to which current analytical models can describe the consequences of such flow transients.

Progress has been made on Steps 1-3. Current efforts center on Step 4. Completion of the detailed design of the test facility and the first

test section is imminent. A preliminary safety-analysis report is nearing completion. The first experiment is scheduled for mid-FY 1973.

This test series is a joint effort of the Fuel-Coolant Interactions and Coolant Dynamics activities. Detailed discussion of the progress in preparation for the R-series tests will also be reported under the latter.

E. TREAT Operations. J. F. Boland, IF (02-122)

1. Operations. J. F. Boland (Last reported: ANL-7833, p. 8.36)

Experiment BCL-1 was subjected to three transients in which the reactor power was held constant by the computer-control system. This was the first TREAT experiment for Battelle-Columbus; the purpose was to investigate the performance of $(U_{0.8}Pu_{0.2})N$ fuel under conditions that simulated a 25% reactor-overpower condition. The experimental capsule was neutron-radiographed before and after the tests. Because the fuel is apparently undamaged, the experiment is being held in storage at TREAT pending a decision on subjecting it to another transient test.

Experiment HEDL-59-9 was received, neutron-radiographed, subjected to a calibration transient, neutron-radiographed, and placed in storage. This experiment contains a prototype FFTF fuel element that had previously been irradiated. The experiment will be subjected to a test transient after the data from the calibration transient are analyzed.

Note that the experiment number in the first sentence of the June report (ANL-7833) should have been HEDL-58-8, not HEDL-58-9.

a. Neutron Radiographs of Capsules for TREAT and EBR-II Experiments (Last reported: ANL-7833, p. 8.36, under Operations)

Neutron radiographs were made of experimental capsules from EBR-II Subassemblies XX02, X085, and X080. Posttransient neutron radiographs were also made of TREAT Experiment RAS-D1.

PUBLICATION

Inelastic Response of Primary Reactor Containment to High-energy Excursions

Joseph Gvildys and Stanley H. Fistedis
ANL-7499 Supplement (June 1971)

IX. ENVIRONMENTAL STUDIES

A. Thermal-plume Dispersion Studies.

B. Hoglund (02-166)

1. Sinking-plume Experiment. B. Hoglund and G. P. Romberg (Last reported: ANL-7825, p. 9.1)

Temperature recorders were placed on the bottom of Lake Michigan near the outfall from the Point Beach Nuclear Power Plant, Point Beach, Wisconsin, to measure water temperature on the lake bottom to determine the extent to which the bottom water might be heated as the result of a "sinking" thermal plume. Figure IX.1 shows the location of five thermographs that operated satisfactorily during the test period of March 11 to May 13, 1971.

The phenomenon of a sinking thermal plume occurs when the lake temperature is less than 4°C. The heated water discharged from the power plant entrains and mixes with the cold lake water. When the discharged and entrained water cools to 4°C, it achieves its maximum density, and gravitational forces cause it to sink through the colder, more buoyant lake water. This slightly denser mass of water should flow along the lake bottom until additional mixing further reduces the temperature.

The experiment is relevant to the behavior of waste-heat inputs during winter conditions. The Lake Michigan Enforcement Conference Technical Committee on Thermal Discharges has expressed concern* that "Bottom layering of warm water might occur over relatively large areas, having its chief effects on bottom fauna and the disruption of fish reproduction." The premature hatching of fish eggs resulting from exposure to warmer than normal ambient water is an item of particular concern.

Preliminary analysis of the data revealed that the plume did sink to the bottom as long as the lake temperature was 4°C or less. When the ambient temperature exceeded 4°C, there was no evidence of temperature perturbations on the bottom produced by the thermal discharge. Figure IX.2 shows typical data obtained from three of the thermographs. Reactor unit No. 1 (south outfall) was operating at 480 MWe. (Unit No. 2 is not operational.) A portion of the cooling water was being recirculated, and this resulted in a condenser inlet temperature of 5.6°C and a discharge temperature of 13.9°C. During the period shown, the weather changed from cloudy to fog. Winds were from the southeast and varied from 3 to 10 knots. The air temperature was relatively constant at 1-2.8°C, and the lake had 0.3- to 0.6-meter waves.

Table IX.1 summarizes the results of the experiment in terms of the percentage of time a particular sensor was influenced by the sinking

*Recommendations of the Lake Michigan Enforcement Conference Technical Committee on Thermal Discharges to Lake Michigan (Jan 1971).

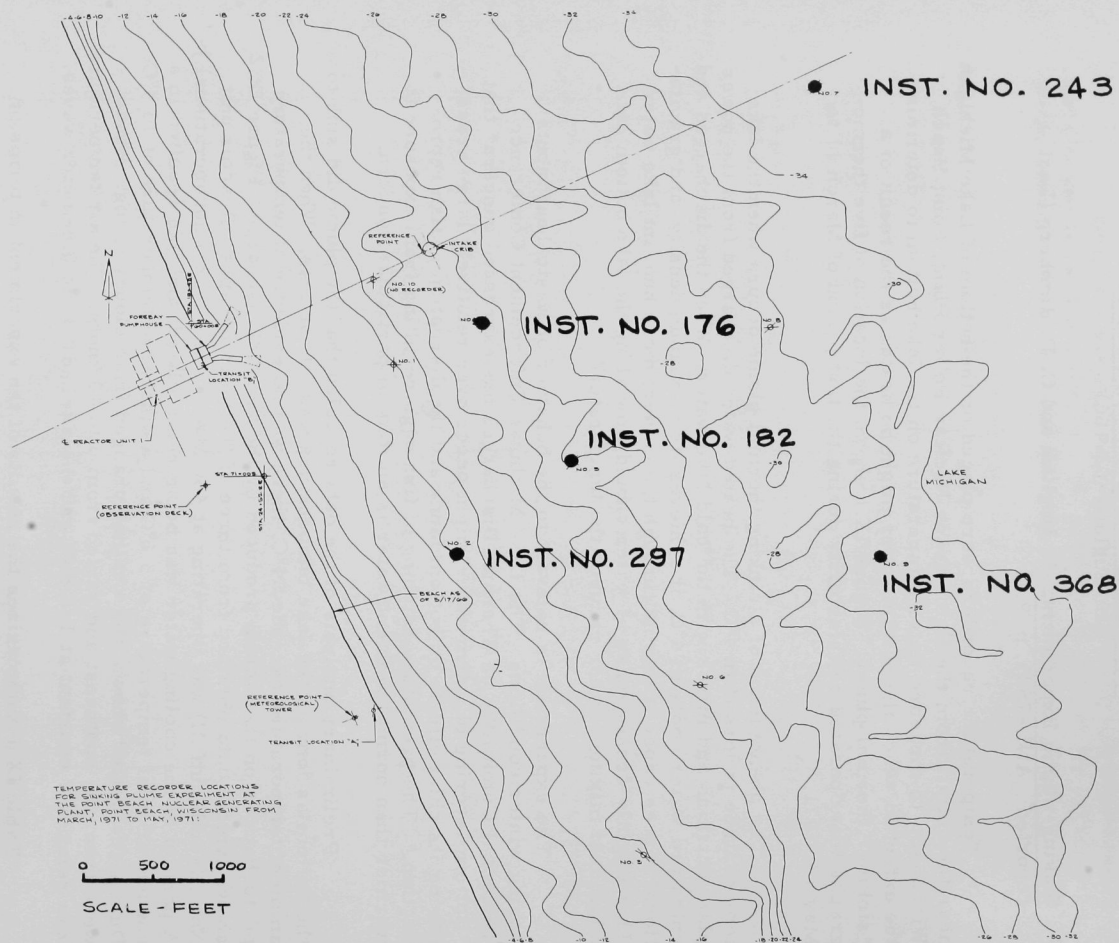


Fig. IX.1. Location of Thermographs

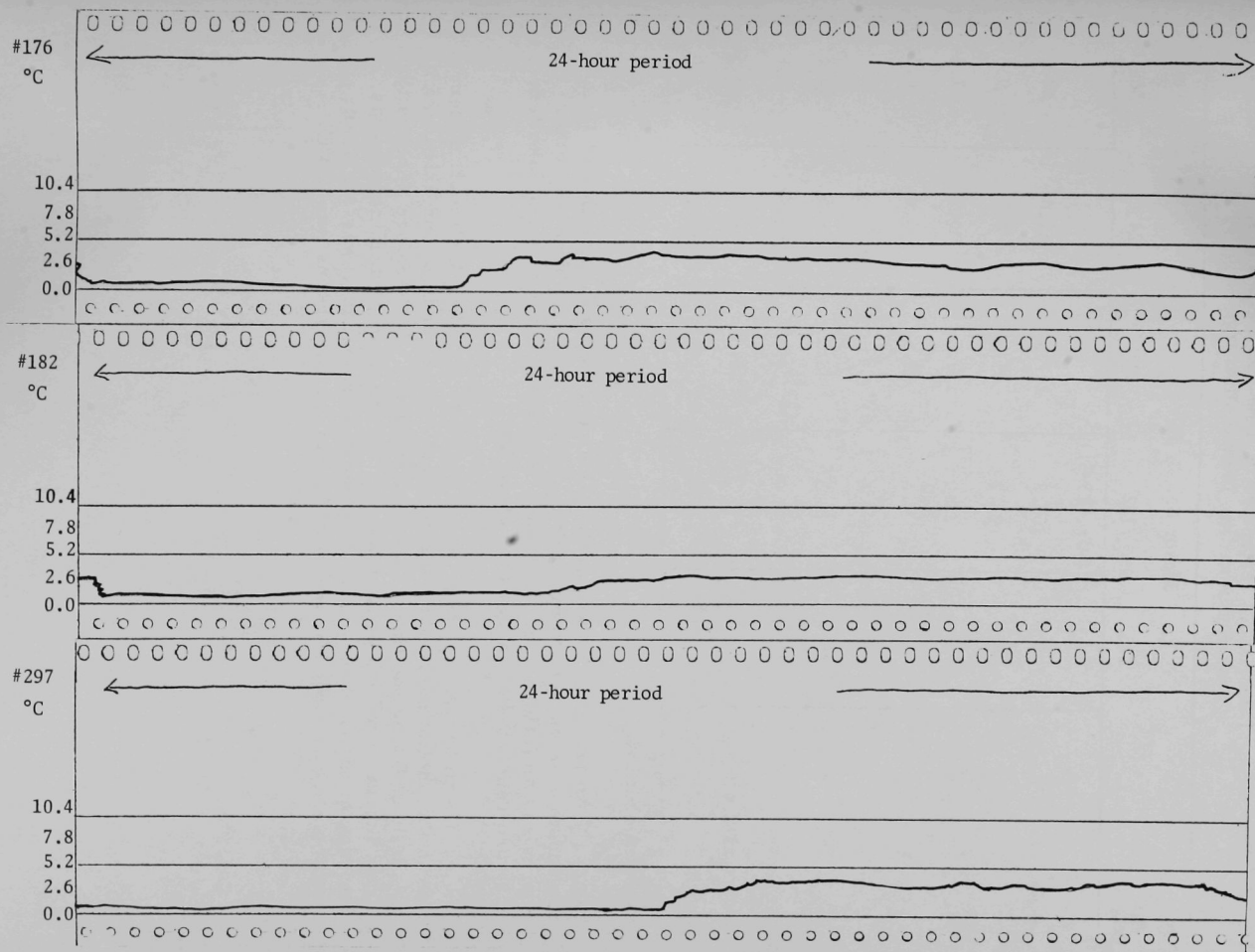


Fig. IX.2. Thermograph Data for March 12-13, 1971 (11:00 a.m.-11:00 a.m.)

TABLE IX.1. Percentage of Time Thermograph
Was Influenced by Thermal Discharge

	Sensor No.				
	176	182	297	243	368
		(Mar. 13-31)			
Hours $\Delta T > 1.5^{\circ}\text{C}$	135.8	105.8	207.5	31.0	44.0
%	29.8	23.2	45.5	6.8	9.6
Hours $\Delta T > 2.6^{\circ}\text{C}$	74.8	21.0	130.2	6.2	1.5
%	16.4	4.6	28.6	1.4	0.3
		(Apr. 1-4 & 21-30) ^a			
Hours $\Delta T > 1.5^{\circ}\text{C}$	59.8	12.5	48.5	29.5	19.5
%	17.8	3.7	14.4	8.8	5.8
Hours $\Delta T > 2.6^{\circ}\text{C}$	11.3	6.2	18.5	4.0	3.5
%	3.4	1.7	5.5	1.2	1.0

^aReactor shutdown Apr. 5-20.

plume. Two percentages are given: One represents the fraction of time the sensor was influenced by more than 1.5°C above ambient, the other represents an influence greater than 2.6°C above ambient. The lake temperature reached 4°C on approximately April 16.

Thermograph No. 297, the instrument recording the most influence, was in the shallowest water. Instruments No. 243 and 368 indicated much less influence than the three closer instruments. It therefore appears that a fair degree of mixing occurs between the inner and outer instruments. The maximum ΔT observed in the closest thermographs was 3.9°C ; the maximum ΔT recorded by the more distant thermographs was 2.3°C .

X

